BUREAU OF RECLAMATION

Mercury Loading to Streams and Reservoirs: A Process-Based Approach

U.S. Department of the Interior

September 2022

REPORT DOCUMENTATION PAGE			Form Approved OMB No. 0704-0188
The public reporting burden for this collection of information is estimated to average 1 hour per response, including the time for reviewing instructions, searching existing data sources, gathering and maintaining the data needed, and completing and reviewing the collection of information. Send comments regarding this burden estimate or any other aspect of this collection of information, including suggestions for reducing the burden, to Department of Defense, Washington Headquarters Services, Directorate for Information Operations and Reports (0704-0188), 1215 Jefferson Davis Highway, Suite 1204, Arlington, VA 22202-4302. Respondents should be aware that notwithstanding any other provision of law, no person shall be subject to any penalty for failing to comply with a collection of information if it does not display a currently valid OMB control number. PLEASE DO NOT RETURN YOUR FORM TO THE ABOVE ADDRESS.			
1. REPORT DATE *(DD-MM-YYYY)* 30-09-2022	2. REPORT TYPE Research		3. DATES COVERED *(From - To)* 10/2018-09/2022
4. TITLE AND SUBTITLE Mercury Loading to Streams and Reservoirs: A Process-Based Approach			5a. CONTRACT NUMBER XXXR4524KS-RR4888FARD1800901/FA718 5b. GRANT NUMBER 5c. PROGRAM ELEMENT NUMBER 1541 (S&T)
6. AUTHOR(S) Yong G. Lai, Ph.D., Hydraulic Engineer 303-445-2560 Ben Abban, Ph.D., Hydraulic Engineer			5d. PROJECT NUMBER Final Report ST-2022-1809-01 5e. TASK NUMBER 5f. WORK UNIT NUMBER
7. PERFORMING ORGANIZATION NAME(S) AND ADDRESS(ES) Sedimentation and River Hydraulics Group Technical Service Center, Bureau of Reclamation Denver, CO 80225			8. PERFORMING ORGANIZATION REPORT NUMBER
9. SPONSORING/MONITORING AGENCY NAME(S) AND ADDRESS(ES) Science and Technology Program Research and Development Office Bureau of Reclamation U.S. Department of the Interior Denver Federal Center PO Box 25007, Denver, CO 80225-0007			10. SPONSOR/MONITOR'S ACRONYM(S) Reclamation 11. SPONSOR/MONITOR'S REPORT NUMBER(S) Final Report ST-2022-1809-01
12. DISTRIBUTION/AVAILABILITY STATEMENT Final Report may be downloaded from https://www.usbr.gov/research/projects/index.html			
13. SUPPLEMENTARY NOTES			
14. ABSTRACT Heavy rainfall and subsequent sediment and mercury movement from watersheds have serious economic, environmental and social impacts on communities around the world. Hydrological models have become useful decision support tools for flood warning, watershed management and mercury delivery to reservoirs. The development of a process-based, mesh-distributed watershed model, however, is complex as it involves a range of disciplines and spans multiple spatial and temporal scales. In this research, a process-based and mesh-distributed model, suitable for both event-based and continuous simulations, was developed. The watershed is conceptualized in three distinct zones: a surface region and two subsurface zones representing the unsaturated soil and groundwater. Overland runoff is governed by the 2D diffusive wave equation with an optional 1D channel network solver; water in the unsaturated zone is modeled through mass conservation assuming dominant vertical processes; and the saturated groundwater flow is governed by the 2D Dupuit approximation. Soil erosion and sediment transport are governed by multi-size non-equilibrium equations incorporating the processes of soil entrainment, deposition and transport. The mercury is routed using also the mass conservation equation. The model is driven by meteorological input, taking into account vegetation characteristics to compute evaporation and plant transpiration, and land use and soil type properties. The new model represents a generalization of the existing models in an attempt to overcome some of the current model shortcomings.			
15. SUBJECT TERMS Mercury Transport; Watershed Model; Hydrological Model			
16. SECURITY CLASSIFICATION OF:		17. LIMITATION OF ABSTRACT	18. NUMBER OF PAGES 97
a. REPORT U	b. ABSTRACT U	THIS PAGE U	19a. NAME OF RESPONSIBLE PERSON Yong Lai 19b. TELEPHONE NUMBER *(Include area code)* 303-445-2560

Standard Form 298 (Rev. 8/98)
Prescribed by ANSI Std. Z39.18

Mission Statements

The U.S. Department of the Interior protects and manages the Nation's natural resources and cultural heritage; provides scientific and other information about those resources; honors its trust responsibilities or special commitments to American Indians, Alaska Natives, and affiliated Island Communities.

The mission of the Bureau of Reclamation is to manage, develop, and protect water and related resources in an environmentally and economically sound manner in the interest of the American public.

Disclaimer

Information in this report may not be used for advertising or promotional purposes. The data and findings should not be construed as an endorsement of any product or firm by the Bureau of Reclamation, Department of Interior, or Federal Government. The products evaluated in the report were evaluated for purposes specific to the Bureau of Reclamation mission. Reclamation gives no warranties or guarantees, expressed or implied, for the products evaluated in this report, including merchantability or fitness for a particular purpose.

Acknowledgements

The Science and Technology Program, Bureau of Reclamation, sponsored this research. The research is also partly funded by the Water Resources Agency, Taiwan. Technical contribution and review by Marcela Politano, University of Iowa, and Blair Greimann, Bureau of Reclamation, are acknowledged. Jun Wang, at the Division of Planning, California Great Basin Region, Bureau of Reclamation, has shared the Cache Creek watershed data used for the model validation and application.

Mercury Loading to Streams and Reservoirs: A Process-Based Approach

prepared by

Yong G. Lai, Ph.D., Hydraulic Engineer
Sedimentation and River Hydraulics Group
Technical Service Center

Final Report ST-2022-1809-01

Mercury Loading to Streams and Reservoirs: A Process-Based Approach

YONG LAI

Digitally signed by YONG LAI
Date: 2022.09.22 08:48:41 -06'00'

Prepared by: Yong G. Lai
Ph.D. and Hydraulic Engineer
Sedimentation and River Hydraulics Group, 86-68240

BENJAMIN ABBAN

Digitally signed by BENJAMIN ABBAN
Date: 2022.09.22 09:31:32 -06'00'

Prepared by: Ben Abban
Ph.D. and Hydraulic Engineer
Sedimentation and River Hydraulics Group, 86-68240

POLITANO.MARCELA.SUSANA.1511715160

Digitally signed by POLITANO.MARCELA.SUSANA.1511715160
Date: 2022.09.22 12:48:46 -04'00'

Peer Review by: Marcela Politano
Ph.D. and Hydraulic Engineer
Environmental Laboratory
US Army Engineer Research and Development Center
Vicksburg, Mississippi

Acronyms and Abbreviations

ARS	Agricultural Research Service
BARC	Burned Area Reflectance Classification
BLM	Bureau of Land Management
EPA	Environment Protection Agency
ET	evapotranspiration
GBMM	Grid-based Mercury Model
GCEW	Goodwin Creek Experimental Watershed
LAI	Leaf area index
MODIS	Moderate Resolution Imaging Spectroradiometer
NSL	National Sedimentation Laboratory
PE	potential evaporation
PET	potential evapotranspiration
SRTM	Shuttle Radar Topography Mission
TSC	Technical Service Center
USACE	U.S. Army Corps of Engineers
USGS	U.S. Geological Survey
VELMA	Visualizing Ecosystem Land Management Assessments model
WASP	Water quality Analysis Simulation Program
WY	water years

Contents

Tables

Figures

Executive Summary

Heavy rainfall and subsequent sediment and mercury movement from watersheds have serious economic, environmental, and social impacts on communities around the world. Hydrological models have become useful decision support tools for flood warning, watershed management and mercury delivery to reservoirs. The development of a process-based, mesh-distributed watershed model; however, is complex as it involves a range of disciplines and spans multiple spatial and temporal scales. In this research, a process-based and mesh-distributed model, suitable for both event-based and continuous simulations, is developed. The watershed is conceptualized in three distinct zones: a surface region and two subsurface zones representing the unsaturated soil and groundwater. Overland runoff is governed by the 2D diffusive wave equation with an optional 1D channel network solver; water in the unsaturated zone is modeled through mass conservation assuming dominant vertical processes; and the saturated groundwater flow is governed by the 2D Dupuit approximation. Soil erosion and sediment transport are governed by the multi-size non-equilibrium equations incorporating the processes of soil entrainment, deposition, and transport. The mercury is routed also using the mass conservation equation. The model is driven by meteorological input, taking into account vegetation characteristics to compute evaporation and plant transpiration, and land use and soil type properties. The new model represents a generalization of the existing models in order to overcome some of the current model shortcomings.

The new model is named SRH-W; and the runoff, soil erosion and sediment transport, and mercury transport are simulated. In this report, the mathematical equations are first presented detailing the theory of SRH-W, and the numerical methods are then summarized. The model test, verification and validation have been documented in a number of other publications and only a selected case is reported. The primary focus is on the use of SRH-W to simulate the runoff, sediment transport and mercury transport in the Cache Creek watershed, California, with special focus on the pre- and post-fire impact of the burn severity. The results demonstrate the flexibility and utility of SRH-W; it is shown that the model is capable of reproducing the field observed runoff, sediment transport and mercury movement rates within the uncertainty of the input data.

1. Introduction

Mercury (Hg) is a toxic metal that is found both naturally and as an introduced contaminant in aquatic environments. Among different forms, methylmercury (MeHg) is the most toxic to humans and aquatic organisms and tends to preferentially form in wet, anoxic environments, such as lakes and reservoirs (Kelly et al. 2006). Even very low concentrations of MeHg in water may cause high levels of mercury contamination in aquatic organisms due to bioaccumulation through the food web (Wang et al. 2004). Elevated mercury and other contaminant concentrations can severely impact drinking water quality, fish, wildlife, and ecosystem health (USEPA 1997; Carroll et al. 2000). Mercury contamination in waterbodies has become a growing concern in recent years and is the target of water quality regulations under the Clean Water Act, Section 303(d), administered by the U.S. Environmental Protection Agency. Many states have been in the process of regulating mercury in streams and reservoirs. As more attention is given to mercury contamination, Reclamation is increasingly required to comply with existing and new mercury water quality regulations. Mercury management practices need to be developed and implemented by Reclamation at the source (watershed) and reservoir scales. Numerical models of watershed-scale Hg accumulation and loading to waterbodies are being used for Hg management. However, spatially-explicit, process-based modelling tools are currently scarce.

Technical Service Center (TSC) of Bureau of Reclamation has previously developed an integrated modeling tool which was coupled to a water quality module within the two-dimensional (2D) flow model SRH-2D (Lai 2017). The integrated model, however, is limited to streams. It has since been realized that a more comprehensive Hg model is needed to take the riparian area and the watershed into account. Such a large-scale model has the following benefits: ability to (1) estimate mercury loading to streams and reservoirs which is often unknown; (2) assess wildfire impact on increased mercury loading; and (3) evaluate watershed-scale management practices for mercury controls.

This research aims to develop a suitable watershed-scale, process-based numerical model that may be used to predict and understand the mercury transport process at the watershed scale and predict mercury loading to streams and reservoirs. The proposed research builds on the knowledge of two previous Reclamation research by Lai (2017) and Wang et al. (2019). It also leverages on the partnership with Taiwan Water Resources Agency to extend SRH-2D to watershed-scale modeling. New developments include the advanced process-based modules, incorporating rainfall, vegetation, soil, surface water, ground water, and new solution schemes, allowing the use of large time step to speed up model execution. It is envisioned that the new

model will incorporate the current state-of-the-art in numerical algorithms and Hg research and may be used to model Hg loading into water bodies for practical projects. Such a model would aid river and reservoir managers in understanding where the mercury sources are and evaluating mitigation measures to reduce mercury loads.

The research aim is to develop a process-based, watershed-scale numerical model that may be used to assess and predict mercury loading to streams and reservoirs. The following research questions will be studied: (1) Can a reliable process-based, mesh-distributed, watershed-scale mercury loading model be developed that will allow Reclamation to assess the feasibility and effectiveness of mercury management measures in its facilities? (2) Can a novel numerical method be developed to simulate mercury delivery efficiently and reliably? (3) Can the mercury model be validated and demonstrated on a practical watershed?

Methylmercury in reservoirs is becoming an urgent water quality issue since many state water quality regulatory agencies have established the water quality standard for mercury (e.g. California, Oregon, Washington and Colorado). Enforcement of the mercury water quality standard requires Reclamation to comply with the new standards. For example, the State of California has performed extensive research, and the results were used to develop and encourage mercury management practices as a part of the TMDL development process. In 2016, ten Reclamation reservoirs were among those listed as “Mercury-Impaired” by the California Department of Water Quality; they were Millerton, Natoma, San Luis, Shasta, Trinity, and Whiskeytown. There are, however, no Hg loading or concentration standards established for reservoirs, as mercury loading to reservoirs has been poorly studied. Research has indicated that each aquatic environment should be evaluated individually; similar conditions in separate reservoirs have been shown to produce different rates of mercury bioaccumulation. On the one hand, current management practices can be cost prohibitive for Reclamation. On the other hand, even if they are implemented, the success of providing the appropriate level of mitigation in Reclamation facilities is uncertain since these practices have not been tested and researched.

There is an urgent need at the Reclamation-wide level to have access to a reliable mercury model that may be used to assess the feasibility of mercury management measures at each specific Reclamation reservoir. In the Mid-Pacific Region, for example, the need has been identified to develop a framework for decision making related to mercury management in reservoirs. This research represents a further step in assisting to finding cost effective solutions beyond what was developed by Wang et al. (2019). Watershed mercury models are important tools for assessing and predicting ecological/human risks of mercury. At the present, few spatially-explicit, mercury-modeling watershed models exist. Reliable numerical modeling may benefit reservoir managers and operators to answer the question of whether reservoir operational changes can be developed to reduce mercury methylation.

There are an extensive number of water quality numerical models in existence. However, only a few have the capability of simulating mercury cycling and transport in streams and reservoirs. Examples of such models include the Dynamic Mercury Cycling Model (EPRI 2009) and the Water quality Analysis Simulation Program (WASP) (Wool et al. 2006). These models simulate Hg dynamics, including methylation, within waterbodies, but require estimates or time series of Hg loads from the contributing watershed. Watershed-scale models for mercury delivery to streams and reservoirs are lacking in general.

The Watershed Analysis Risk Management Framework (Chen et al. 1998) is a watershed modeling framework used as a decision support system for watershed management for pollutant load reduction and it included an Hg loading module. The model may be classified as a lumped hydrologic model that estimates Hg loads using relatively simplistic coefficients of the land-use characteristics of a watershed; it is primarily used as a planning tool.

Two watershed-based models were developed at Environment Protection Agency (EPA) to simulate mercury loading, transport, and fate. One is the Grid-based Mercury Model (GBMM) by Dai et al. (2005) and the other is the Visualizing Ecosystem Land Management Assessments model (VELMA) by Davis et al. (2011). Both models simulate the rainfall-runoff process, though using different approaches, and mercury loading and export. These models have been applied and demonstrated at several locations such as a few small watersheds in New Hampshire and Vermont (Knightes et al. 2004), and a coastal plains watershed in South Carolina (Golden et al. 2012).

The GBMM is a spatially-explicit mercury model driven by surface runoff and sediment delivery (soil water partitioning method). It estimates Hg loads to waterbodies primarily as the particulate fraction of total Hg, with MeHg load estimated based on a simple fractions of total Hg. Empirical relations are used to estimate Hg concentrations and accumulation based on the land cover types and provide the basis for overall Hg load estimation. The model is more appropriate in watershed with large sediment yields such as those whose land use is dominated by agricultural, urbanization, or in arid environments. The model, however, lacks the in-stream processes such as sediment resuspension and bank erosion. The VELMA-Hg model is also a spatially-explicit model. Total Hg fluxes are associated with multi-soil layer hydrology and carbon, nitrogen, and Hg cycling. This model was developed for forested watersheds and focusses on the dissolved fraction of the total Hg; therefore, it is more appropriate for humid, vegetated watersheds where Hg is mostly bound to organic carbon. It is commented that both GBMM and VELMA-Hg exclude some important processes, such as methylation, sulfur dynamics, variables that increase availability of other Hg species (e.g, pH, Fe, size/quality of OM), wetland cycling, and in-stream processes. Also, the hydrological processes lack linkages with groundwater models. Both models are no longer maintained and GBMM no longer functions as it relied on obsolete versions of geospatial databases and geographic information system software.

In a recent research at Reclamation reported by Wang et al. (2019; 2020), multi-agency effort was initiated among Reclamation, the U.S. Geological Survey (USGS), the Bureau of Land Management (BLM), the U.S. Army Corps of Engineers (USACE), and Berkeley National Laboratory. The objective was to understand the mercury transport and develop an integrated modeling approach. In specific, a new model called PFHydro-WQ was developed to simulate runoff, daily sediment load, and total mercury and methylmercury loads. The model was applied to Upper Cache Creek watershed, California, with satisfactory results. The PGHydro-WQ belongs to the category of lumped model which is fast and may be used as a decision support tool.

Our research strategy is outlined as follows:

- First, develop a main watershed hydrology model to obtain reliable watershed runoff and sediment transport, using advanced numerical algorithms to improve accuracy and efficiency.

- Next, new physical processes will be developed, such as rainfall, land-over (vegetation), infiltration and ground water, through collaboration with researchers at The University of Iowa.

- Following, a mercury module will be developed based on advanced numerical algorithms.

- Finally, the model will be verified for most processes using available laboratory and field data. The completed mercury model will be applied and demonstrated to a practical watershed – the Cache Creek settling basin in California.

2. Methods

In this chapter, the theory and mathematical formulation of the mercury model SRH-W are presented, focusing on the governing equations and the numerical methods. Details of the watershed runoff and sediment modules are documented elsewhere and not repeated in this report. Readers may refer to Lai and Greimenn (2019) and Lai et al. (2020; 2022).

Watershed (or overland) runoff module is the primary engine of the model; it is discussed first. The module solves the mass and momentum conservation laws by adopting the mesh-distributed routing equations that transform rainfall excess on a watershed into runoff flow depth accurately. Various routing methods have been adopted in the past, ranging from simple to complex. As a processed-based, mesh-distributed model, SRH-W resorts to the first principle governing equations and belongs to the complex-model category.

A key assumption adopted is that the overland flow is shallow, which is true for watershed modeling. The most general shallow-water governing equations are the so-called Saint Venant equations or the dynamic-wave equations which are a mathematical expression of the mass and momentum conservation laws. The equation set is solved by SRH-2D for stream flows (Lai 2008; 2010), and it may be expressed as:

$$\frac{\partial h}{\partial t}+\frac{\partial hu}{\partial x}+\frac{\partial hv}{\partial y}=e$$
$$\frac{\partial hu}{\partial t}+\frac{\partial hu^2}{\partial x}+\frac{\partial huv}{\partial y}=gh\left(S_{ox}-S_{fx}-\frac{\partial h}{\partial x}\right)$$
$$\frac{\partial hv}{\partial t}+\frac{\partial huv}{\partial x}+\frac{\partial hv^2}{\partial y}=gh\left(S_{oy}-S_{fy}-\frac{\partial h}{\partial y}\right)$$

In the above, h is overland flow depth (m); x, y are Cartesian coordinates (m) projected onto the horizontal plane; t is time (s); u and v are depth-averaged flow velocity components (m/s) in x and y directions, respectively; e is rainfall excess rate (m/s) (rainfall minus interception, storage and infiltration); g is the gravitational acceleration (m/s^2); $S_{ox}$and S_{oy} are the land surface slopes in x and y directions, respectively; and S_{fx} and S_{fy} are the friction slopes in the x and y directions, respectively.

The dynamic-wave equations are general, but the solution of it requires sophisticated, time-consuming algorithms. Use of the dynamic-wave equations, however, may not be necessary for very shallow flows such as runoff on a watershed. Simplifications have been adopted with almost all existing watershed models. The next level of simplification is to use the so-called diffusive-wave assumption which is adopted by SRH-W. The diffusive-wave equation has the advantage of reduced computational cost but retains the ability to take into account important runoff features (e.g., backwater effect). Overland routing using the diffusive-wave equation is probably one of the most complex routing methods adopted in existing watershed models. Examples include models such as CASC2D, TREX, GSHSHA, SHETRAN, PIHM, GHOST, among others.

It is noted that a further simplification to the diffusive wave equation is the so-called kinematic wave assumption. The kinematic-wave equation has been widely used by distributed watershed models such as WEPP and EUROSEM. The additional assumption adopted by the kinematic-wave approach is that the overland flow velocity is proportional to the slope of the watershed land

surface instead of the energy slope. A principal drawback of the kinematic model is that effects such as backwater are not simulated, which may be important at locations such as the interface of overland and channel networks and relatively flat areas of a watershed.

The diffusive-wave equation may be derived from the dynamic-wave equations by neglecting the inertial term; i.e., flow acceleration/deceleration is assumed negligible and the gravity and bed frictional are in balance as:

$$S_{fx} = S_{ox} - \frac{\partial h}{\partial x} = -\frac{\partial z}{\partial x}$$
$$S_{fy} = S_{oy} - \frac{\partial h}{\partial y} = -\frac{\partial z}{\partial y}$$

where $z = z_b + h$ is the water surface elevation and z_b is the bed elevation which is computed by

$$q_i = hV_i = \alpha_i h^\beta \quad (i = x \text{ or } y;\ V_x = u, V_y = v)$$

where α_x and α_y depend on the friction slope (S_{fx}, S_{fy}), and β is a constant. If overland flow is fully turbulent – normally the case for field applications, the Manning's equation is used to relate the flow velocity to water depth as:

$$\alpha_x = \frac{S_{fx}}{n\sqrt{S}},\ \alpha_y = \frac{S_{fy}}{n\sqrt{S}},\ S = \left(S_{fx}^2 + S_{fy}^2\right)^{1/2}$$
$$\beta = \frac{5}{3}$$

where n is the Manning roughness coefficient. The above lead to the following diffusive-wave equation:

$$\frac{\partial h}{\partial t} + \frac{\partial}{\partial x}\left(\alpha_x h^\beta\right) + \frac{\partial}{\partial y}\left(\alpha_y h^\beta\right) = e$$

If the Manning's flow resistance equation is inserted, the final diffusive-wave equation may be obtained as:

$$\frac{\partial h}{\partial t} = \frac{\partial}{\partial x}\left(\frac{h^\beta}{n\sqrt{S}}\frac{\partial z}{\partial x}\right) + \frac{\partial}{\partial y}\left(\frac{h^\beta}{n\sqrt{S}}\frac{\partial z}{\partial y}\right) + e$$

If the bed slope is used in place of the friction slope, the kinematic wave equation may be obtained.

Water and sediment routing through a channel network is a very important process that should be taken into account by a watershed model; it is particularly important for large watersheds. The 1D channel network solver implemented is based on the diffusive-wave solver. In particular, the approach of Julien and Saghafian (1991) is followed. The main assumptions include:

- The channel network is dendritic with only one downstream watershed outlet;
- Channel cross-sections are rectangular or trapezoidal in shape;
- The diffusive-wave approximation is appropriate; and
- The explicit time stepping method is adopted so the time step is subject to a CFL number constraint.

For many watershed applications, the flow kinematic-wave number in the channel is usually high (e.g., > 5) or the Froude number is relatively small (e.g., < 0.5). Under such conditions, the diffusive-wave channel routing is a reasonable approach. Even for flows with high Froude number, the diffusive-wave routing is still adequate as far as the flow is relatively uniform. The diffusive-wave channel network solver provides a quick, yet reasonable, solution for many watershed applications. It is applicable to both subcritical and supercritical flows.

The derivation of the diffusive-wave equation for the 1D channel network is similar to that for the overland flow. It starts from the dynamic-wave equations. If the first two terms on the left-hand side of the above momentum equation are assumed to be in equilibrium, the momentum equation is reduced to:

$$\frac{\partial h_{ch}}{\partial x} = S_0 - S_f$$

In the above, S_0 is bed slope $[m/m]$, S_f is friction slope $[m/m]$, and h_{ch} is flow depth $[m]$. If flow is fully turbulent, the Manning's equation may be used to relate the friction slope to discharge as:

$$Q = \frac{A}{n} R^{2/3} {S_f}^{1/2}$$

where R is the hydraulic radius $[m]$ of the channel, and n is the Manning roughness coefficient. With a fixed channel cross-section shape, the above equations are combined into a single equation to solve the channel wetted cross-sectional area, *A,* the only state variable. The 1D diffusive-wave equation is written as:

$$\frac{\partial A}{\partial t} + \frac{\partial Q}{\partial x} = \frac{\partial A}{\partial t} + \frac{\partial}{\partial x}\left(\frac{AR^{2/3}}{n}\sqrt{S_0 - \frac{\partial h_{ch}}{\partial x}}\right) = q_l$$

In SRH-W, the explicit time marching scheme is used to solve the above equation which may be expressed as:

$$A^{k+1} = A^k - \frac{\delta t}{\delta x}\{Q_{up} - Q_{dn}\} \rightleftarrows + \delta t q_l$$

where δt is the time step used for the 1D channel network solver and usually different from the time step specified for the 2D overland solution, δx stands for the longitudinal distance between two cross sections of the channel, Q_{up} and $Q_{dn}$are the flow discharges at the upstream and downstream cross sections, respectively.

Once the rainfall interception is satisfied, continued rainfall is available for runoff and infiltration. Subsurface flow processes need to be simulated properly to obtain the infiltration rate on a watershed. In addition, groundwater may emerge to contribute to overland flows – it is the exfiltration process. Both infiltration and exfiltration processes are handled through the subsurface flow module.

Two options are available to compute the surface-subsurface water flux estimation:(1) a simple infiltration model that predicts infiltration rate considering only infiltration-excess runoff (exfiltration is assumed zero), and (2) a combined surface and subsurface model capable of predicting both infiltration and exfiltration.

The simple infiltration model assumes that a watershed is dominated by the Hortonian process producing an infiltration rate. Under the Hortonian process, water infiltrated is “lost” and not reflected in the watershed outflow hydrograph. This assumption is valid for watersheds in which subsurface travel time is much smaller than the overland travel time during an event. For such cases, subsurface flow responses are insignificant for the duration of the simulation, surface-subsurface interactions may be simulated assuming fluxes into the ground surface are sinks that do not affect groundwater contributions to the channel network. The coupled surface-subsurface model is computationally much more demanding, but appropriate for watersheds or storm events where subsurface processes play an important role, e.g., in watersheds where exfiltration is a prominent feature affecting surface and river hydraulics.

The Green-Ampt infiltration model assumes that the watershed is dominated by the Hortonian infiltration-excess process. The relative strength of rainfall intensity and the potential infiltration rate need to be distinguished. Whenever the rainfall rate exceeds the infiltration rate in the absence of a near-surface water table, runoff occurs due to the Hortonian mechanism (Horton, 1933). Hortonian infiltration-excess runoff is most likely to occur at a watershed where the relief is high and the water table is deep. In general, Hortonian runoff is a valid assumption in arid and semi-arid regions such as many regions of the western, mid-western and southern US when the rainfall rate exceeds 30 mm/hr (Downer et al. 2002).

The Green-Ampt model assumes that the subsurface consists of two zones: a saturated zone on the top and an initially "dry" zone at the bottom. The bottom zone has an initial water moisture content. The two zones are separated by a sharp wetting front (Bras 1990). The wet zone increases in length as infiltration progresses. The model is illustrated in Figure 1. Neglecting the level of ponding on the surface, the general equation of the Green-Ampt relationship is expressed as (Bras 1990):

$$f = K_s\left(1 + \frac{\Psi_f(\theta_s - \theta_i)}{F}\right)$$

where f is the infiltration rate (m s^{-1}) (or the infiltration capacity), K_s is saturated hydraulic conductivity (m s^{-1}), Ψ_f is capillary pressure head at the wetting front (m), θ_s is the saturated moisture content (dimensionless), θ_i is the initial moisture content (dimensionless) present in the bottom dry zone, and F is the total infiltrated depth (m).

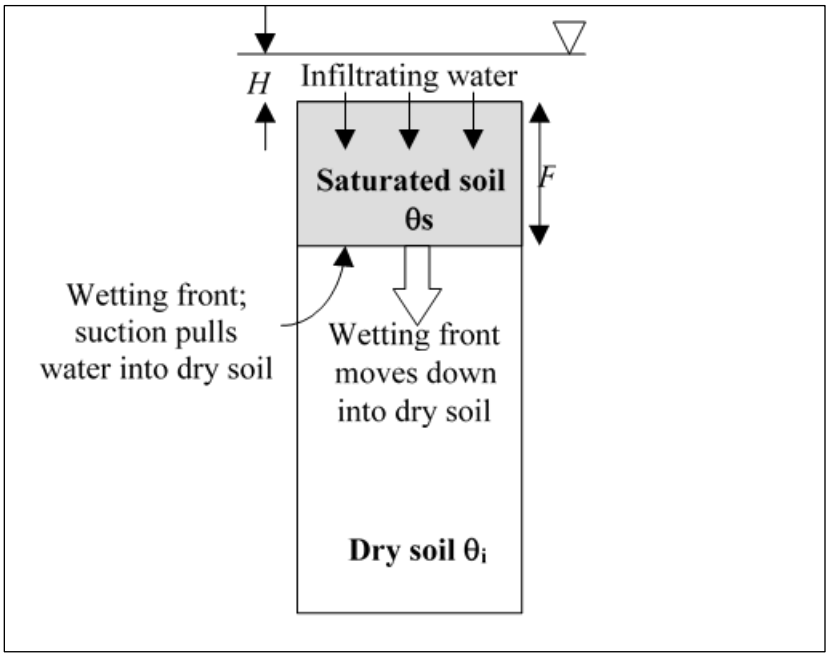

Figure 1.—Illustration of the Green-Ampt infiltration model.

SRH-W implemented the Green-Ampt model as modified by Ogden and Saghafian (1997). Three physical characteristic parameters are needed as inputs to the model: the hydraulic conductivity, the capillary pressure head, sand the moisture content deficit ($\theta_s - \theta_i$). See Rawls et al. (1983) and Chow et al. (1988) for the typical values of these parameters for different soil textures. The variance of values reported in the literature, however, is large (Maidment 1993; Downer and Odgen 2006). Therefore, these values should be used as an initial estimate and final parameters can be determined during the model calibration.

A more sophisticated surface-subsurface module is required when both infiltration and exfiltration are important, in particular for long-term, non-event based simulation. For such cases, groundwater inputs to stream flows need to be taken into account. In SRH-W, the coupled model is based on that used in PIHM watershed model (Qu and Duffy 2007) and improved in the GHOST model (Politano 2018). This coupled model can capture infiltration, exfiltration, and groundwater recharge processes simultaneously. The approach is based on the simplified Richards' equation for the subsurface flow and applicable to both small- and large-scale watersheds.

The model is conceptually illustrated in Figure *2*. The subsurface is divided into two zones: an unsaturated zone and a saturated (groundwater) zone; both zones can vary in thickness as fluxes enter or leave the zones. There is a vertical flux exchange between the ground surface and the unsaturated zone, and also between the unsaturated and saturated zones. When the unsaturated zone is completely depleted, vertical flux is exchanged directly between the saturated zone and the ground surface.

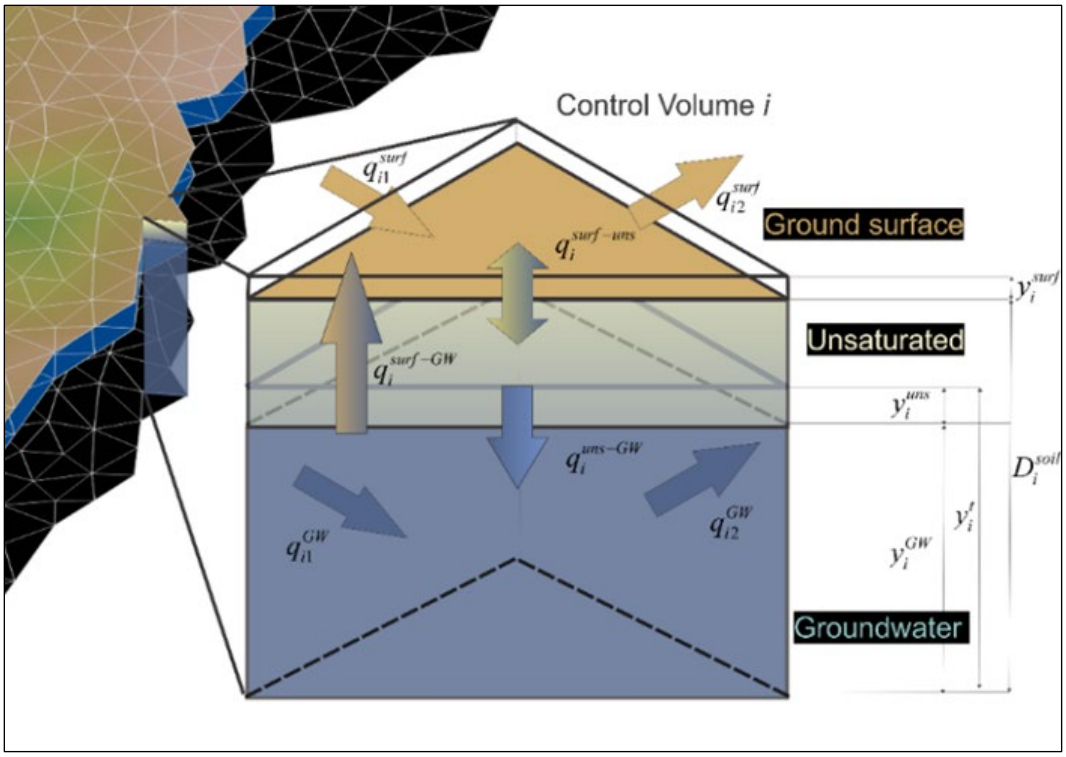

Figure 2.—Illustration of surface-subsurface interaction and subsurface flow representation (figure source: Politano 2018).

In the unsaturated zone, the approach is subject to the following limitations:

- Lack of resolution of the vertical water content profile in the unsaturated zone; and
- Not able to predict the wetting-front displacement in the unsaturated zone.

The force driving mass flux between the surface and subsurface is the total head difference, which is computed as:

$$\Delta h_i = \left[y_i^{surf} - max\left(y_i^{soil} - D_i^{soil}, 0\right)\right] - \psi_i$$

where y_i^{surf} and y_i^{soil} are the water heads on the ground surface and in the subsurface zones, respectively, D_i^{soil} is the thickness of the soil layer from ground surface to bedrock, and ψ_i represents the capillary head. y_i^{soil} is the sum of the heads of water in the groundwater and unsaturated zones, y^{GW} and y^{uns}, respectively. A positive value of Δh_i denotes infiltration while a negative value denotes exfiltration. When heads in the surface and subsurface are the same, the driving force is zero and equilibrium between the regions is reached. Groundwater can only contribute to overland flow when the water table reaches the ground. Exfiltration occurs when the soil is fully saturated and is modeled considering the contributions of both the initially unsaturated zone and groundwater region.

Using the total head difference, the mass flux between the surface and unsaturated region, $q^{surf\text{-}uns}$, is computed as:

$$q_i^{surf-uns} = \begin{cases} Z_i^{surf}\Gamma_i & \text{if } \Delta h_i > 0 \text{ (infiltration)} \\ \begin{cases} \dfrac{y_i^{uns}}{y_i^{soil}}\Gamma_i & \text{if } |\Gamma_i^{uns}| < |\Gamma_i| \\ \Gamma_i & \text{if } |\Gamma_i^{uns}| > |\Gamma_i| \end{cases} & \text{if } \Delta h_i < 0 \text{ (exfiltration)} \end{cases}$$

where $\Gamma_i = \frac{k_i^v}{l_i^{exc}}\Delta h_i$ is the maximum mass flux, with k_i^v the vertical hydraulic conductivity and l_i^{exc} the coupling length, y^{uns} is the head of water in the unsaturated zone, and Z_i^{surf} is a sigmoid function to adjust infiltration for water stored in depression storage D_i^{strg}:

$$Z_i^{surf} = \left(\frac{\left(y_i^{surf}\right)^3}{\left(y_i^{surf}\right)^3 + \left(D_i^{strg}\right)^3}\right)$$

Gravity-dominated, vertical flow is assumed in the unsaturated zone, giving in the following equation, which is solved for y^{uns}:

$$\phi\frac{dy^{uns}}{dt} = q^{surf-uns} - q^{uns-GW} - T^{uns} - E^{uns}$$

where ϕ is the porosity, q^{uns-GW} is the mass flux from the unsaturated region to groundwater (recharge), and T^{uns} and E^{uns} are water losses by plant transpiration and evaporation in the unsaturated region.

Similarly, the groundwater head, y^{GW}, in the saturated zone is calculated from Darcy's law and mass balance as:

$$\phi_i \frac{dy^{GW}}{dt} + \nabla.\left(\boldsymbol{K}\,\nabla y^{GW}\right) = q^{uns-GW} - q^{GW-surf} - E^{GW} - T^{GW}$$

where $\mathbf{K}$ is the hydraulic conductivity tensor, $q^{GW-surf}$ represents direct mass flux exchange between groundwater and the surface, and E^{GW} and T^{GW} are water losses by evaporation and transpiration in the groundwater, respectively. The term $\nabla.(\mathrm{K}\nabla y^{GW})$ represents lateral subsurface fluxes in the groundwater zone.

An overview on estimation of the plant transpiration and evaporation terms are described in the section below. Further details are also provided in Lai et al. (2020).

The type of land cover present on a landscape dictates its response to atmospheric and hydrologic forcing. Important land cover properties affecting the hydrologic cycle and flow response include the canopy cover, vegetation height, albedo, leaf area index, shade factor, surface roughness, and depression storage volume. The type of vegetation present also determines root depths, which in turn control the extent of abstraction of water from the subsurface by the vegetation. Collectively, the land cover properties directly affect the interception of precipitation, above-ground water storage, evapotranspiration rates and below-ground water storage, and overland flow rates. The land cover properties are thus key inputs to SRH-W. More information on the land cover properties and their individual effects and roles is provided in Lai et al. (2020).

For long-term simulation, a major source of water loss is the evapotranspiration (ET) process and should be included in a watershed model. The ET module in SRH-W is developed based on the GHOST watershed model of Politano (2018). It estimates the water loss from a watershed due to several mechanisms such as evaporation from canopy-intercepted rainfall, surface water and land soil, and crop transpiration. These processes are illustrated in Figure *3* below.

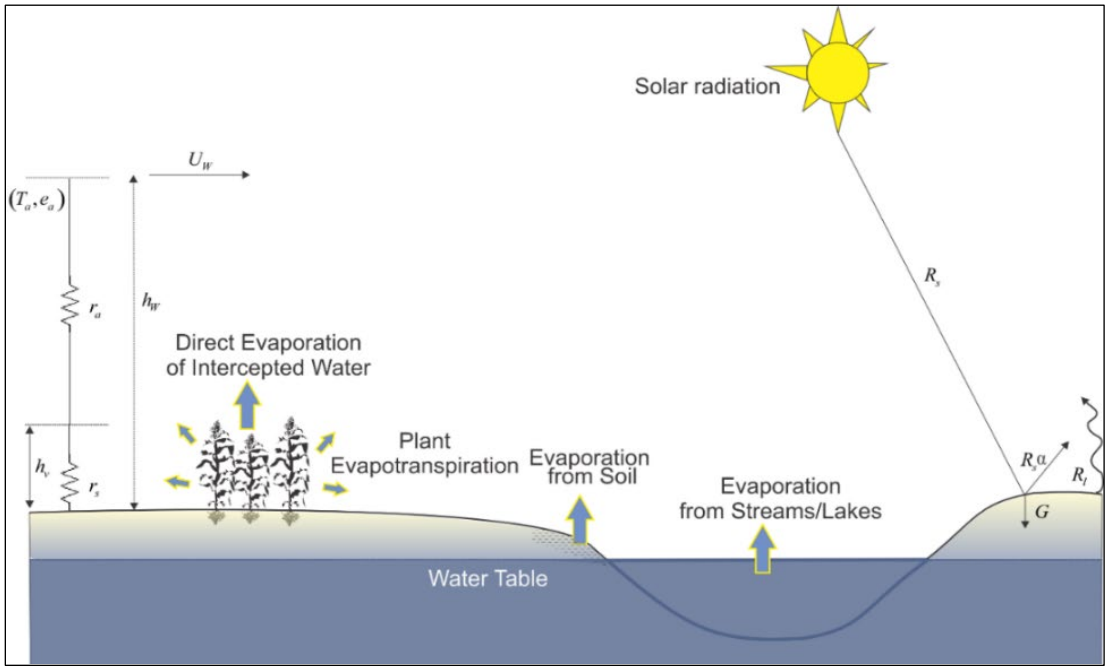

Figure 3.—Schematic representation of the evapotranspiration module (figure source: Politano 2018).

An overview of the ET module procedure is shown in Figure *4*. The different ET components are determined sequentially, starting with evaporation of intercepted water on plant/tree canopy, followed by evaporation of water stored on the surface, and then finally evapotranspiration of water from the soil subsurface.

A summary of the steps is as follows:

- At the start of the computation, the available energy in the atmosphere to drive ET under prevalent weather conditions is estimated in the form of the Potential Evapotranspiration (PET). PET represents the rate (energy) at which evaporation would occur under the condition of an infinite water supply and constant atmospheric pressure and surface temperature.

- If the energy is enough to evaporate the water stored in plant/tree canopy, then that water is evaporated, and the amount of energy left after this step is computed and saved.

- If the amount of energy left is enough to evaporate surface water, then surface water is evaporated, and the amount of energy left is estimated and saved.

- If the amount of energy left is enough for soil evaporation and plant transpiration, then both processes are computed.

- At any point of the above 4-step ET computation sequence, if the amount of energy available is exhausted, the remaining water storage components are not adjusted. For example, if the energy was exhausted evaporating water stored in plant/tree canopies, then there would be no evaporation of surface water and no evapotranspiration of water from the soil and by plants.

Detailed descriptions are documented in Lai et al. (2019).

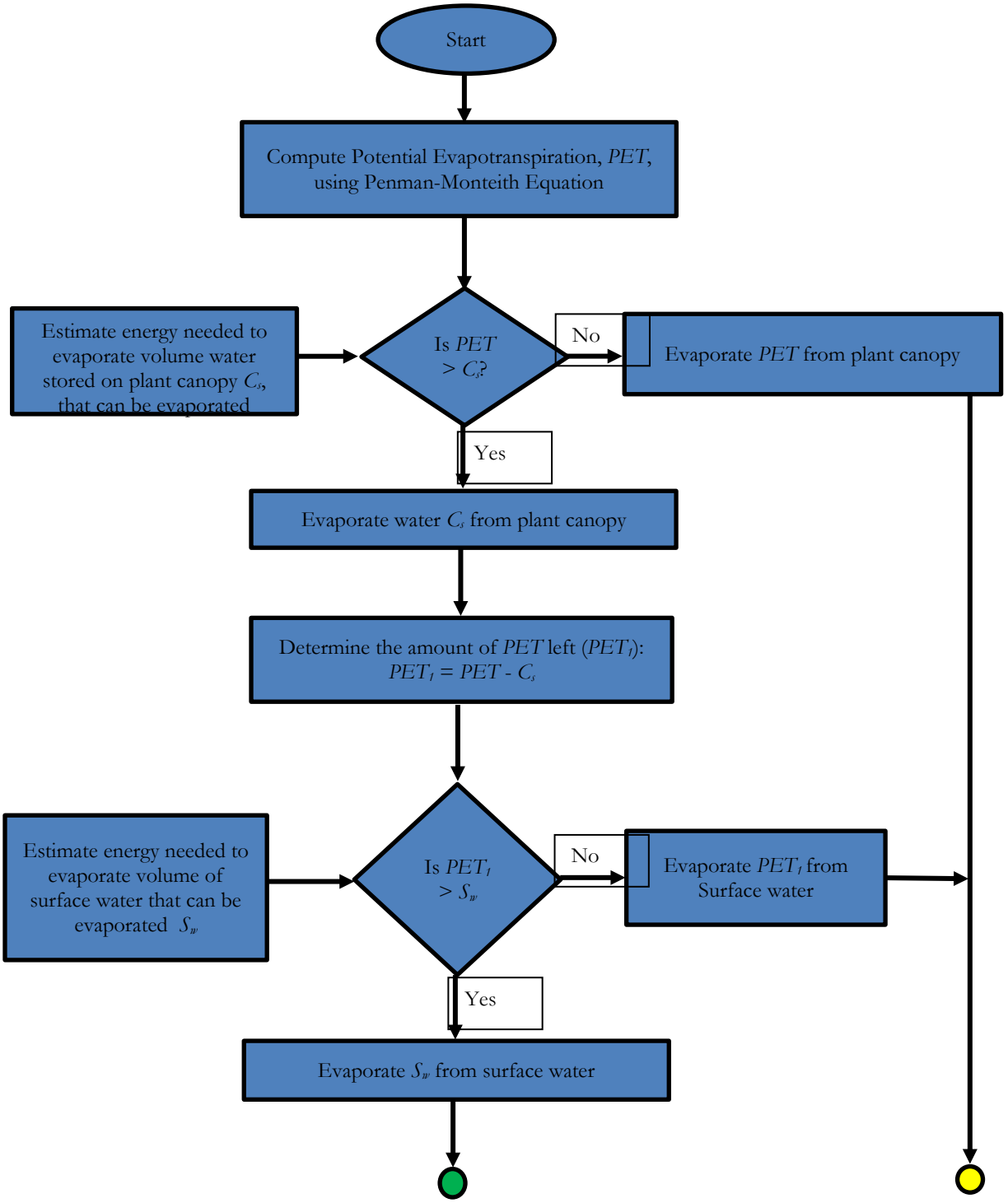
Start
Compute Potential Evapotranspiration, PET, using Penman-Monteith Equation
Estimate energy needed to evaporate volume water stored on plant canopy C_s, that can be evaporated
Is PET > C_s?
No
Evaporate PET from plant canopy
Yes
Evaporate water C_s from plant canopy
Determine the amount of PET left (PET_1): $PET_1 = PET - C_s$
Estimate energy needed to evaporate volume of surface water that can be evaporated S_w
Is PET_1 > S_w
No
Evaporate PET_1 from Surface water
Yes
Evaporate S_w from surface water

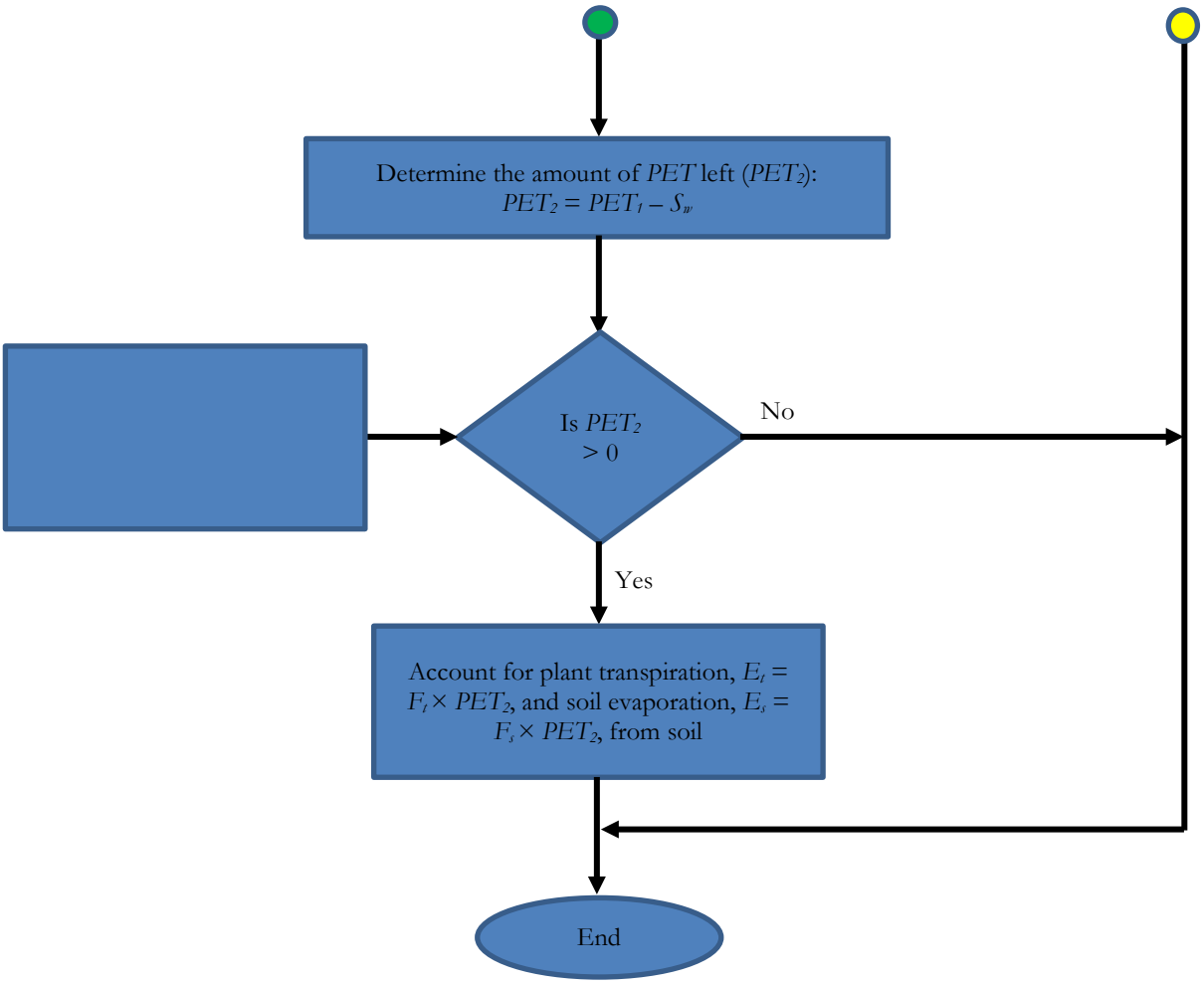

Figure 4.—Flow Chart Illustrating the Steps to Calculate ET. Symbols: PET = potential evapotranspiration; C_s = stored water on plant canopy available for evaporation; S_w = surface water available for evaporation; F_t proportion of soil water available for plant transpiration; F_s = proportion of soil water available for evaporation; E_t = plant transpiration; E_s = soil evaporation.

Erosion and sediment transport module involves complex physical processes and only the basic theory is described herein. Some of the key assumptions adopted by SRH-W in the soil erosion and sediment transport modeling are listed below:

- Erosion from stream banks and gullies are not considered;
- Land elevation changes due to soil erosion and deposition are negligible on overland runoff and erosion computation – this is often a good approximation for event-based simulation,

- Soil properties remains constant in the vertical direction of the bed subsurface; and
- There is unlimited soil supply from the land (i.e., capacity limited) when an area is subject to erosion.

Soils on a watershed and in the channel network may consist of a wide range of sizes in diameters. The characteristics of erosion/deposition and subsequent transport may be vastly different for different size classes. A proper representation of all soil size classes may be important. As a general-purpose model, SRH-W offers two approaches: single-size and multi-size approach. Availability of the multi-size transport is an advantage of the SRH-W as many existing models adopted the single-size approach.

The single-size approach treats all soils in the system as one aggregate having a representative diameter (the notation d_{50} is used though it does not have to be the actual medium diameter). The aggregate may have different erosion and transport properties at different locations. Once detached, however, the aggregate's movement by water is governed by the same mass conservation equation. This approach has been widely used and is appropriate for many applications with large spatial scales and predominantly fine sediments (silts and clays).

The multi-size approach divides soils according to their representative sizes; that is, an arbitrary number of size classes may be used to represent soil particles. For example, soils may be divided into clay, silt, sand, and/or soil aggregates, and the gradation (percentage of presence) is provided at each spatial location of the watershed. Each size class is characterized by its representative diameter, density, and fall velocity; and each is transported separately by flowing water using its own routing equation. The multi-size capability may be needed for applications where fine-scale study questions are of the interest (e.g., impact of local management features), and/or soils consist of widely different sizes. It has been found that the sediment transport capacity was strongly influenced by the sediment size and density (Low 1989; Govers 1992; Guy et al., 2009; Nord et al., 2009). An extensive discussion by Zhang et al. (2011) demonstrated the importance of adopting the multi-size approach.

Two overland erosion processes need to be taken into accounts: splash erosion and runoff erosion.

Splash erosion refers to the detachment of soil particles by falling raindrops. It is an important process at sparsely vegetated areas. It was reported that the energy released at the soil surface in a large rainfall was sufficient to splash more than 200 tons of soil into the air on one hectare of bare and loose soil (UNESCO 2013). Soil particles can be splashed more than 0.5 m in height and 1.5 m sideways. Raindrops can also cause a deterioration of soil aggregates and transform the aggregates into easily erodible loose sediments (Dunne and Leopold 1978). Rainfall induced land surface erosion can be significant with high-intensity rains on steep unobstructed slopes. Such soil losses are

common in arid and semi-arid regions where the sparse vegetative cover has often been disturbed by poor land practices. It is noted that the primary impact of rainfall splash is increased soil detachment rate due to reduced aggregate size, reduced threshold for entrainment, and increased entrainment rate.

For splash erosion, the approach by Gilley et al. (1985), Haan et al. (1994), and Wicks and Bathurst (1996) is adopted. That is, the raindrop detachment, E_{rain} (kg/m²/s), is a function of rainfall intensity as:

$$E_{rain} = K_{rain} C_G C_m I^2$$

where K_{rain} is the soil erodibility factor for detachment by raindrop impact (in kgs/m^4), C_G is a canopy cover correction factor, C_m is a cover-management factor, and I is the rainfall intensity (in m/s). E_{rain} is added as an additional source term to the sediment routing equation and is evaluated at each time step.

Runoff erosion refers to the detachment and subsequent transport of soil particles by the moving surface water. Runoff erosion consists of rill and inter-rill (or sheet) erosion processes. Rills are the concentrated overland flows in micro-relief channels formed in the soil surface; they may produce the greatest amount of soil loss (Dunne and Leopold 1978; Brooks et al. 2013). Inter-rill sheet erosion occurs between rills and is the movement of a semi-suspended layer of soil particles over land surface. Surface runoff quickly becomes concentrated in rills where its erosive power increases with increased water depth. As the flow increases and carries more soil particles, the abrasive action of the particles adds to the erosive power of the surface runoff (Dunne and Leopold 1978; Brooks et al. 2013).

SRH-W adopts the lumped method adequate for non-agricultural watersheds. In this approach, detachment by rill and inter-rill in a lumped manner. That is, an empirical-based erosion equation is adopted to take into account the total and average properties of the erosion and transport processes over an overland area consisting of both rill and sheet areas. In the lumped approach, the processes of soil detachment, movement and deposition are handled such that only the average soil transport rate (flux per unit flow width) is computed on the overland surface. The lumped approach does not distinguish the differences of sheet and rill processes and only the total effective transport rate is computed. With the lumped approach, an empirical sediment transport rate is necessary that relates the net rate of detachment and erosion to variables such as the rainfall intensity or kinetic energy of rainfall, runoff velocity, slope, etc. The lumped approach has been adopted by many existing watershed models.

Two routing methods may be adopted: equilibrium or non-equilibrium method. The equilibrium routing method assumes instant exchanges between sediments in transport and those on the ground surface. As a result, there is no need to solve an additional sediment transport equation, as the sediment rate is made equal to the empirical equilibrium equation. The equilibrium method is the most widely used approach and implemented in most existing watershed models. A drawback of the approach is that sediment transport is highly dependent on the selected

formulation of the equilibrium sediment equation. Sediment delivery to an outlet is only capacity-limited with this approach.

SRH-W adopts the non-equilibrium sediment transport method - i.e., sediment transport rate does not equal the equilibrium sediment transport and has its own governing equation. This approach is more general as it incorporates additional physical processes such as advection by water runoff, dispersion by turbulence, and detachment and deposition processes. Sediment delivery to an outlet may be limited by the transport capacity or the detachment rate (sediment supply limited).

The non-equilibrium sediment routing equation is based on the principle of mass conservation and is expressed on an overland as:

$$\frac{\partial AC_s}{\partial t} + \frac{\partial UAC_s}{\partial x} + \frac{\partial VAC_s}{\partial y} = \frac{\partial}{\partial x}\left(AD\frac{\partial C_s}{\partial x}\right) + \frac{\partial}{\partial y}\left(AD\frac{\partial C_s}{\partial y}\right) + S_C$$

In the above, C_s is volume concentration of a particular size class (non-dimensional), A is flow area per unit width (m), t is time (s), x and y are the horizontal coordinates (m), U and V are the overland runoff velocity components (m/s) in x and y directions, respectively, D is dispersion coefficient, and S_C is sediment exchange rate between sediments in transport and those on the bed (m/s).

For the lumped method, the flow area per unit width (A) is the overland flow depth h (m), but the depth should be interpreted as an average over a sufficiently large lateral distance so that the sediment concentration represents the average contributed from both rill and inter-rill fluxes. SRH-W treats A as local water depth. This means that the watershed terrain represents the average elevation of the combined rill and sheet areas. Note that the above formulation has the potential to reduce to the individualized routing when the mesh is fine enough so that rills and inter-rills are resolved by the mesh. For such cases, of course, different sediment exchange rate should be adopted in the rill and sheet areas.

The non-equilibrium routing equation consists of four terms: the rate of sediment storage, the sediment advection (divergence of the sediment flux), the dispersion, and the detachment and deposition rates. At present, the dispersion is neglected in SRH-W according to the recommendation of Bennett (1974) for overland erosion processes. The storage term is retained although it has been neglected by most existing watershed models. The storage term was regarded small if the variation of flow depth was slow (Haan et al. 1994). The advection term is important as it governs the speed and direction of the sediment transport from one location to another.

The key term in the above equation is the sediment exchange rate which is a primary source of model uncertainty. Options of computing the sediment exchange rate are discussed next.

The formulation for the sediment exchange term is important in the erosion and sediment routing modeling. The exchange term consists of soil detachment and deposition processes and many involve various physical processes. Each process may have to resort to empiricism to develop the appropriate mathematical expression. The accuracy of the sediment erosion prediction depends largely on the accuracy of these expressions.

In SRH-W, the sediment exchange rate (m/s) is computed by:

$$S_C = E_C - D_C$$

where E_C is the detachment rate (m/s) and D_C is the deposition rate (m/s).

The deposition rate for loose sediments in suspension is computed by the approach widely used for suspended sediment routing in streams; that is, it is expressed as:

$$D_C = ahC_s$$

where a is the adaptation parameter (1/s) - reciprocal of the adaptation time. For loose sediments in suspension, the adaptation parameter is related to the sediment fall velocity as:

$$a = \frac{\omega}{\zeta h}$$

where is the sediment fall velocity and ζ is a non-dimensional adaptation constant (a user input). The adaptation constant may range from 0.1 to 1.0 for stream flows; but its value for watershed applications is yet to be determined. The adaptation constant may take different values depending on whether it is net erosion or net deposition; it may also be a function of soil erodibility, erosion resistance (e.g., coved by mulch or not), and clay content. At present, it is treated as a calibration parameter.

The detachment rate depends on several physical processes. In SRH-W, the capacity-based method is adopted, i.e., the detachment rate is equated to the sediment transport capacity or the equilibrium transport rate. This approach has the benefit of simplicity and is consistent with the lumped erosion method adopted (i.e., no separate splash detachment is needed). The capacity equations used in SRH-W are discussed below.

The modified Kilinc-Richardson equation is implemented in the SRH-W model. This equation, in the equilibrium form, has been adopted by a number of watershed models such as Johnson et al. (2000), Ogden and Julien (2002), and Velleux et al. (2005). The original equation was

proposed by Kilinc and Richardson (1973); modifications were made by Julien (1998; 2002) who added to the equation the soil erodibility, cover, and management practice terms of USLE parameters.

With the modified Kilinc-Richardson equation, the total sediment transport capacity on an overland was computed using the unit flow discharge, the slope of the land surface, and three of the six USLE parameters; or it may be expressed as (Johnson et. al. 2000):

$$q_s = 25500 q^{2.035} S_f^{1.664} \frac{KCP}{0.15}$$

where: q_s = capacity sediment rate per unit lateral length (ton/m/s),
q = unit discharge of the overland flow (m^2/s)
S_f = friction slope
K, C, and P = USLE parameters (dimensionless)

The factors K, C, and P may be calibrated with constraints determined by values reported in the widely available literature. These USLE empirical factors have been estimated to represent annual averages of soil loss. Their use in an event-based dynamic model means that they may not be the same as the way they were used by the empirical watershed models.

A further modification was suggested by Velleux et al. (2005) in order to correct the implicit assumption that the threshold for incipient motion is zero. Without correction, the transport capacity will always be greater than zero regardless of the particle size class or the exerted shear stress. Velleux et al. (2005) added thresholds to the modified Kilinc-Richardson equation as:

$$q_s = 25500 (q - q_c)^{2.035} S_f^{1.664} \frac{KCP}{0.15}$$

where q_c is the critical unit flow for erosion.

In general, the sediment transport capacity represents the combined influence on erosion of rainfall intensity, water runoff, and landscape and particle characteristics such as soil erodibility, infiltration, surface roughness, and vegetative cover. Raindrop impact is negligible when flow depths are greater than three times the average raindrop diameter (Julien 2002).

Note that the above equation is not dependent on the sediment size, and capacity rate is interpreted as the rate for the entire aggregate on the land surface. This means the equal mobility assumption is adopted, which means all size classes and aggregates are detached according to their share in the soil layer.

The first step in modeling mercury fate and transport is ascertaining and delineating mercury sources and baseline stores within a watershed. There are several potential sources and species of mercury within a watershed. The different types of species include metallic mercury, cinnabar, mercury chloride, mercury oxide, and anthropogenic metacinnabar. Various conceptual models for the fate and transport of mercury have been developed (see Wang et al., 2017, for a detailed review with emphasis on the processes that affect mobilization and transport). In many parts of the world, atmospheric deposition is a dominant source of mercury to aquatic systems. However, in other regions, e.g., regions with historic mining activities, this deposition can be relatively insignificant compared to mercury transported from other sources (Domagalski et al., 2016) – sources such as soils with mineral cinnabar deposits, geothermal sources, upland sources that have received elevated atmospheric deposition from mining and mercury extraction activities, etc. From a land use/cover perspective, studies suggest that forest vegetation and soils tend to attenuate mercury transport to aquatic systems compared to urban areas. Vegetation facilitates the buildup of mercury concentrations in soils due to the high mercury affinity for associated organic matter. Hence, soils with higher organic matter content tend to collect more mercury over time (Schlüter, 2000). This accumulation, coupled with low runoff and mobilization rates leads to the attenuated transport from forests. Soils with clay minerals and iron oxides have also been shown to also contain larger concentrations of mercury (Obrist et al., 2016).

Baseline spatial stores of mercury may be obtained from the USGS's national geochemical database (Smith et al., 2013) when field measurements are not readily available. For wildfire affected watersheds, these baseline values need to be modified. Undisturbed watersheds generally serve as mercury sinks, with little delivery with runoff. On the contrary, wildfire tends to have a marked impact not only on concentrations on the landscape, but on the delivery with runoff as well. Wildfires release mercury from terrestrial pools into the atmosphere, with soil releases accounting for most emissions followed by burning vegetation. This results in reduced mercury concentrations within the upper layers of the soil. The degree of reduction depends on the severity of the fire. High-intensity, longer duration fires release more mercury compared to low-intensity, shorter duration fires due to more heating and burning. In some instances, high-intensity, long-duration fires can result in the volatilization of all mercury in the top layers. A crucial factor that affects mercury concentration post fire is time. While concentrations markedly decreased immediately following a fire, concentrations increase with time through new atmospheric deposition and sequestration. Compared to unburned soils, the rate of increase in concentration in burned soils is higher due to the presence of ash, which is found to accumulate mercury from atmospheric sources faster. This faster rate is not related to organic matter concentrations, but it is rather hypothesized that fire-induced chemical alterations of carbon compounds in ash lead to greater adsorption of mercury. In all, the importance of accounting for pre-fire concentrations, fire conditions, post-fire inputs, and time elapsed post-fire, cannot be overstated when establishing initial mercury conditions for a watershed simulation.

Several models have been developed to simulate the fate and transport of mercury. These models range from detailed small-scale models that simulate mercury cycling and various species present to coarser, larger-scale models with a cruder representation of mercury exports. The model used for a particular application depends on the problem or question of interest. In this study, we base our approach on the PFHYDRO-WQ model (Wang et al., 2019), developed for larger watersheds to predict total and methyl mercury fluxes associated with soil and sediment transported with overland runoff and streamflow discharge. This approach requires a good initial distribution of mercury concentration for the model – it is assumed that mercury conditions on the landscape do not change over the period of simulation. For cases in which terrestrial mercury concentrations change over the study period, model simulations may be split into periods of quasi-steady terrestrial mercury concentrations. This approach is particularly beneficial for evaluating the effects of fire on mercury delivery several years following the fire event. A model such as FOFEM may be used to predict the initial mercury distributions post fire (Wang et al., 2019).

In this study, the routing of total mercury associated with soils/sediment is based on the mass conservation and expressed as:

$$\frac{\partial AC_{Hg}}{\partial t} + \frac{\partial AUC_{Hg}}{\partial x} + \frac{\partial AVC_{Hg}}{\partial y} = S_{Hg}$$

where C_{Hg} is the concentration of total mercury (µg/m³), A is average flow area per unit width (or average water depth) (m), t is time (s), x and y are the horizontal coordinates (m), U and V are the overland runoff velocity components (m/s) in x and y directions, respectively, and S_{Hg} is the net total mercury exchange rate between mercury in transport and on the bed (µg/m²/s).

The source term S_{Hg} consists of erosion and deposition terms. The erosion rate (S_{HgE}) is assumed proportional to the soil erosion/deposition rate as only mercury sticking to the sediments is the primary mercury source for this study. The net erosion rate S_{HgE} is calculated as follows:

$$S_{HgE} = Hg_{soil}E_{net}$$

where Hg_{soil} is the mass concentration of mercury in the soil (µg/g) and E_{net} is the net erosion rate of the sediment (g/m²/s). The net deposition rate S_{HgD} is based on the assumption of a well-mixed distribution of soil within the water column which is often true for fine soils. The deposition rate S_{HgD} is calculated as:

$$S_{HgD} = -C_{Hg}D_{net}/C_s$$

where D_{net} is the soil deposition rate per unit area (g/m²/s) and C_s is the soil concentration in the water column (g/m³).

Additional source or sink terms may be added to the right-hand side of the transport equation to account for other mercury inputs or losses not represented in the current expression.

The spatiotemporal distribution of methylmercury is much more variable than that of total mercury. Methylmercury is produced from the methylation of inorganic mercury through the action of anaerobic, sulfur reducing microbes. Factors that affect the biogeochemical processes that lead methyl mercury include temperature and redox environments, pH, the presence of organic carbons that serve as electron donors, and the presence of electron receivers such as sulfate and iron (Benoit et al., 2003). Methylmercury concentrations are usually higher during wet periods and in floodplain sediment (Holloway et al., 2009; Wang et al., 2019). There are ongoing studies to better understand the effect of fire on methylmercury concentrations. Previous findings suggest that there is an increase in methylmercury concentration in sediment and biomass after burning (Caldwell et al., 2000; Kelly et al., 2006). Wang et al. (2019) hypothesize that the thermal changes to carbon-bearing particles and formation of sorption-active surfaces during heating enhances adsorption of methylmercury to particles, which would explain the observed increases. According to Krabbenhoft and Fink (2001), methylmercury formation can also be stimulated with the addition of sulfate and labile carbon, which are generated during the soil heating that occurs with burning. For modeling purposes, it is generally beneficial to have available observed data of methylmercury owing to its variability and larger uncertainty compared with total mercury. In this study, we again follow the approach of Wang et al. (2019), which simply uses observed ratios of methylmercury to total mercury to predict time series of methyl mercury fluxes for large watersheds. The observed ratios in Wang et al. (2019) were estimated from water and suspended sediment samples and were found to be 0.002 (0.2%) pre-fire, 0.006 (0.6%) in the year immediately following fire, and 0.0033 (0.33%) two years after fire; the trend showing an immediate increase after fire, which then decreases over time. Herein, we simply multiply the predicted total mercury fluxes with the ratio for a given year to determine the corresponding methyl mercury fluxes.

The numerical methods adopted by SRH-W have been documented by Lai and Greimenn (2019) and Lai et al. (2020; 2022); only some general comments are offered below.

SRH-W adopts the general finite volume discretization method to solve all governing equations. This discretization has the benefit of satisfying the conservation laws locally and globally.

Both explicit and implicit schemes are developed in terms of time advancement of the simulation. The benefit of the explicit scheme is that the solver is relatively simple to implement and the scheme is highly parallelizable. The explicit scheme, however, has a very strict requirement of the time step. The implicit scheme is much more stable and robust and has less restriction on the time step for stability purpose. The implicit method, however, is more difficult to implement and the algorithm is much harder for parallel computing.

A number of important physical processes are two-way coupled and may span a wide range of time scales. Surface flow time scale, for example, may be much faster than the subsurface flow processes. In addition, overland and channel network processes are in different spatial dimension and scales. Different ways of handling the coupling among these physical processes are possible. The two general approaches are widely used in the literature. In a fully-coupled approach, equations governing the surface and subsurface flows are solved simultaneously (e.g., VanderKwaak 1999; Panday and Huyakorn 2004). In the second approach, the governing equations that describe flows in surface and subsurface regions are solved separately and the coupling is accomplished using an iterative method.
SRH-W adopts the iteratively-coupled method. That is, each physical process is solved separately by adopting the latest available results of other processes. The fully coupled method has been promoted by a number of researchers such as by Therrien et al. (2003). The fully-coupled approach may be more stable but can be computationally expensive. The advantages of the fully-coupled method, however, have been argued primarily theoretically, and are yet to be demonstrated in practice.

3. Model Verification

The new model SRH-W has been tested, verified and validated with an extensive list of cases. They are documented in Lai and Greimann (2019) and Lai et al. (2020; 2022). Herein, only a field case is provided to verify that the model is capable of simulating runoff and sediment transport. The selected case is at the Goodwin Creek Experimental Watershed (GCEW).

GCEW is located in Panola County, Mississippi, near Batesville (see Figure 5). It has a size of 21.3 km^2 situated in the bluff hills of the Yazoo River basin of northern Mississippi; the watershed outlet is located at latitude 89°54' 50" and longitude 34 ° 13' 55". It is a tributary of Long Creek that flows into the Yocona River, one of the main rivers of the Yazoo River Basin. The watershed is under research management by the National Sedimentation Laboratory (NSL), Agricultural Research Service (ARS); it has been instrumented extensively so that research was conducted on upstream erosion, stream sedimentation, and watershed hydrology. Relevant research was documented by, e.g., Shields *et al.* (1995), Alonso (1995), Alonso *et al.* (1996). The watershed database consists of runoff, sediment, and precipitation from 1981 to 1996.

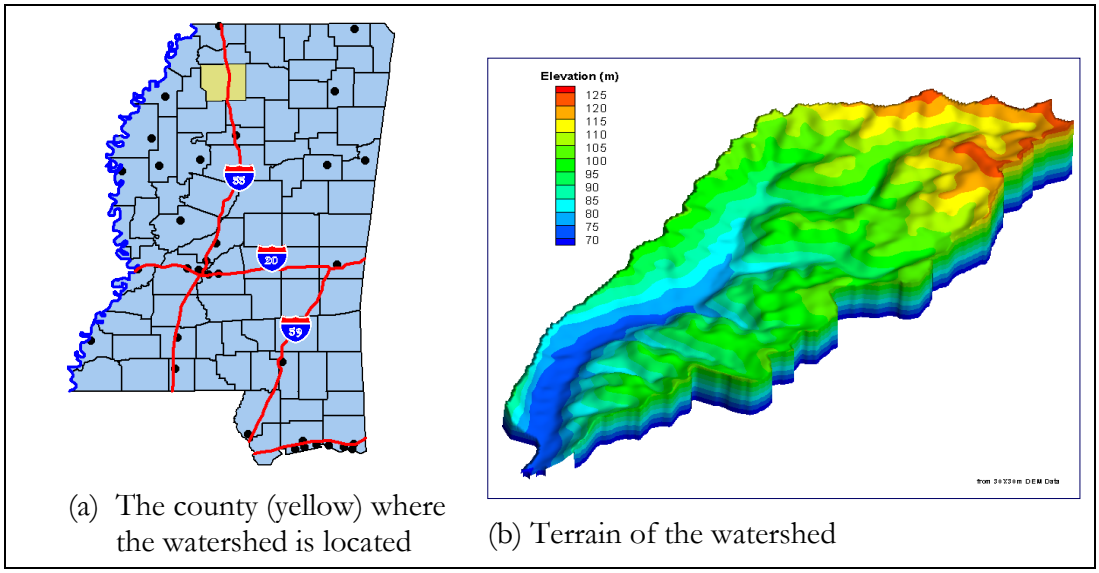

Figure 5.—Goodwin Creek watershed location and its terrain based on 30-m DEM.

The watershed consists of fourteen nested sub-catchments with the drainage areas ranging from 1.6 to 21.3 km^2. At some drainage outlets, flow-measuring flumes were constructed and flow hydrograph and sediment rate data were measured. Terrain elevation varies from 71 to 128 m above mean sea level, with an average channel slope of 0.004 (Figure 5b).

A digital elevation model (DEM) of the Goodwin Creek Watershed is available at a 30-meter resolution, and the data is used for the present study. The terrain was preprocessed first using TOPAZ to obtain a depressionless DEM; the channel network was then delineated from the smoothed 30-m DEM (see Figure 6). The DEM processing procedure was carried out and reported by Sanchez (2002). Four monitoring gage stations are used for model comparison with the measured data in the present study, and they are marked in Figure 6.

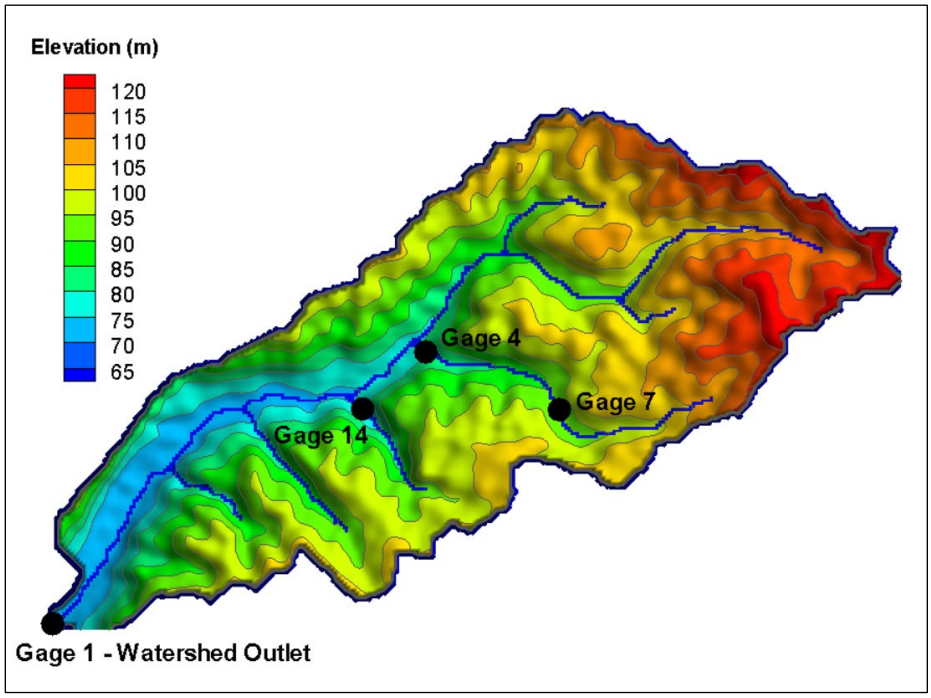

Figure 6.—Smoothed digital elevation model with delineated 1D channel network and the measurement gage stations.

Two major soil associations were mapped at the Goodwin Creek: Collins-Falaya-Grenada-Calloway and Loring-Grenada-Memphis. The Collins-Falaya-Grenada-Calloway association is mapped in the terrace and flood plain areas. These are silty soils, poorly to moderately well drained and include much of the cultivated area in the watershed. The Loring-Grenada-Memphis association is developed on the loess ridges and hillsides. These are well to moderately well drained soils on gently sloping to very steep surfaces and include most of the pasture and wooded area in the watershed. Seven soil types are used for the present modeling and the soil type distribution map is shown in Figure 7. The soil characteristics of each area are described below, based on the report of Blackmarr (1995):

- Calloway (Ca): Fine-silty, mixed, thermic Glossaquic Fragiudalfs; soils are somewhat poorly drained, strongly acid or medium acid silt loam soils formed in deposits of loess in upland positions of low relief (terraces). A fragipan is present generally at a depth of 16 inches.

- Collins (Cm): Coarse-silty, mixed, acid, thermic Aquic Udifluvents; soils are moderately well drained, strongly to medium acid, that have formed in silty alluvium on nearly level bottom lands. These silt loam soils occur primarily along the stream in the bottom area and are the location of much of the cultivation in the watershed. Cotton is the predominant crop but has been supplanted somewhat in recent years by soybeans.

- Falaya (Fa): Coarse-silty, mixed, acid, thermic Aeric Fluvaquents; soil consists of somewhat poorly drained, strongly to very strongly acid silt loam soils that developed in silty alluvium on nearly level bottom land. Most of the Falaya is cultivated.

- Grenada (Gr): Fine-silty, mixed, thermic Glossic Fragiudalfs; soil consists of moderately well drained, strongly to very strongly acid silt loam soils that have developed in thick loess deposits on uplands or terraces. A fragipan is present at a depth of about 24 inches.

- Gullied Land (Gu): Land consists of areas that are severely eroded, severely gullied, or both. The surface soil and much of the subsurface soil has been washed away. Most of this is land that was cleared, cultivated and later abandoned. It is now in trees, idle or pastured. It is unsuited for cultivation.

- Loring (Lo): Fine-silty, mixed, thermic Typic Fragiudalfs; soil series is moderately well drained to well drained, strongly to very strongly acid silt loam soils that developed in thick loess on uplands. A fragipan has formed at a depth of about 30 inches.

- Memphis (Ml): Fine-silty, mixed, thermic Typic Hapludalfs; soil series consists of well drained, strongly to very strongly acid silt loam soils that developed in thick loess on uplands. In Goodwin Creek, this soil occurs as a mixture with the Natchez and Guin or the Loring. This series has no fragipan within the characterization depth; it is predominantly wooded.

- Mixed Alluvial Land (Mx): Land is poorly drained to excessively drained, strongly acid silt loam and coarse sand; no uniformity in the arrangement, depth, color, or thickness of the soil layers. The soil is doughty and very low in organic-matter content and in natural fertility. It is in cultivation (row crops), pasture and trees (hardwoods).

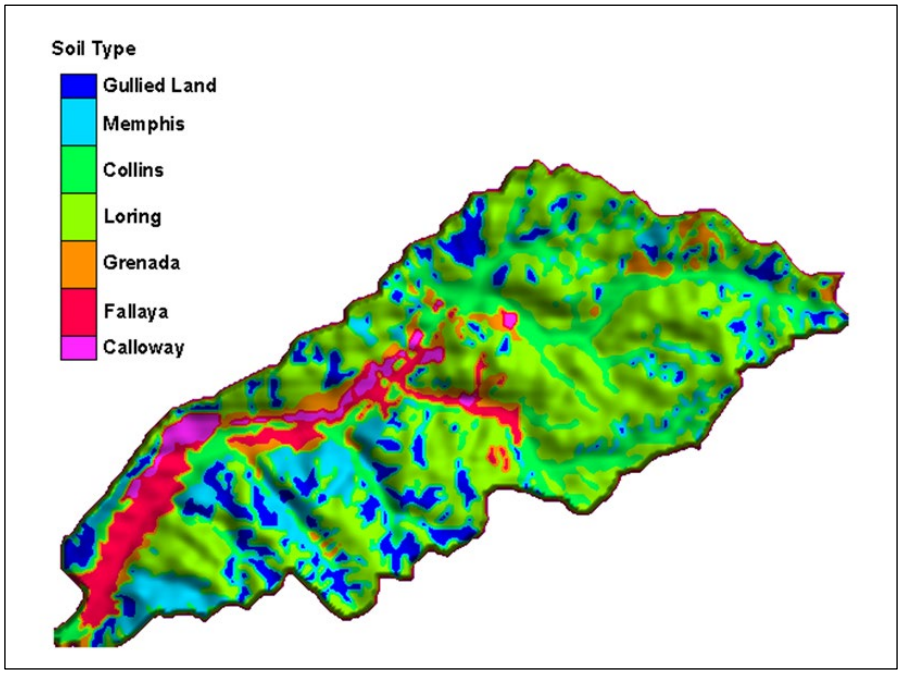

Figure 7.—Soil type distribution map in Goodwin Creek Watershed.

Land use and management practices may influence the rate and amount of runoff and sediment delivered to streams from uplands. The Goodwin Creek Watershed consists of areas ranging from timber land to row crops and is largely free of land management activities. Thirteen percent of its total area is under cultivation and the rest is idle, pasture and forestland. Periodic acquisition of aerial photography and satellite data contributes to a complete aerial coverage of the land use and surface conditions. Land use classification in Goodwin Creek was described by Blackmarr (1995) and summarized below:

- Cultivated Land: consists of three categories: cotton, soybeans and small grain. The field classification is based upon visual confirmation of the crop or by asking the land owner. Types of crops are cotton, soybeans, corn, and small grain.

- Pasture: Classified on the up-keep of the land, the presence of cattle, the presence of fences, and/or asking the land owner.

- Idle Land: Classified on the up-keep of the land, if overgrown with scrub vegetation, the absence of cattle, no fences present, and/or asking the land owner.

- Forest: Classified on the age of the trees, an approximation of age is based on tree height and width which is usually seven years and older.

- Planted Forest: Classified on the age of the trees; as with forest, an approximation of age is based on tree height and width. The range for the classification is from newly planted to seven years old.

In the present study, the land use/land cover is reclassified as forest (includes planted forest), pasture (includes idle land), water, and cultivated. The land use class distribution is based on 30-m resolution data and displayed in Figure 8.

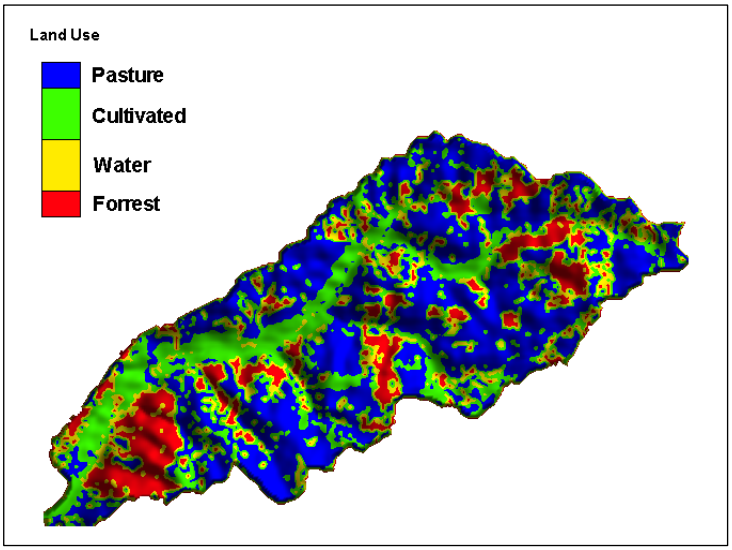

Figure 8. .—Land use class map in Goodwin Creek.

The climate at the Goodwin Creek Watershed is humid and hot in summer and mild in winter. The average annual rainfall during 1982-1992 was 1440 mm and the mean annual runoff measured at the watershed outlet was $14x10^6$ m^3. For the simulated rainfall event, sixteen rain gages recorded the rainfall rate with time and they are used as the precipitation data. These rainfall gages are displayed in Figure *9*.

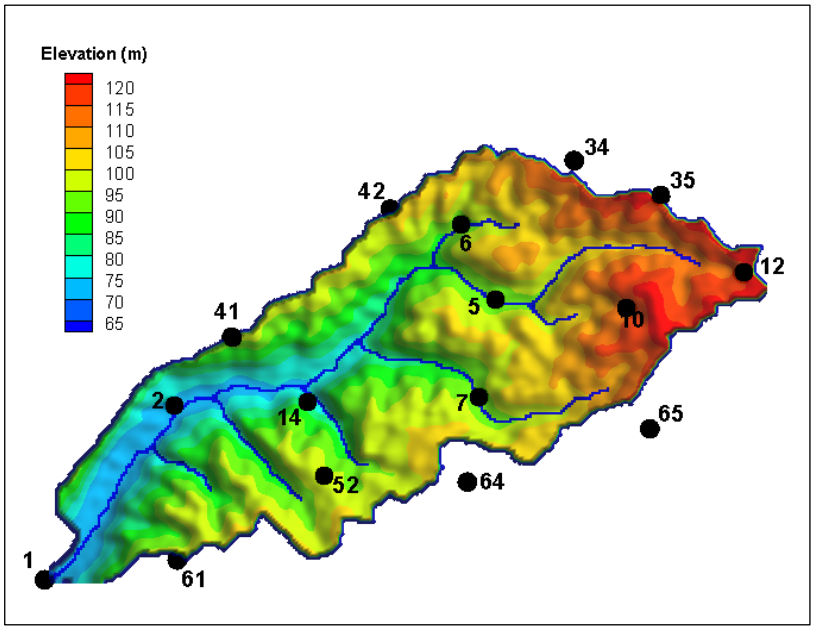

Figure 9.—Locations of all rain gages used for the precipitation input coving the Goodwin Creek watershed.

Channel network was delineated from the smoothed 30-m DEM data and a total of eighteen channel reaches were identified and used by Sanchez (2002) (see Figure 10). In the present simulation, channel reaches are assumed to have the rectangular cross-section, and the channel width and depth vary in different reaches but are constant within each reach. The characteristic cross-sectional geometry in each reach, i.e., the width and depth, was surveyed and compiled by the NSL research team during 978 to 1988. The reported average channel width and depth in each of the eighteen reaches are listed in Table 1 (Backmarr 1995); they are used in the present simulation. It is noted that the terrain elevation along the channel, which is in the DEM and used by the 2D overland solver, represents the channel bank-full elevation. Therefore, the channel depth subtracted from the channel bank-full elevation determines the channel bottom elevation.

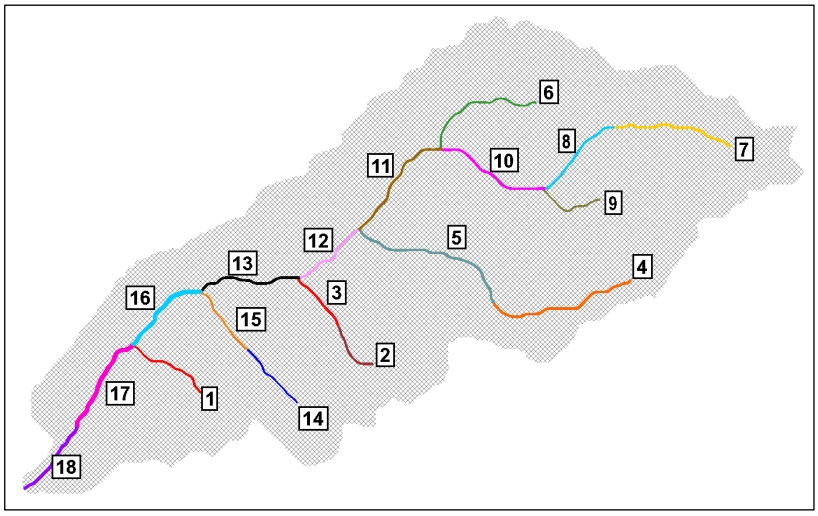

Figure 10.—Delineated channel network and the reach IDs in Goodwin Creek.

Table 1.—Channel reach properties (width, depth and the Manning's roughness coefficient)

Reach ID	Width (m)	Depth (m)	Manning n
1	25	3.5	0.0648
2	20	3.0	0.0648
3	22	3.5	0.0648
4	27	4.3	0.0648
5	28	3.1	0.0648
6	30	3.4	0.1296
7	30	3.55	0.0648
8	22	4.1	0.054
9	29.4	4.2	0.0648
10	26	4.35	0.054
11	30	4.4	0.054
12	22.4	4.0	0.054
13	27	4.3	0.054
14	30	4.5	0.054
15	30	4.7	0.054
16	50	5.0	0.0648
17	48	5.0	0.0648
18	34	6.05	0.0648

The storm event of October 17, 1981 is simulated. The precipitation event began at 9:19 pm and had a rainfall duration of 4.8 hours. There was very little rainfall preceding this event – so initially dry condition is applied on the watershed. Precipitation data were from sixteen rain gages (see Figure 9 for locations). The recorded rainfall intensity time series at all gages (30-minute averaged) are the precipitation input and displayed in Figure 11. For the event, the total rainfall depth varied from 66 to 78.7 mm with an average value of 73.6 mm. The average rainfall intensity was 0.58 in/hr (or 14.7 mm/hr) with a maximum of 2.03 in/hr (or 51.6 mm/hr).

Other model input data include: the watershed terrain interpolated onto the 2D mesh from the 30-m DEM, spatial distribution of the watershed properties of the soil types and the land use, and relevant parameters associated with each soil type and land use class. The terrain, soil type and land use maps are discussed earlier; the specific model parameters associated with each soil type and land use class are discussed next.

For each soil type, the key runoff simulation input is the infiltration properties as the Hortonian runoff is adopted with the Green-Ampt model. Three infiltration parameters are needed for each soil type: the saturated hydraulic conductivity, the suction head, and the moisture content deficit. The first two were taken from the estimation by Rawls et al. (1983); the last (moisture content deficit) was assumed uniform on the watershed as no data were available, according to Sanchez (2002). The three infiltration parameters used by the model are listed in Table 2.

For erosion simulation, each soil type has other input parameters specified; and they are listed in Table 3. Each land use class has the following input parameters: the Manning's roughness coefficient, the rainfall interception depth, and C_{USLE}. The values used are listed in Table 4. Other model inputs include the following:

- Modified Kilinc-Richardson equation for overland
  - Three sediment sizes are used

- Engelund-Hansen transport equation in the 1D channel network
  - The channel is assumed non-erodible though deposition is allowed

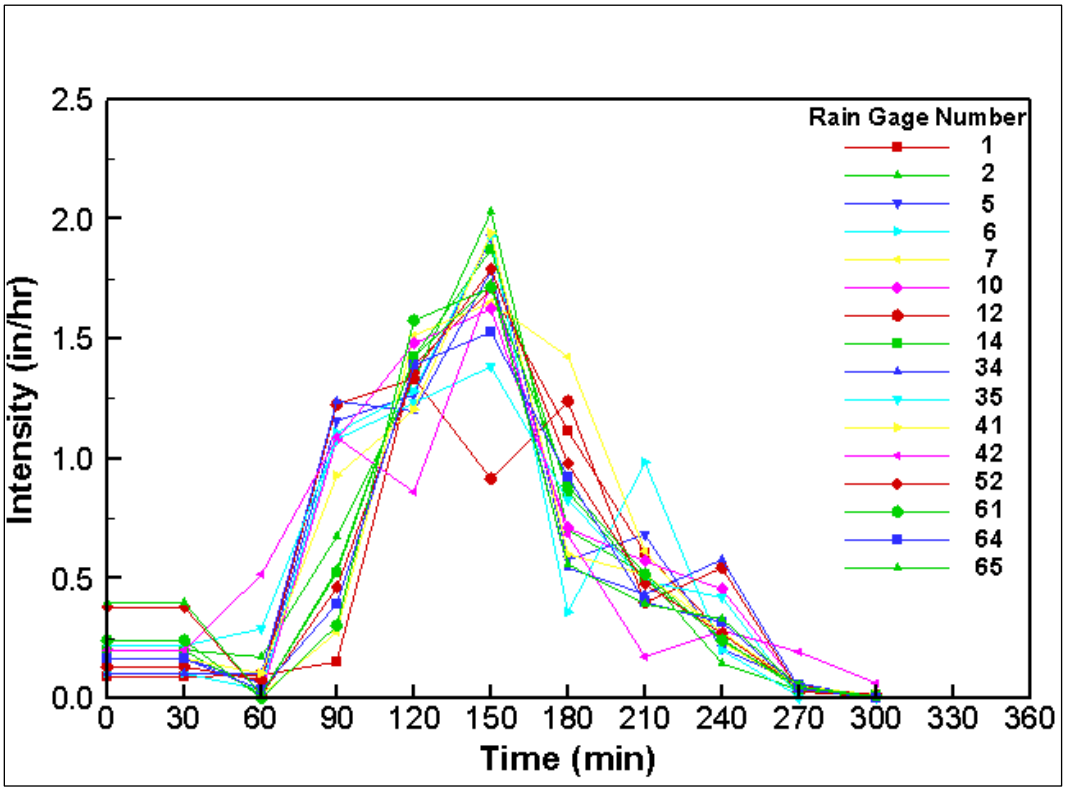

Figure 11.—The rainfall intensity time series and locations of the sixteen rain gages for the event of Oct. 17, 1981 at Goodwin Creek.

Table 2.—Infiltration parameters for each soil type at GCEW

Soil Type	Drainage Condition	K_s (cm/hr)	Ψ_f (cm)	$\theta_s - \theta_i$ (cm^3/cm^3)
Calloway	Poor	0.32	18	0.33
Fallaya	Poor	0.30	14	0.33
Grenada	Moderate	0.35	17	0.33
Loring	Mod/Well	0.38	22	0.33
Collins	Mod/Well	0.37	19	0.33
Menphis	Well	0.40	22	0.33
Gullied Land	Poor	0.25	10	0.33

Table 3.—Soil erosion parameters for each soil type at GCEW

Soil Type	K_{USLE}	Soil Gradation (%)		
		d_1	d_2	d_2
Calloway	0.4	20	55	25
Fallaya	0.1	20	55	25
Grenada	0.2	10	60	30
Loring	0.4	20	55	25
Collins	0.4	20	55	25
Menphis	0.1	10	60	30
Gullied Land	0.1	20	55	25

Table 4.—Land use parameters for each land use class at Goodwin Creek

Land Use Class	Roughness n	Interception (mm)	C_{USLE}
Forest	0.20	1.5	0.0005
Water	0.01	0.0	0.0
Cultivated	0.08	0.8	0.02
Pasture	0.12	1.0	0.018

The hybrid mesh with mixed quadrilateral and triangular cells is used for simulation. The reason is that such a mesh may be easily generated using the SMS software and maintains a good representation of the 1D channel and 2D overland at the same time. The final mesh is show in Figure *12* – the mesh consists of 37,839 cells (25,812 quads and 12,027 triangles). The development of the mesh follows the following procedure:

- The mesh representing the 1D channel network follows naturally the channel longitudinal location while only one cell is used across the channel width in the lateral direction.

- In SRH-W approach, the locations of the left and right banks of the channel are needed but not critically important as results are not sensitive to its choice. The 2D cells that represent the 1D channel network serve only to facilitate the implementation of 1D-2D coupling. The terrain of the 2D cells within the 1D channel is not used by the 1D channel solver. The actual 1D channel geometry is specified by a separate input which specifies

the actual geometry of the 1D channel cross sections. In general, the elevation of the 2D cells of the channel network may represent the bankfull elevation or simply the water surface elevation at the time of the terrain survey for DEM development.

- The 2D overland mesh is generated using the automatic feature of the SMS software, based on the watershed boundary and the 1D channel network bank lines. The mesh resolution of the GCEW mesh is such that the edges of the mesh cells are approximately 30 m to match the DEM data resolution. Mesh resolution finer than the terrain data is not recommended as no new terrain information is included by such a fine-resolution model. Our experiences show that model results are not improved by using a mesh whose resolution is finer than the DEM.

Once the 2D mesh is developed, the terrain surface elevations at mesh points are resampled from the 30-m DEM using the bi-linear interpolation algorithm. The soil type and land use class may have been in any resolution in its original form; they are also interpolated onto the 2D mesh for modeling.

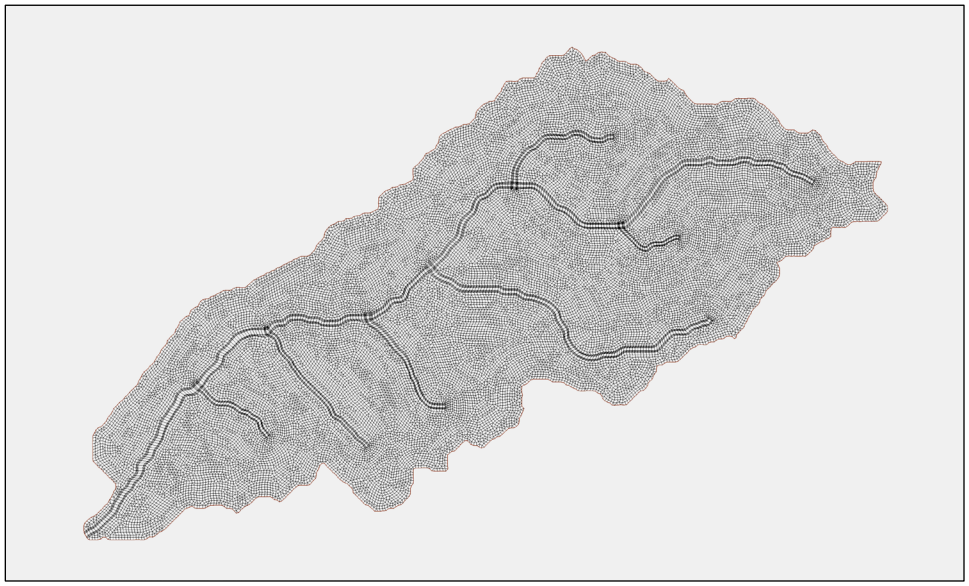

Figure 12.—The 2D hybrid mesh developed for the simulation of GCEW.

Simulation is carried out using the implicit 2D overland solver with a time step of 15 s and the explicit 1D diffusive-wave channel network solver with a time step of 0.125 s.

The predicted flow runoff hydrographs at four gage stations are compared with the measured data in Figure 13. At the watershed exit (gage 1), the predicted peak runoff and time-to-peak, i.e., the rising limb, match the measured data well; but the runoff during the recession (the falling limb) deviates slightly from the measured data. The overall result is satisfactory at the watershed exit. At other three internal gage locations, the rising and falling limbs of the runoff hydrograph and the time-to-peak are also predicted reasonably. The peak discharge, however, is underpredicted. The larger under-prediction of the peak runoff rate is observed to be associated with smaller sub-catchments. The discrepancy, therefore, may be attributed to the inaccuracy of the precipitation data. The other primary source of error is the local infiltration simulation. For small sub-catchments, high uncertainties in model input data or local mesh distortion may be translated into high uncertainties in model outputs. The impact is normally less in larger catchments. Therefore, we suspect that the large discrepancy was due to the high uncertainty of input data in small sub-catchments.

Spatial distributions of the precipitation intensity and the simulated water depth over the watershed are displayed in Figure 14 and Figure 15 at different times. The figures show the advantage of the mesh-distributed watershed model in that detailed information may be visualized which may be used to identify where the runoff has the highest rate at a given time. The information may be used to help evaluate the impact of different land use and management practices on runoff.

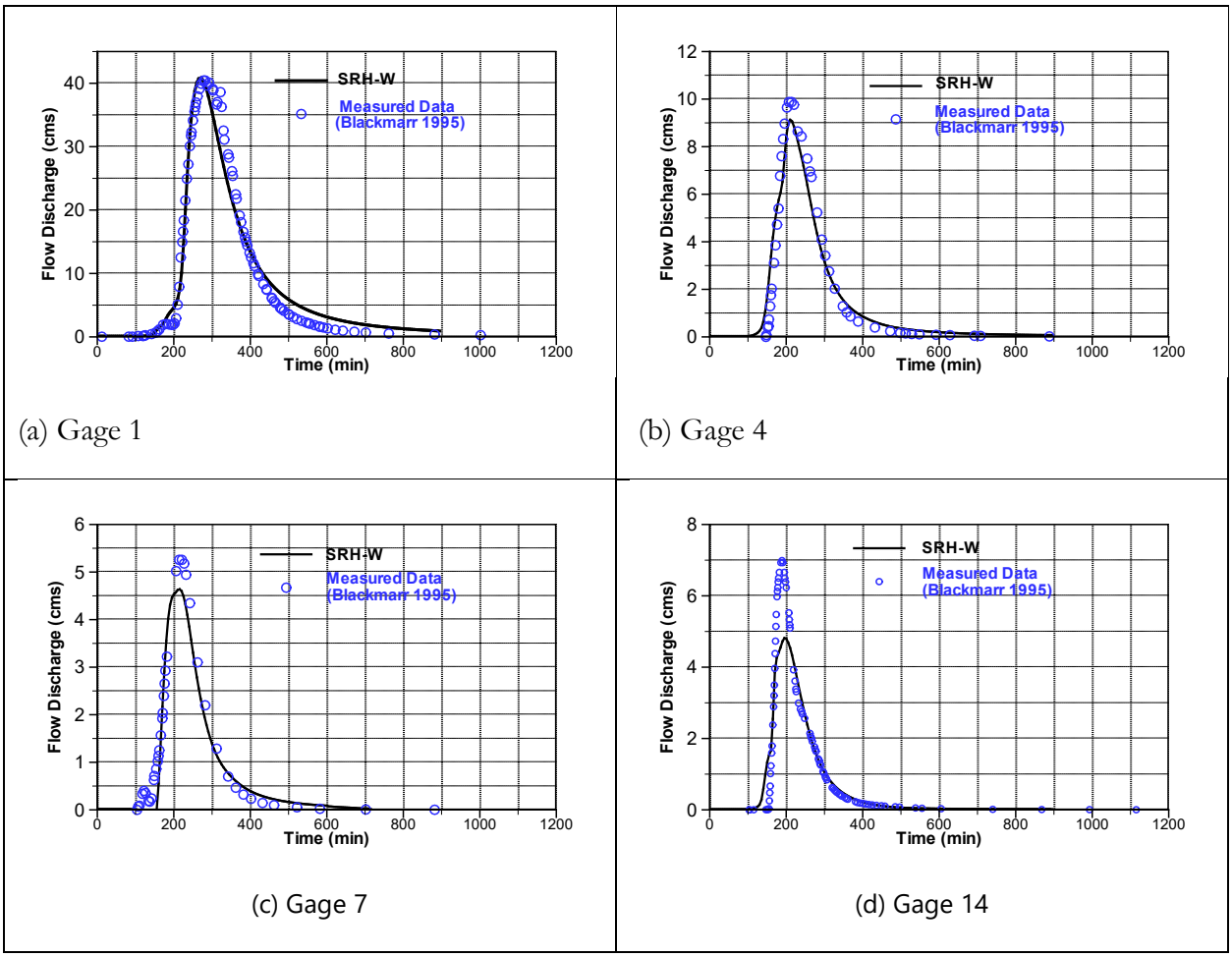

Figure 13.—Comparison of predicted and measured runoff hydrographs at four gage stations with the model with the 1D-2D coupling.

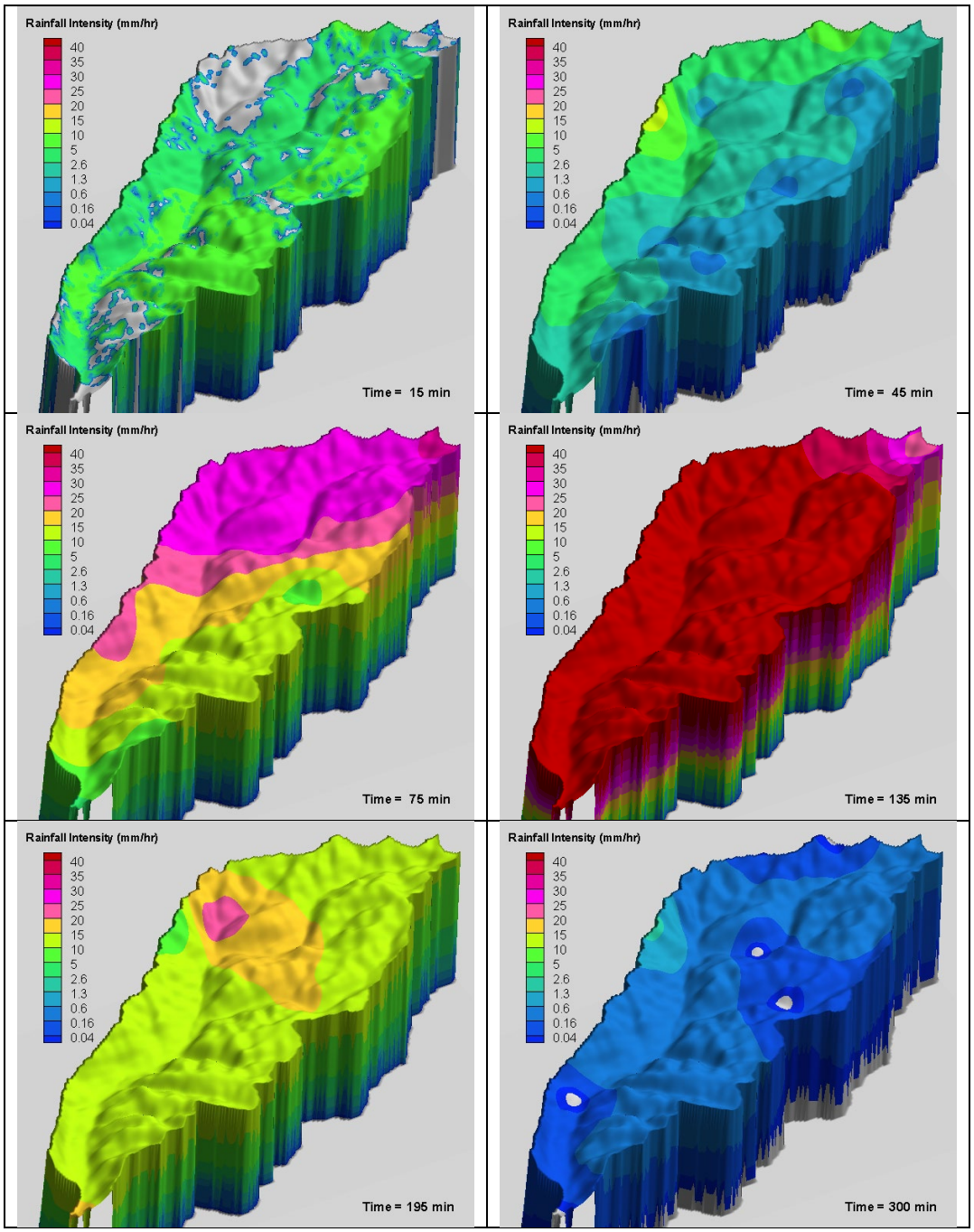

Figure 14.—Spatial distribution of the rainfall intensity at different times of the precipitation event.

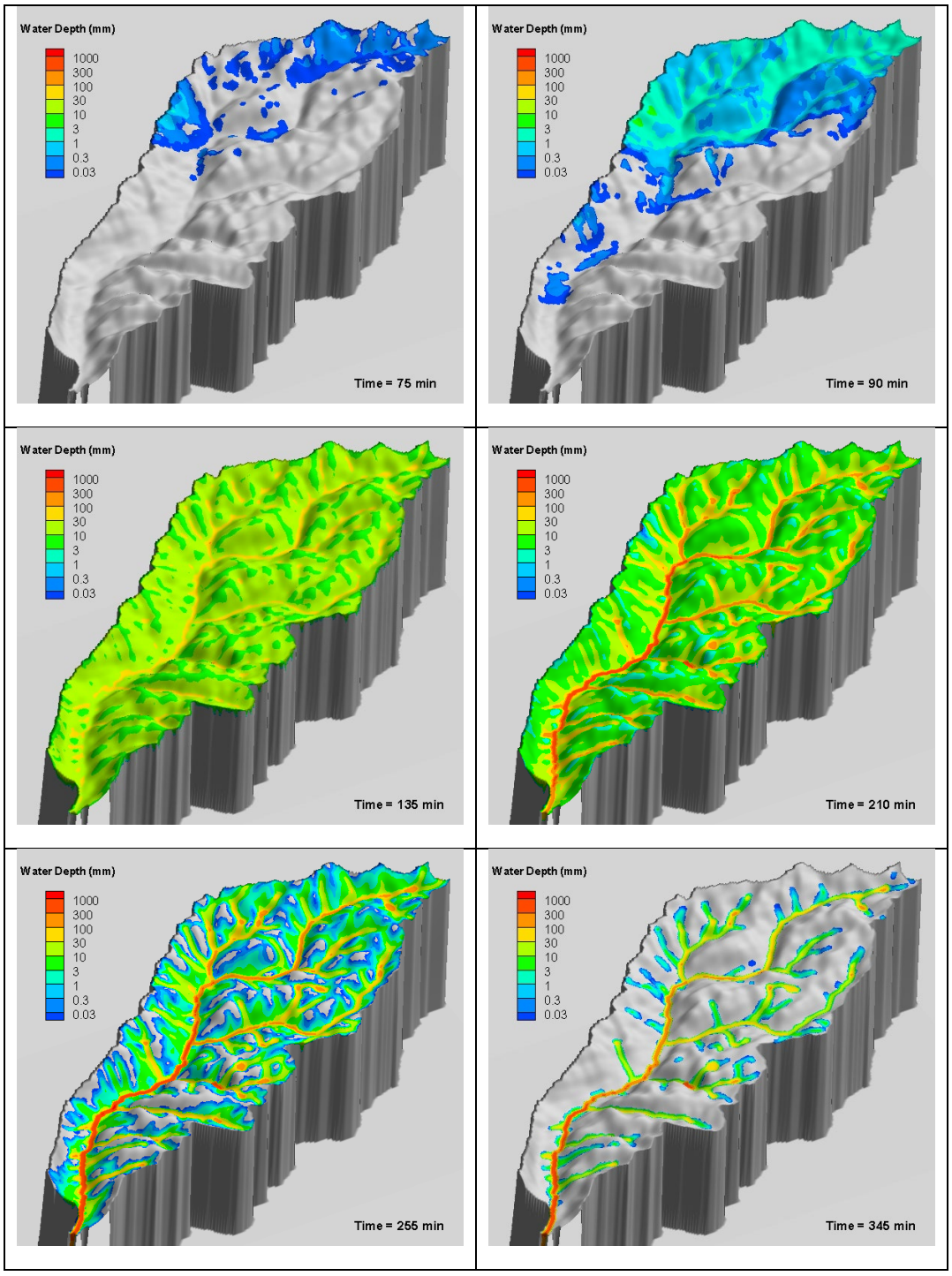

Figure 15.—Spatial distribution of the predicted water depth at different times of the precipitation event.

Next, erosion and sediment transport results are discussed. Note that the runoff results should be the same as the runoff-only simulation reported above, as the overland terrain changes are assumed negligible.

The predicted and measured sediment rates at the four gage stations are compared in Figure 16. Overall, the model predicts the volume and the shape of the sediment rate, but the peak is delayed at the watershed outlet (gage 1). The model under-predicts the sediment rate significantly at other gages. The model consistently predicts delayed response of the sediment rate at the gage stations in comparison to the flow hydrograph. However, the time to peak for the sediment rate is earlier than that for the flow hydrograph based upon the measured data at most gage stations. The specific reason why the peak of the sediment rate precedes the peak of the flow rate is unclear, but it is not unusual for the sediment transport rates to be significantly higher on the ascending limb of the hydrograph than on the descending. For most internal gage points, the rising limb of the sediment graph is predicted but not the falling limb. The peak is significantly underpredicted and the reason is unclear. A number of factors may contribute to the differences. In addition to similar differences associated with the flow hydrograph for small sub-watersheds, the channel bank erosion and land slide may also contribute to the differences. Gully erosion on the sub-watershed is possible but not considered by the model, which was known to happen at the site. Another potential source of sediment delay may be due to the nature of the sediment transport on the overland: the model assumes unlimited sediment supply on the overland which may not be true everywhere. In summary, the predicted and observed sediment rates are generally of the same order of magnitude, which is decent for sediment predictions.

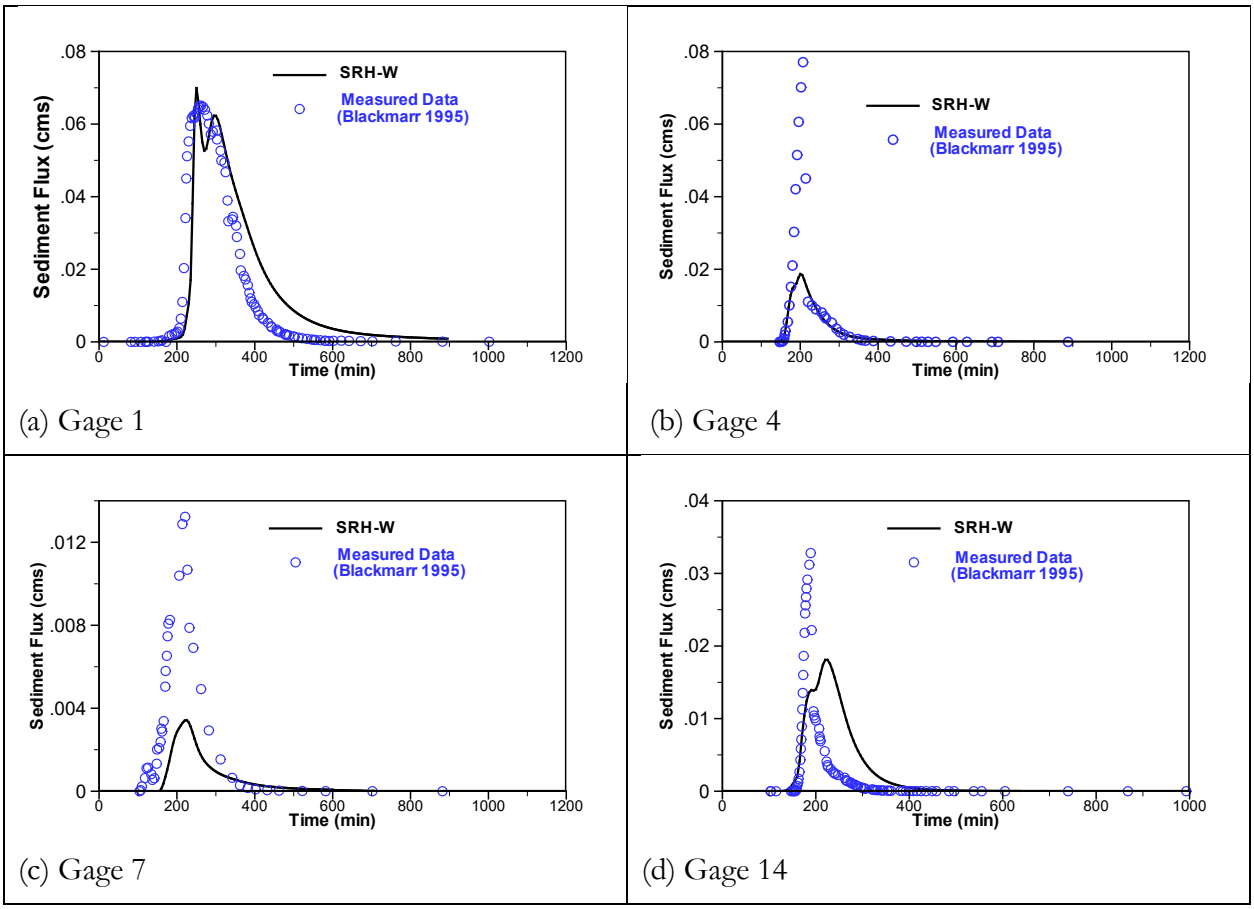

Figure 16.—Comparison of predicted and measured sediment flux at four gage stations with the model using the 1D-2D coupling.

4 Model Validation

Herein another field case modeling is carried out focusing on mercury transport. The results of water runoff, sediment movement and mercury transport at the Cache Creek Watershed, CA, are presented.

4.1 Water Runoff and Sediment Results

4.1.1 Watershed Overview

The Upper Cache Creek Watershed covers portions of Lake County, Yolo County, and Colusa County in northern California (Figure 17). It has an area of 3,017 km², with elevations ranging from approximately 0 to 1,800 meters. This region does not experience significant amounts of snowfall. Like several other watersheds in California, the watershed has been subject to major wildfire events in recent years. Data suggests that wildfires have become more severe and there is a need for examining the impacts of these events on runoff, sediment yield and total mercury delivery. For example, the Jerusalem and Rocky fires together burned about 214 km² within the Upper Cache Creek watershed between July to August 2015. The intensity of the fires varied across the watershed, resulting in spatial variability in the effects on soil properties and vegetation cover. This watershed has been the focus of other past modeling studies by, e.g., Stern et al. (2016) and Wang et al. (2019; 2020).

The simulation domain is a gauged 282 km² sub-watershed of Upper Cache Creek in which approximately 163 km² burned (see Figure 17). Previous simulations have been performed on this sub-watershed using the lumped models of HSPF and PFHydro (Wang et al. 2019). The same model simulated by PFHydro is adopted, as the same boundary conditions may be applied with the present mesh-distributed modeling using SRH-W. Two pre-fire runs (2000 and 2015) and two post-fire runs (2016 and 2017) are carried out for runoff. The sediment transport and delivery are then simulated for one pre-fire (2015) and two post-fire (2016 and 2017) scenarios. In contrast with PFHydro, SRH-W used the physically-based sediment model of the Kilinc-Richardson approach (Kilinc and Richardson, 1973).

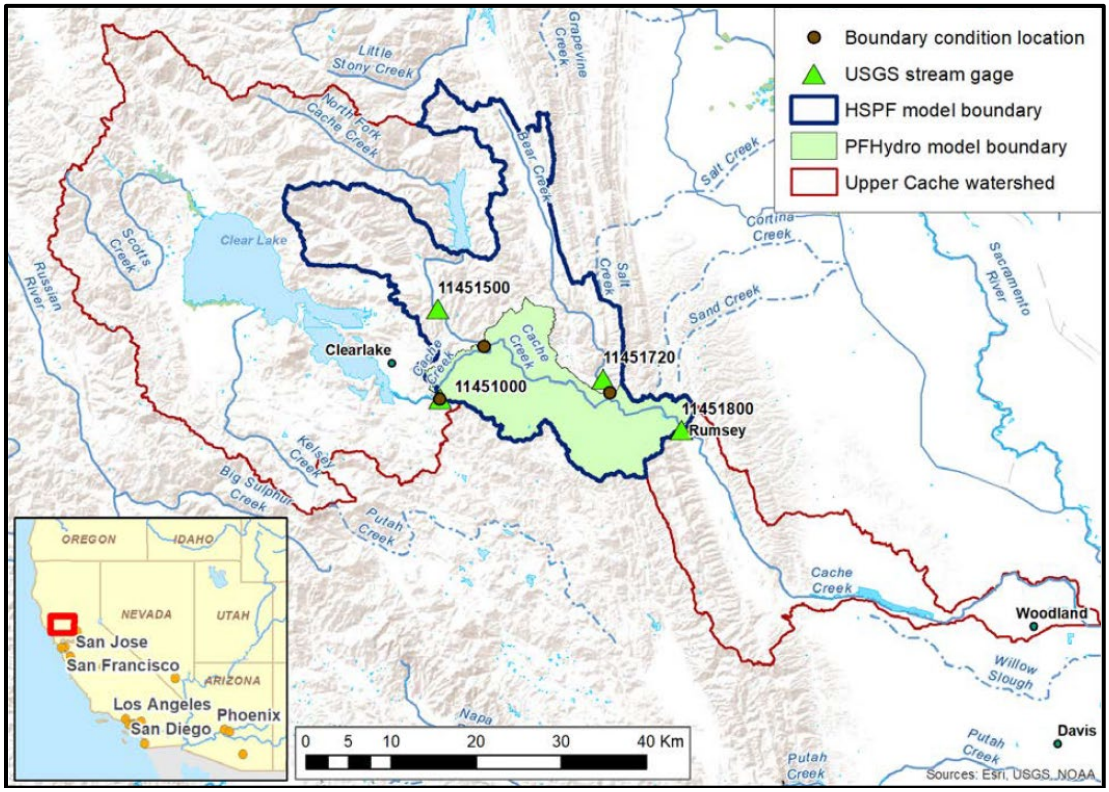

Figure 17.—Upper Cache Creek Watershed in Northern California. Modeled Cache Creek Watershed (in green) shown within the Upper Cache Creek HUC-8 watershed (Figure courtesy of Wang et al. 2019). Shown on the figure is a previously modeled HSPF domain (Stern et al. 2016) and the USGS stream gauge and model boundary condition locations.

4.1.2 Terrain and Mesh

The terrain is from the Shuttle Radar Topography Mission (SRTM) 1-arcsecond digital elevation model (DEM) (USGS 2014); the DEM was reprojected into the State Plane California II coordinate system using ArcGIS and then resampled to a size of 30 meters for use by the SRH-W model. The terrain was further preprocessed in GIS to obtain a depression-less (filled) DEM, and the channel network and watershed were then delineated. The terrain elevation overlaid on a hillshade of the watershed is shown in Figure 18.

A 2D hybrid mesh (mixed quadrilateral and triangular cells) was developed for mesh-distributed modeling; it consists of 9,712 cells (8,998 triangles and 714 quads) as shown in Figure 19. The development of the mesh follows the following rule:

- Both overland and channel network are represented by the 2D mesh cells.

- The channel network was represented by quad cells only along the direction of the river network (i.e., in the longitudinal direction) with only one lateral cell. The width represented the potential flow extent including both channel and floodplains and ranged between 50 m to 75 m.

- The overland mesh was automatically generated using the SMS software with a given resolution. The cell size ranged between approximately 100 m and 500 m (hillslope scale).

Once the 2D mesh was generated, the terrain elevations at mesh points were resampled from the 30-m DEM using the bi-linear interpolation algorithm. The spatial distribution of key watershed properties, such as soil type, land use class and fire burn severity, were then populated onto the 2D mesh cells automatically by the model.

Three USGS flow gauge stations are located close to the boundary of the simulated sub-watershed (see Figure 17). One upstream gauge is at Cache Creek near Lower Lake, CA (USGS) 11451000; the other at Bear Creek near Rumsey, CA (USGS 11451720); and the downstream gauge is on Cache Creek at Rumsey, CA (USGS 11451800). An additional boundary condition is needed on the North Fork of Cache Creek that does not have a gauge. For this location, the time series flow data were from the calibrated HSPF model.

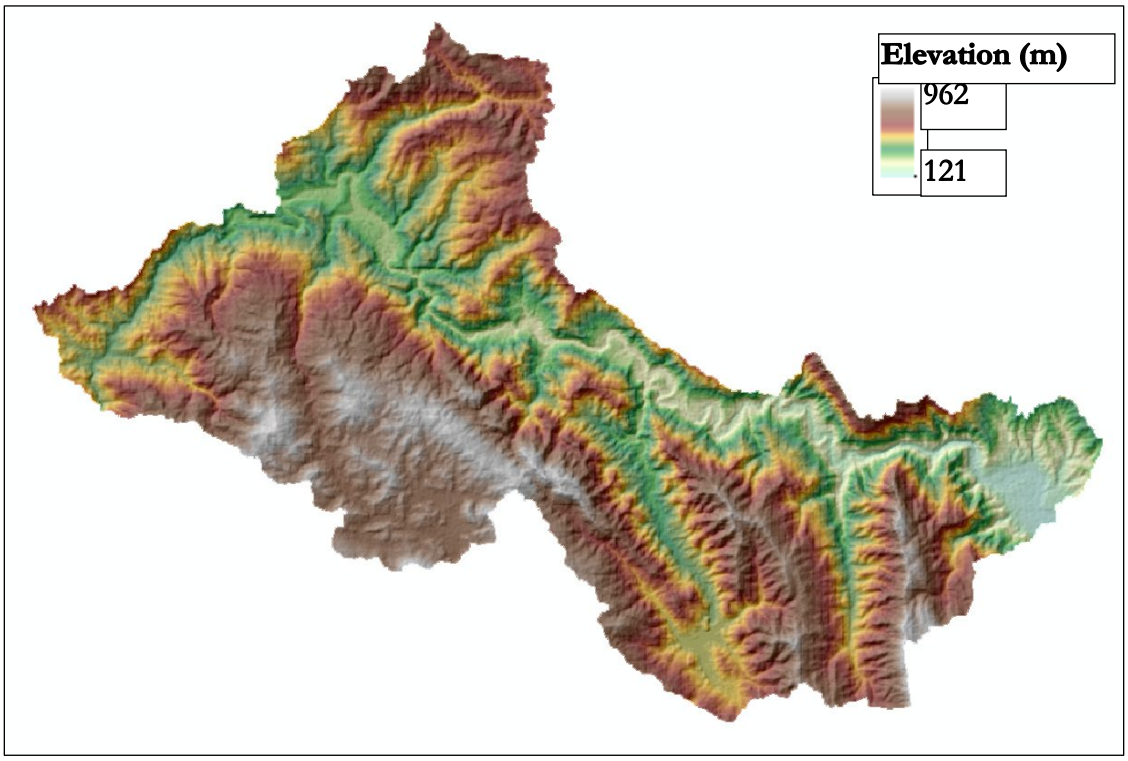

Figure 18.—Terrain Elevation Ranges of the Upper Cache Creek Overlaid on a Hillshade of the Sub-Watershed.

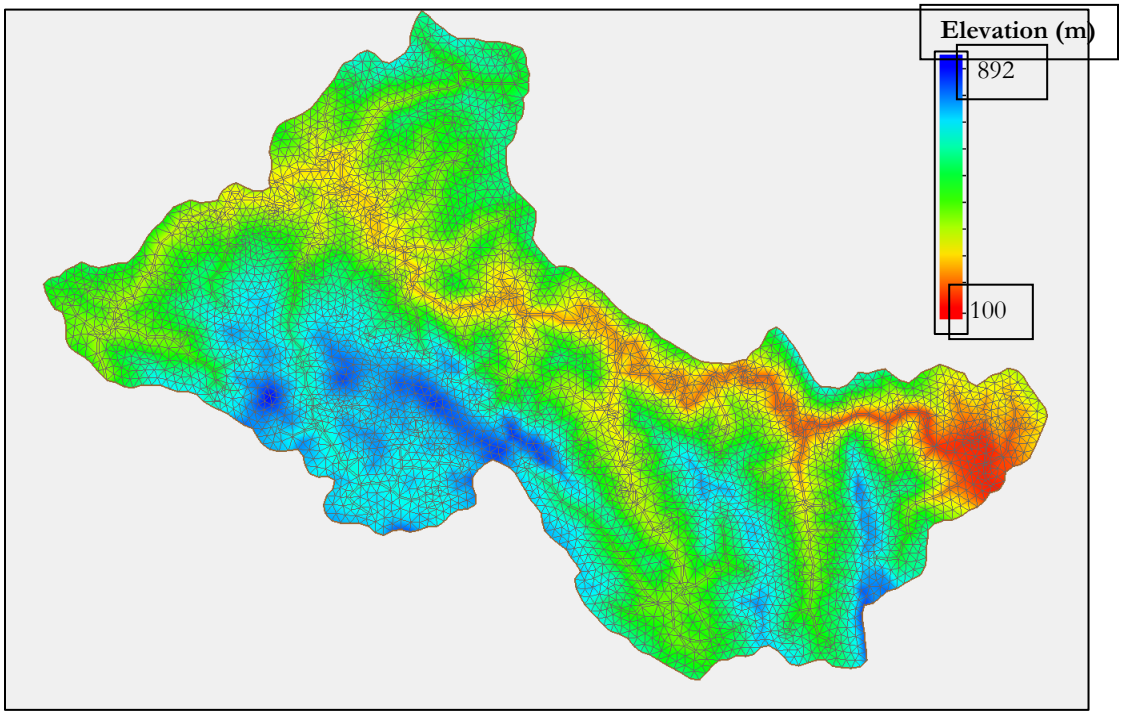

Figure 19.—CCW Computational Mesh Comprising 2D Triangular Elements for Overland and Quadrilateral Elements for the Channel Network.

4.1.3 Land Cover Class and Burn Severity

Pre- and Post-Fire land cover class data were from two Landsat 8 images. The pre-fire image was taken on 07/27/2015 and the post-fire image on 09/04/2015. Land cover class was categorized into seven classes: low vegetation, mixed trees and grass, mixed trees and shrubs, trees, bare earth, impermeable surfaces, and surface water. The spatial distribution of the land cover class is shown in Figure 20 under both pre-fire and post-fire conditions. Per Wang et al. (2019), the mixed trees and shrubs class was estimated to contain approximately 50% trees and 50% short vegetation, and the mixed trees and grass class was estimated to contain approximately 30% trees and 70% short vegetation.

The fire burn severity varied considerably spatially (Wang et al. 2019). The Rocky fire burned from 07/29/15 to 08/14/15 and the Jerusalem Fire burned from 08/09 to 08/25/15, with the two merging on 08/12/15. A satellite-derived layer of post-fire vegetation conditions, known as the Burned Area Reflectance Classification (BARC), was used to delineate burn severity and shown in Figure 21. BARC is based on a relationship between near- and mid-infrared reflectance, and classifies burns into high, moderate, low, and unburned (USFS Geospatial Technology and Applications Center, 2022). Statistical analysis of the layer indicates that 42.1% of the modeled domain was unburned, and 12.5%, 38.5% and 6.9% experienced low, moderate and high burn,

respectively. A summary of the percentages of land cover classes, pre- and post-fire, is provided in Table 5. The calibrated canopy coefficients and depression storages for the classes are also presented in Table 6. An average manning's roughness coefficient of 0.03 was used for the channel network, while average values ranging between 0.04 and 0.06 were used for the uplands.

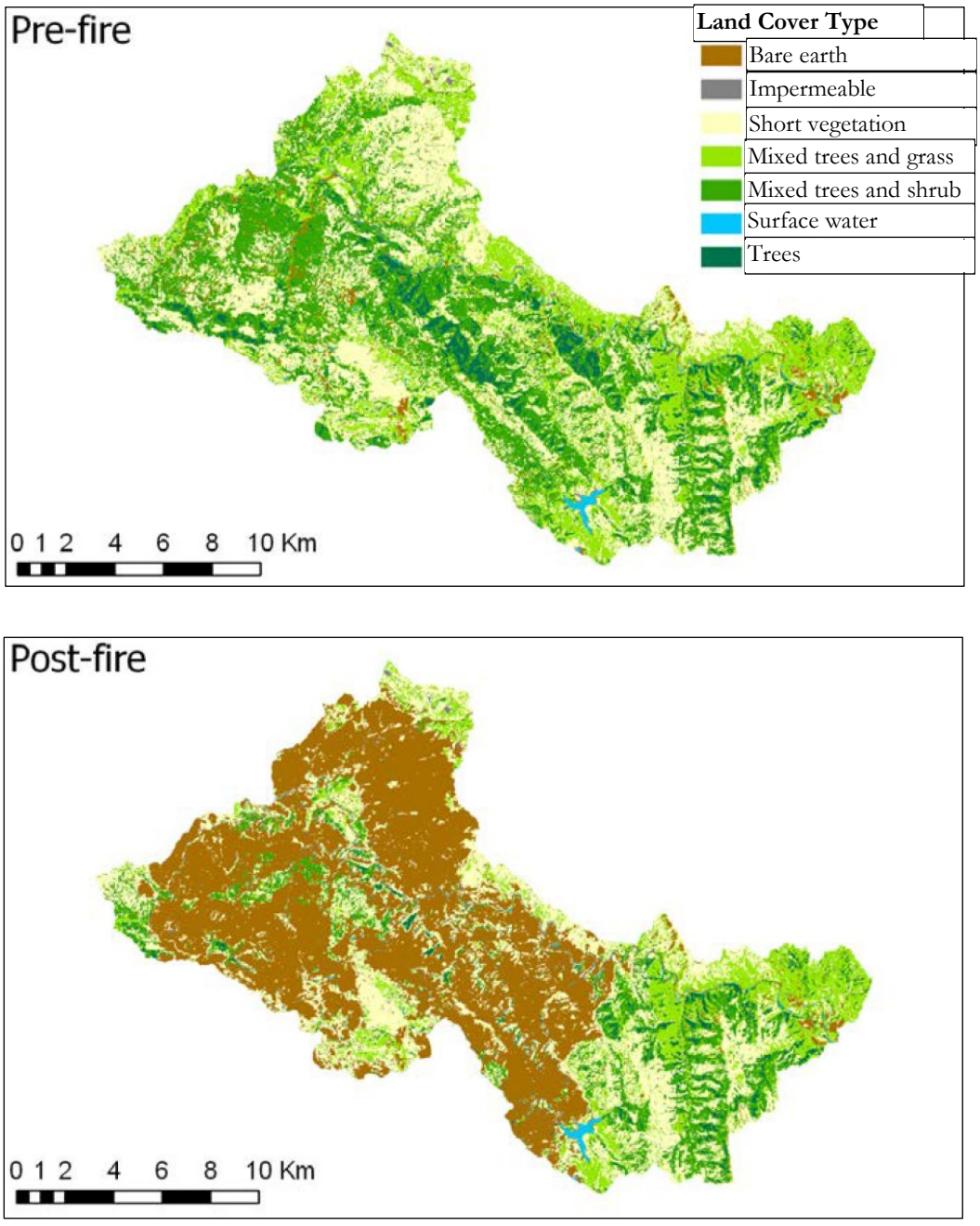

Figure 20.—Pre- and post-fire land cover distributions in Upper Cache Creek (Wang et al., 2019).

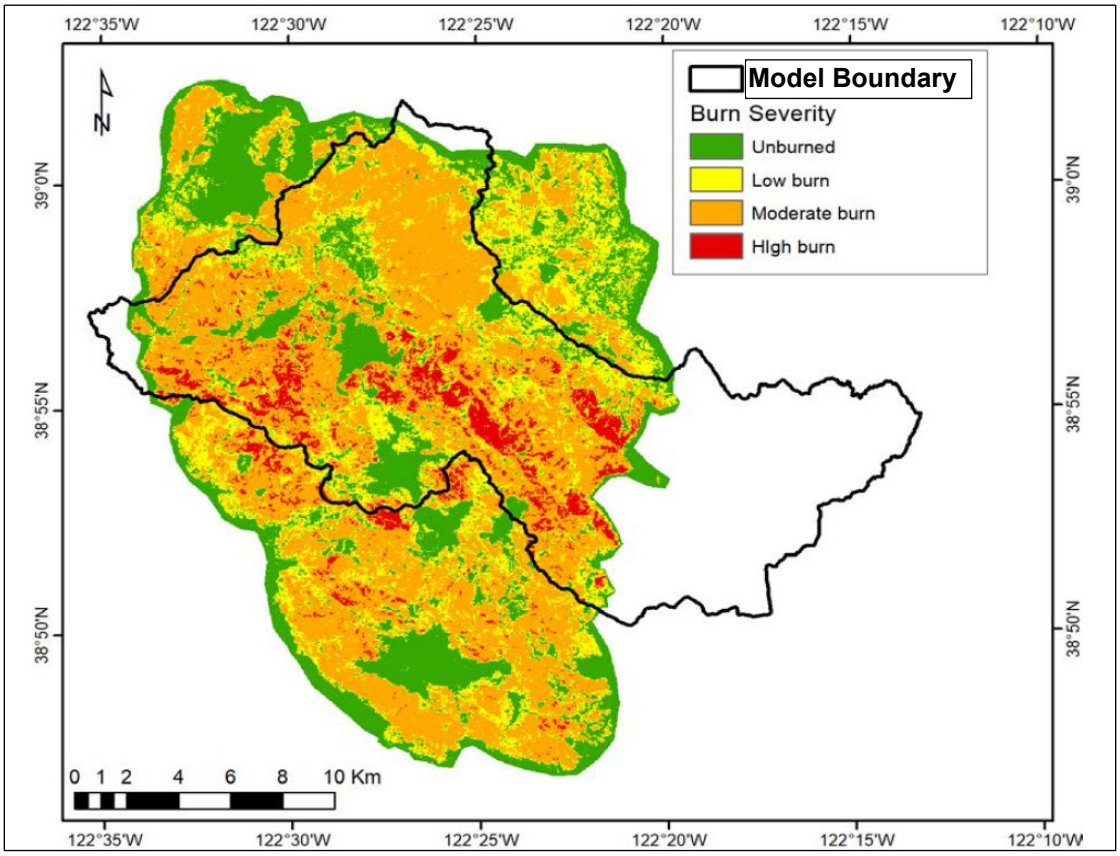

Figure 21.—Burn severity classifications for combined Rocky and Jerusalem Fires in Upper Cache Creek (Wang et al., 2019).

Table 5.—Percentages of land use in each burn severity class and vegetation classification for the total modeling area showing a significant reduction in live vegetation post-fire.

Land Cover Type	Pre-fire (%)	Post-fire (%)
Trees	30.9	13.2
Short Vegetation	65.1	38.2
Impermeable	0.2	0.9
Surface Water	0.5	0.6
Bare Earth	0.3	57.1

Table 6.—Land cover properties

Land Cover Type	Depression Storage	Canopy Coefficient
Trees	0.03	0.2
Short Vegetation	0.004	0.04
Impermeable	0.0015	0.001
Surface Water	0	0
Mixed Trees and Grass	0.012	0.088
Mixed Trees and Shrub	0.017	0.12
Bare	0.004	0

The soil cover management factor C is a key parameter used in the USLE relationship as well as SRH-W in soil erosion modeling. Wang et al. (2019) calibrated the C-value based on the recommendation of value ranges by Wischmeier and Smith (1978). Similar C values were adopted in the present study with the pre-fire C values listed in Table 7. For post-fire, soil erosion is greatly affected by wildfires through the removal of soil cover and exposure of the soil surface layer, causing a greater impact of precipitation and resultant runoff and erosion. This effect is usually taken into account through changes in C factor (Rulli et al., 2013). The post-fire C values take into consideration the burn severity, the percentage of area in each land cover type that is burned, and the duration since the fire. The C values used in the present study are listed in

.

Table 7.—Pre-fire *C* value

Land Cover Type	*C*
Trees	0.005
Short Vegetation	0.009
Mixed Trees and Grass	0.006
Mixed Trees and Shrub	0.006
Impermeable	0.000
Bare	0.010
Surface Water	0.000

Table 8.—Post-fire *C* factors

Land Cover Type	*C* (2017)
Trees	0.019
Short Vegetation	0.0131
Mixed Trees and Grass	0.0093
Mixed Trees and Shrub	0.0084
Impermeable	0.0001
Bare	0.075
Surface Water	0.000

4.1.4 Soil Properties

Hydraulic Conductivity

The soil type data for the watershed was obtained from the SSURGO database (produced and distributed by the U.S. Department of Agriculture Natural Resources). Seventy soil units are represented within the model domain. For modeling purpose, these units were grouped into eight hydraulic conductivity classes (see Figure 22). For regions with unknown hydraulic

conductivities, the closest known hydraulic conductivity was used. The same hydraulic conductivity values were adopted for both vertical and lateral directions. Overall, the pre-fire mean hydraulic conductivity was larger than 9.5 mm/hr for over 95% of the watershed.

The soil type groups used in the model was based on a combination of the hydraulic conductivity classes, the land use classes, and the burn severities. This was necessary to accommodate the impact of these properties on the effective hydraulic conductivity. As a result, a total of 14 classes were established (Figure 23). A summary of the pre-fire properties is presented Table 9. For post-fire scenarios, the pre-fire soil hydraulic conductivity values were adjusted following the approach of Wang et al. (2019) in which the hydraulic conductivity was adjusted according to the burn severity. The adjustment factor was μ, 1.2μ, and 1.4μ for high, medium, and low severity burns, respectively, where μ is a calibration parameter estimated to be 0.1 for water year 2016 and 0.2 for water year 2017.

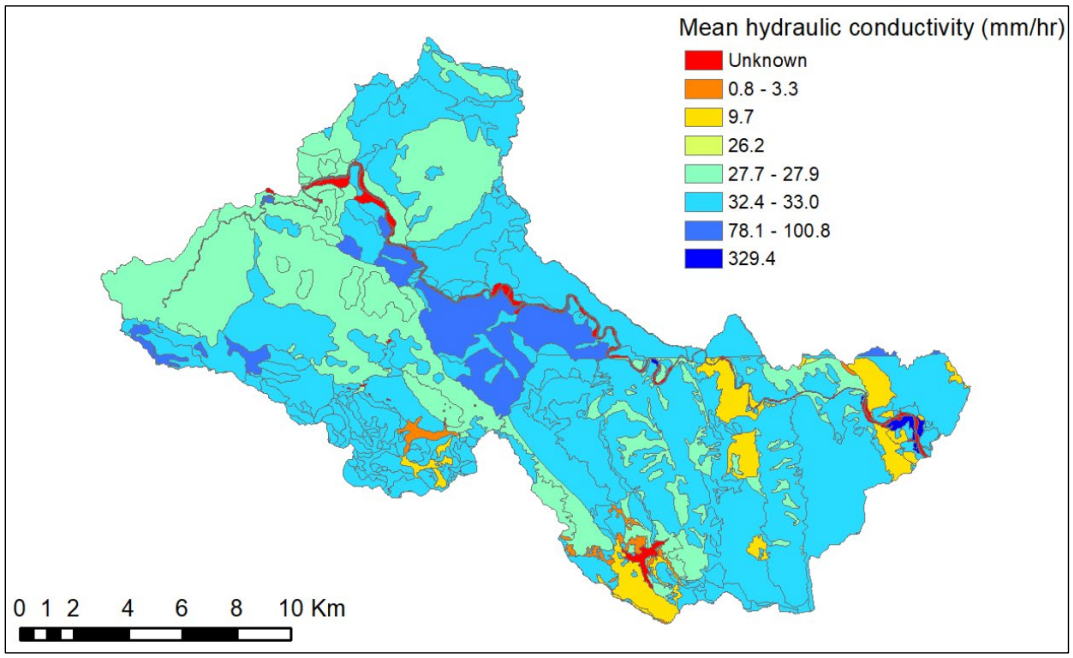

Figure 22.—Soil hydraulic conductivity ranges for soils within Upper Cache Creek sub-watershed (Wang et al., 2019).

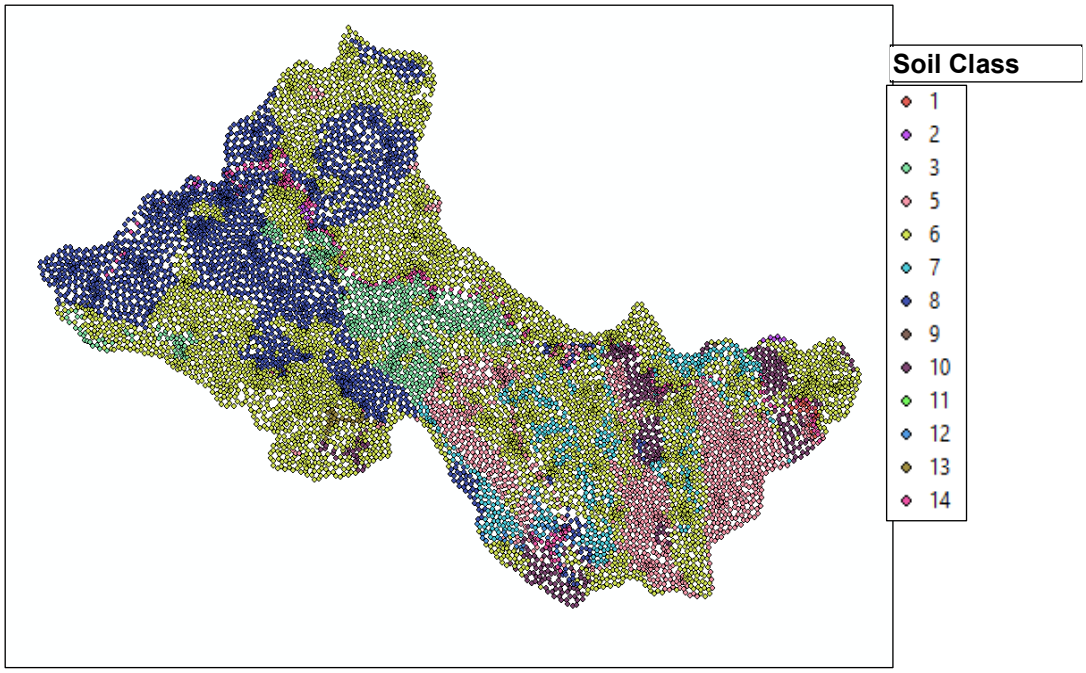

Figure 23.—Color-coded effective hydraulic conductivity classes adopted for modeling the Upper Cache Creek sub-watershed. Each dot represents the center of a mesh cell.

Table 9.—Pre-fire soil properties applied in the model for the soil classes in Figure 23

Soil Group ID	Vertical Hydraulic Cond. (m/s)	Lateral Hydraulic Cond. (m/s)	Porosity	Field Capacity	Residual Moisture	Van Genuchten Parameters	
						α	β
1	9.15E-05	9.15E-05	0.45	0.315	0.002	0.46	4.5
2	2.80E-05	2.80E-05	0.45	0.315	0.002	0.152	1.17
3	2.30E-05	2.30E-05	0.45	0.315	0.002	0.152	1.17
4	2.17E-05	2.17E-05	0.49	0.343	0.002	0.152	1.17
5	9.17E-06	9.17E-06	0.45	0.315	0.002	0.46	4.5
6	9.00E-06	9.00E-06	0.45	0.315	0.002	0.46	4.5
7	7.76E-06	7.76E-06	0.43	0.301	0.002	0.152	1.17
8	7.70E-06	7.70E-06	0.46	0.322	0.002	0.152	1.17
9	7.27E-06	7.27E-06	0.49	0.343	0.002	0.152	1.17
10	2.70E-06	2.70E-06	0.43	0.301	0.002	0.152	1.17
11	9.15E-07	9.15E-07	0.46	0.322	0.002	0.152	1.17
12	9.10E-07	9.10E-07	0.43	0.301	0.002	0.152	1.17
13	2.14E-07	2.14E-07	0.48	0.336	0.002	0.152	1.17
14	2.14E-07	2.14E-07	0.45	0.315	0.002	0.46	4.5

Soil Erodibility

The soil erodibility data was also obtained from the SSURGO database and spatial distribution is shown in Figure 24. Nine soil units are represented within the model domain, each has an erodibility estimate (i.e., *K* value in the USLE equation). For modeling purposes, the erodibility values were extracted onto the computational mesh, and then each of the 14 soil groups *in* Table 9 was assigned an erodibility value estimated as the average erodibility of all the mesh cells belonging to the group. The final pre-fire erodibility values are presented in Table 10.

Diaz-Fierros et al. (1987) noted extensive erosion in the first year of post-fire, but the effect decayed exponentially to a negligible extent after the first 12 months. Accordingly, they proposed that the soil erodibility be modified to adapt to the burned condition. This modification represents the loss in soil aggregate stability from physicochemical changes brought about by the fire. Accordingly, for Cache Creek, the erodibility in the first year post-fire (2016) was increased by 10% to the values in Table 11. This took into account the number of months post-fire before any major sediment transport occurred and the exponential decay. The erodibility values for 2017 were set to pre-fire values (Table 10).

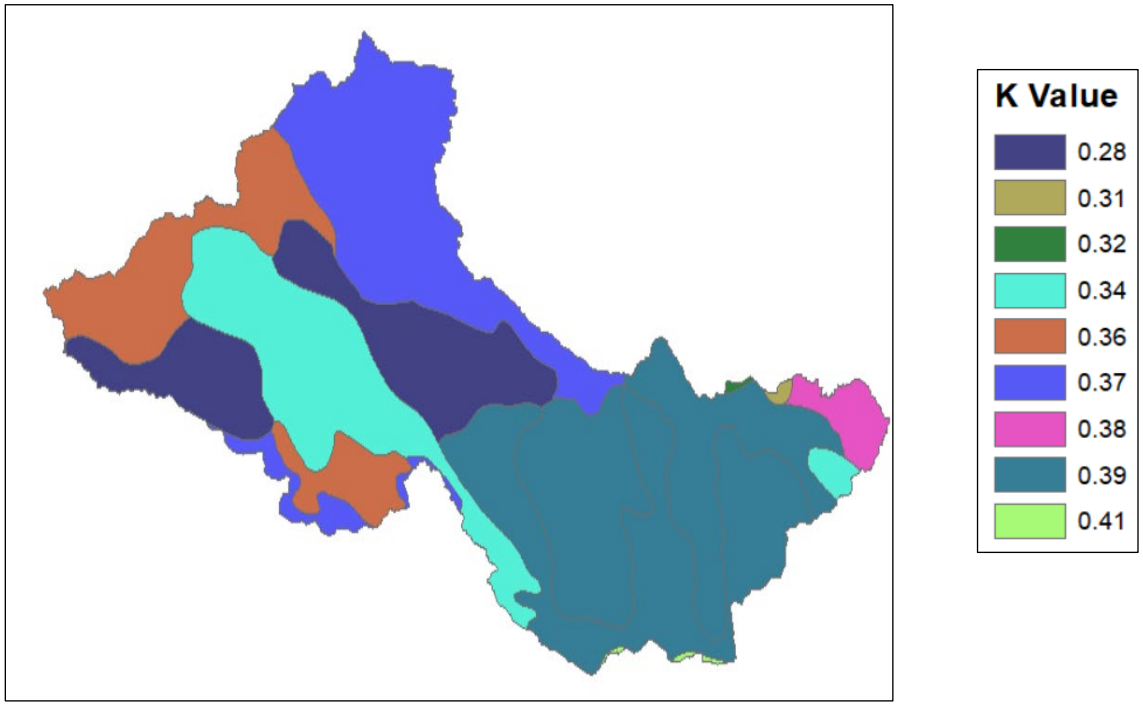

Figure 24.—Soil Erodibility (K value) distribution in Cache Creek (SSURGO).

Table 10.—Pre-fire Soil Erodibility Values

Soil Group ID	K Value (-)
1	0.35
2	0.33
3	0.29
4	0.39
5	0.39
6	0.36
7	0.38
8	0.35
9	0.32
10	0.38
11	0.31
12	0.38
13	0.36
14	0.35

Table 11.—Fire Year (2016) post-fire soil erodibility values

Soil Group ID	K Value (-)
1	0.39
2	0.36
3	0.32
4	0.43
5	0.43
6	0.40
7	0.42
8	0.39
9	0.35
10	0.42
11	0.34
12	0.42
13	0.40
14	0.39

4.1.5 Weather and Evapotranspiration Data

Hourly precipitation, potential evapotranspiration (PET) and potential evaporation (PE) time series data were also needed as model inputs. Hourly climate grids of precipitation and air temperature were based on eleven local climate stations to reflect the spatial heterogeneity. The resulting precipitation time series data are plotted in Figure 25a and Figure 26a for water years (WY) WY2015 and WY2017, respectively.

Wang et al. (2019) used the resulting air temperature grid with the Priestly-Taylor PET relationship to derive the hourly PET time series for the model domain (Figure 25b and Figure 26b). For short vegetation, the Priestly-Taylor relationship was used to estimate the hourly PE time series (Figure 25c and Figure 26c), assuming a vegetation height of 2 m. For trees, the Penman-Monteith equation was used to estimate the hourly PE time series (Figure 25d and Figure 26d) and verified using the Holmes equation and local hourly wind data.

Leaf area index (LAI) time series and root depths were also generated for trees and short vegetation (Figure 27). The LAI values were derived from Moderate Resolution Imaging Spectroradiometer (MODIS) remotely sensed data, while leaf on and off dates were developed using eMODIS Normalized Density Vegetation Index grids (Swets et al. 1999; Jenkerson 2010; https://phenology.cr.usgs.gov). The time series for land cover types comprising mixed trees and short vegetation were derived from those for trees and short vegetation through simple weighting based on the proportion of trees and short vegetation present. These are also shown on (Figure 27). The mean root depths corresponding to the different land cover types (Table 12) was estimated from a plant rooting depth database obtained from the Nature Conservancy program (https://groundwaterresourcehub.org/sgma-tools/gde-rooting-depths-database-for-gdes/).

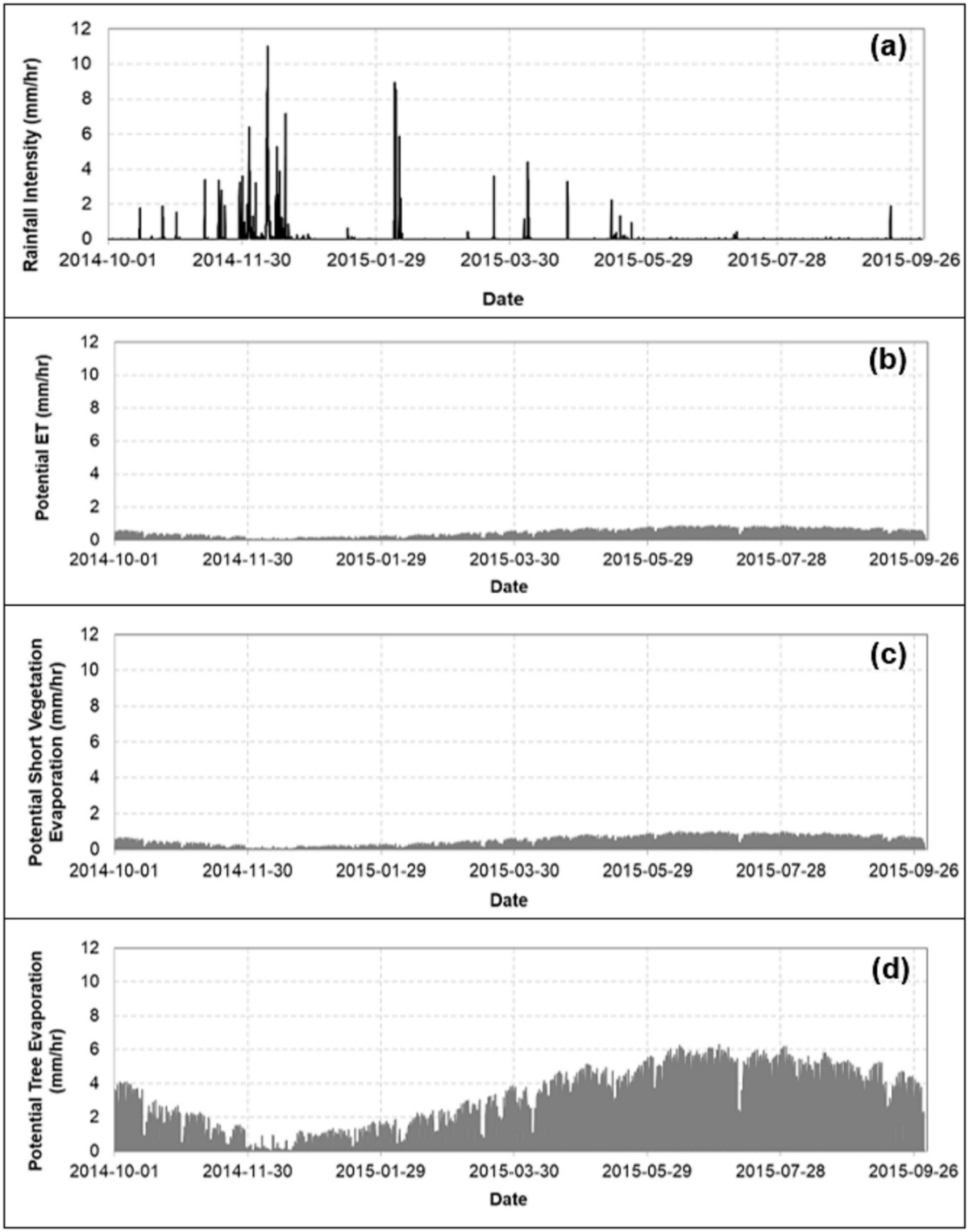

Figure 25.—WY2015 forcing time series in model domain; (a) precipitation intensity for domain, (b) potential evapotranspiration for domain, (c) potential evaporation for short vegetation only, and (d) potential evaporation for trees only.

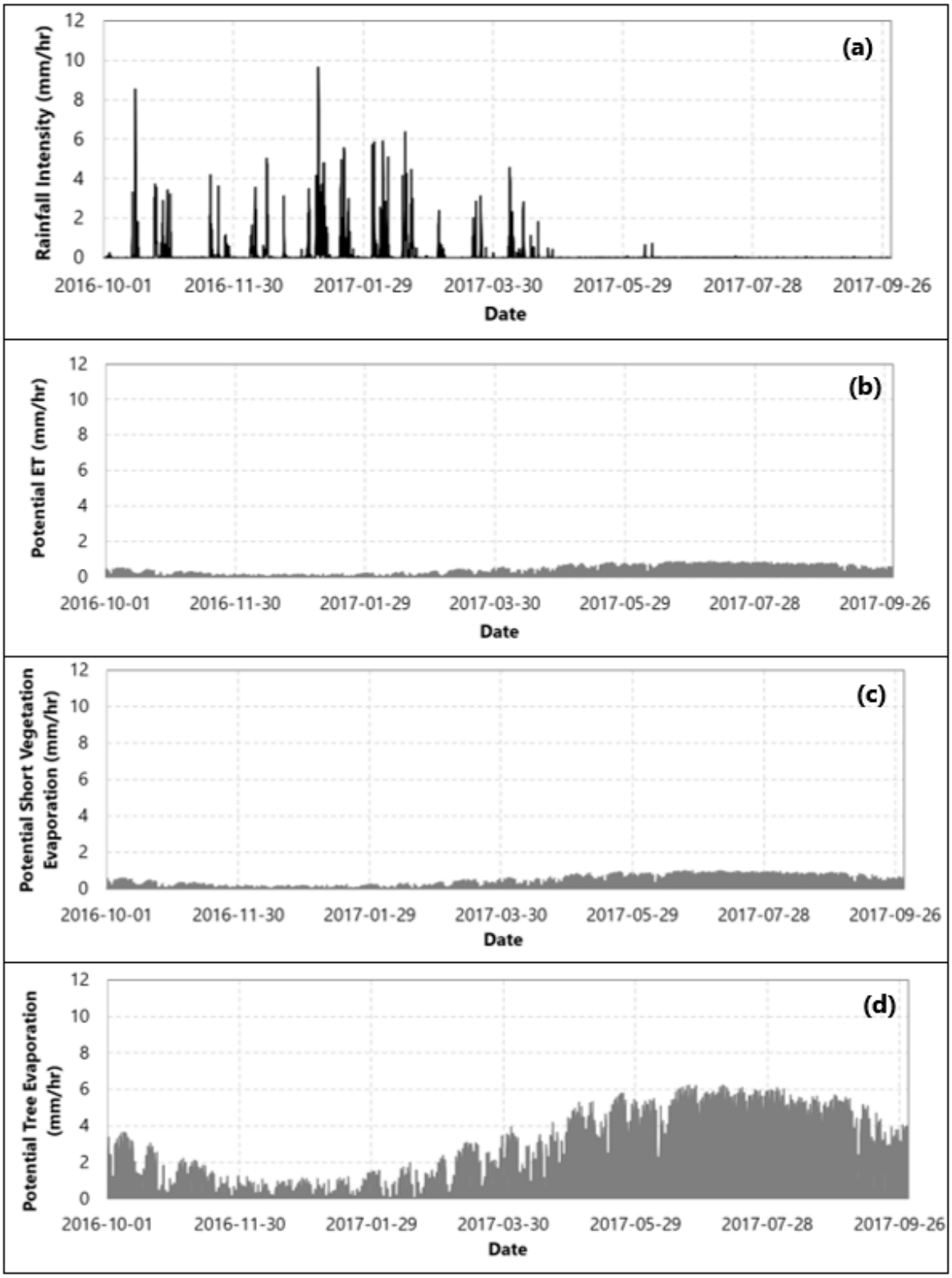

Figure 26.—WY2017 forcing time series in model domain; (a) precipitation intensity for domain, (b) potential evapotranspiration for domain, (c) potential evaporation for short vegetation only, and (d) potential evaporation for trees only.

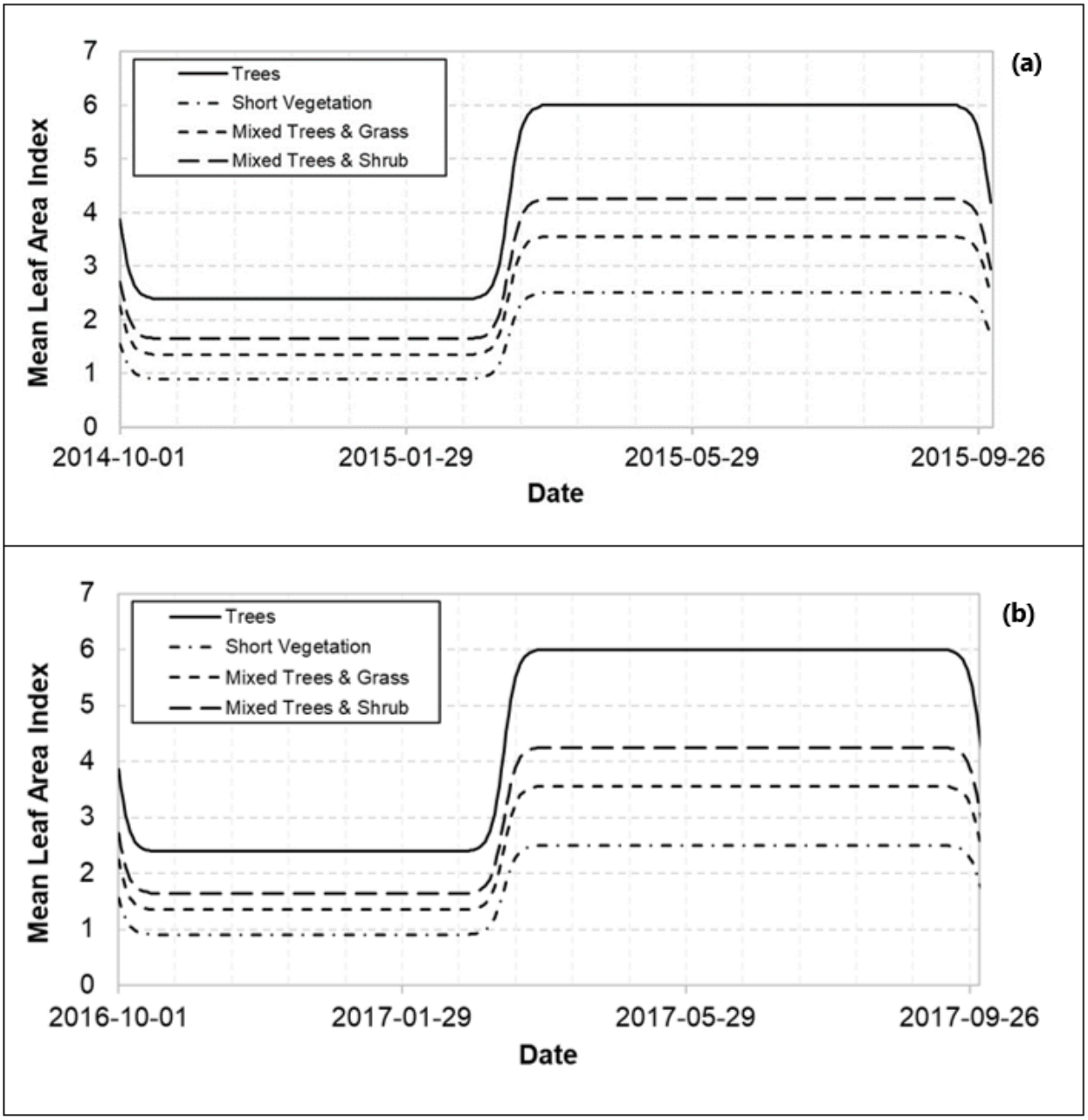

Figure 27.—Leaf Area Index times series for vegetation in the model domain (a) WY2015, and (b) WY2017.

Table 12.—Estimated root depth for Cache Creek Watershed

Land Cover Type	Root Depth (m)
Trees	3.5
Short Vegetation	1.5
Mixed Trees and Grass	2.1
Mixed Trees and Shrub	2.5

4.1.6 Runoff and Sediment Results

The SRH-W predicted water runoff at the watershed outlet is presented in Figure 28 and Figure 29 for the pre- and post-fire scenarios respectively. Overall, SRH-W performs well for both pre- and post-fire scenarios; the Nash-Sutcliffe efficiency coefficient is 0.80 and 0.81, respectively, for pre-fire water years 2000 and 2015, and 0.79 and 0.87 for post-fire water years 2016 and 2017, respectively. The timing and magnitudes of the predicted flow peaks generally correspond well with the observed values. Predicted low flows are also generally in good correspondence with the observed low flows over the simulated time periods (with some over- and under-prediction). The largest deviations in low flows occurred during the falling limbs of events, where the model results tend to underpredict the discharge rates. The cause of this underprediction is traced to the North Fork inlet boundary condition that was obtained from the HSPF model. The HSPF model predicted negligible baseflow contributions at the North Fork inlet boundary location, which is unlikely given the size of the watershed contributing to that location. Hence, the lower model discharges.

The predicted sediment loads at the watershed outlet are presented in Figure 30 and Figure 31 for the pre- and post-fire scenarios. SRH-W is able to predict the observed trends and performs well overall for both pre- and post-fire scenarios. The Nash-Sutcliffe efficiency coefficient is 0.91 for pre-fire water year 2015, and 0.67 and 0.83 for post-fire water years 2016 and 2017, respectively. The timing and magnitudes of sediment load peaks were predicted well. An interesting trend is observed in which the sediment fluxes in the year immediately after the fires were much lower in magnitude than the previous pre-fire year. This can be explained as that there was considerably less rainfall. This highlights the importance of being able to forecast and predict fire impact using the future projected rainfall, without always assuming that the net flux would increase following the fire. It is worth pointing out that the sediment fluxes are reported on a daily time step, hence the relatively higher NSEC values compared to flow discharge, which is reported on an hourly time step.

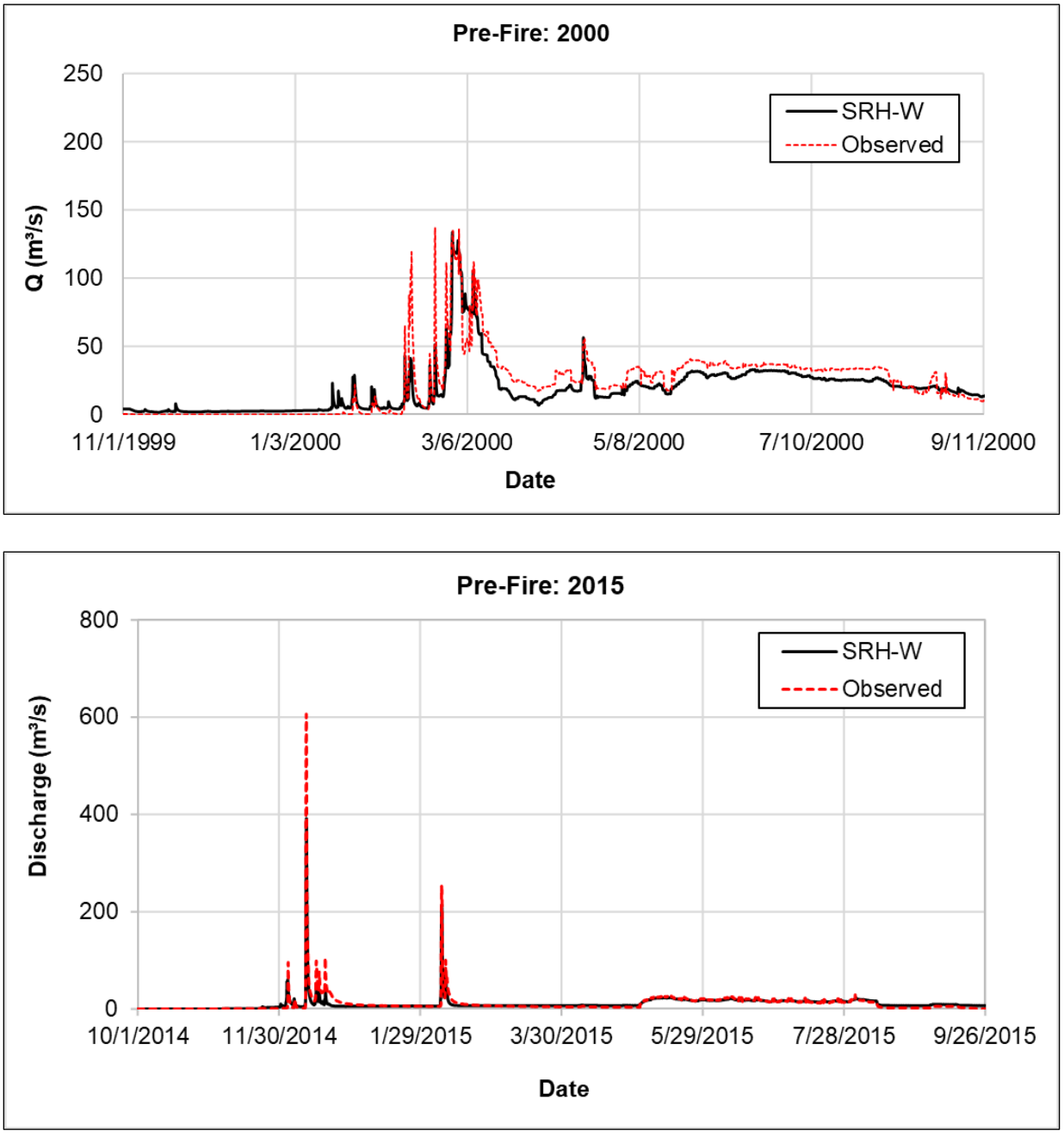

Figure 28.—Comparison between observed flow discharge and SRH-W predicted flow discharge at the watershed outlet for pre-fire water years 2000 and 2015.

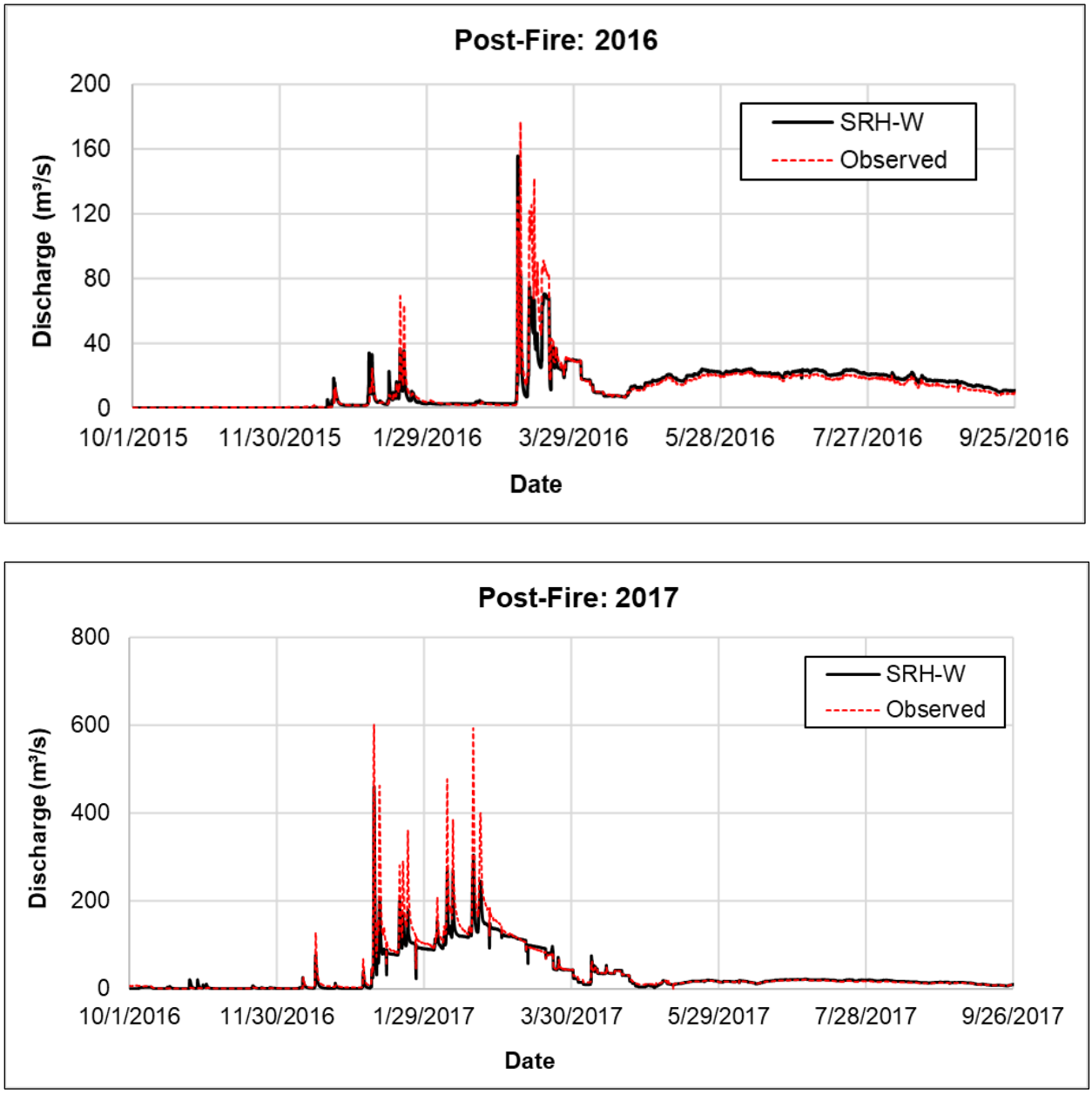

Figure 29.—Comparison between observed flow discharge and SRH-W predicted flow discharge at the watershed outlet for post-fire water years 2016 and 2017.

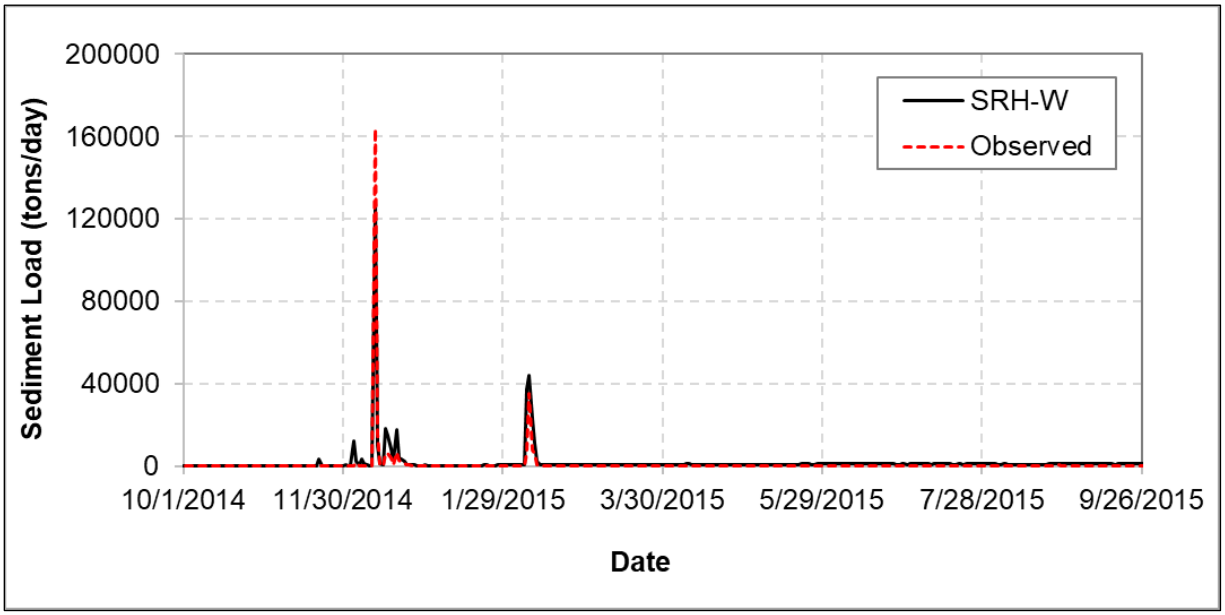

Figure 30.—Comparison between observed sediment load and SRH-W predicted sediment load at the watershed outlet for pre-fire water year 2015.

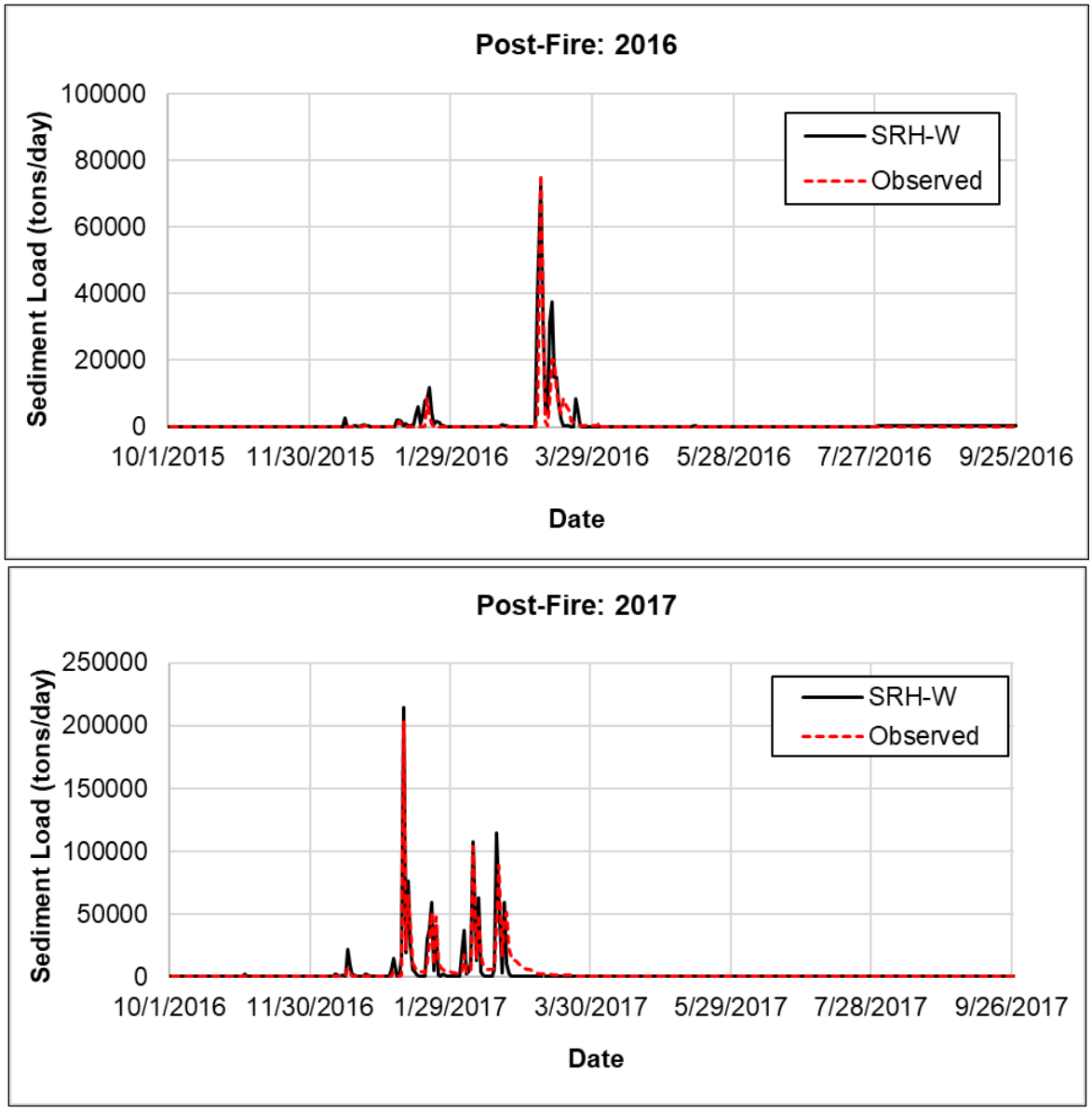

Figure 31.—Comparison between observed sediment load and SRH-W predicted sediment load at the watershed outlet for post-fire water years 2016 and 2017.

4.2 Mercury Simulation Results

This section focuses on the mercury simulation result in the Cache Creek Watershed, CA. In specific, water years 2015 (October 2014 to September 2015) and 2017 (October 2016 to September 2017) are simulated. These periods respectively correspond to pre- and post-fire conditions (following the Rocky and Jerusalem fires) in the watershed. Characterization of the watershed, model inputs, and model results relevant to the water runoff and sediment have been presented in the previous section and not repeated. Only those relevant to the mercury simulation are presented and discussed.

4.2.1 Modeling setup and inputs

The 2D mesh used for the mercury simulations is the same as described in Figure 19 - a 2D hybrid mesh. Following Wang et al. (2019), the USGS' national geochemical database (Smith et al., 2013) is used to estimate an average pre-fire total soil-mercury concentration of 0.175µg/g for upland soils in the watershed for WY2015. For WY2017, Wang et al. (2019) used a soil-heating model to estimate the depth of soil heating and resultant post-fire soil concentration. The loss estimation was based on the temperature beyond which ligands that bind mercury to organic matter are destroyed. Post-fire mercury concentrations with depth are estimated based on the burn severity. Table 13 below presents the post-fire mercury distribution used in the model (corresponding to the post-fire burn areas shown in Figure 21). For the simulations, it is assumed that atmospheric mercury inputs are negligible compared to sediment related mercury inputs – this is consistent with observed patterns in Cache Creek and the model that has been developed.

For methylmercury simulations, our predictions are based on observed ratios between methylmercury and total mercury in Cache Creek for WY2015 and WY2017. This approach is simple and necessitated by the little methylmercury information available in Cache Creek. Using data from field samples of water and suspend sediment, Wang et al. (2019) recommend the ratios in Table 14 for estimating methylmercury loads in Cache Creek.

Further model calibration, including the Manning's roughness, was performed for the mercury simulations to better capture the runoff associated with the different spatial distributions of land cover and burn intensities, and associated mobilization of mercury. The resultant calibration values for Manning's *n*, the most sensitive parameter, are presented in Table 15.

Table 13.—Mercury concentration for the four burn severity categories in Cache Creek

Soil erosion depth (cm)	Mercury concentration (µg/kg)			
	High burn	Moderate burn	Low burn	No burn
0.5	35.6	45.7	114.8	175
1.0	79.8	101.1	144.9	175
1.5	112.5	126.1	153.4	175
2.0	129.0	138.1	160.6	175
2.5	137.7	145.4	163.0	175
3.0	143.9	149.9	165.4	175

Table 14.—Methylmercury to total mercury ratios in Cache Creek for WY2015 and WY2017

Water Year	Ratio of Methylmercury to Total Mercury
2015 (pre-fire)	0.002
2017 (post-fire)	0.0033

Table 15.—Calibrated Manning's roughness values for mercury simulations

Land Cover Type	Manning's Roughness
Trees	0.1
Short Vegetation	0.06
Impermeable	0.02
Surface Water	0.02
Mixed Trees and Grass	0.08
Mixed Trees and Shrub	0.08
Bare	0.03

4.2.2 Mercury Results and Discussion

Figure 32 compares the predicted total mercury loads with the observed data for storm events in WY2015 and WY2017. Overall, the model predicted the observed fluxes reasonably well. The NSEC values for the total mercury fluxes were 0.87 and 0.33 respectively for WY2015 and WY2017. Like the sediment flux, the total mercury flux is reported on a daily time step. While, the model performed well for WY2015, it is judged only to be fair for WY2017. The peak magnitude and timing were captured well for WY2015. However, while the timings of the peaks were captured for WY2017, the trend and magnitude of the peaks were not. The observed data showed increasing mercury concentrations with subsequent storms, which was not captured by the model.

The predicted trend in total mercury flux mimicked the trend in sediment flux for the most part. This is expected since the model assumes that total mercury is directly associated with sediment. The observed increase in mercury concentration with subsequent storms in WY2017, which was not captured by the model, is likely due to mercury sources not accounted for in the current

model. Post-fire mercury concentrations in upland soils are low at the surface and increase with soil depth (Table 13). Consequently, one would expect mercury concentrations in eroded soils to increase in time and the number of events following a fire, due to erosion of material deeper within the soil column. To accurately capture this, a detailed representation of micro-channel and gully formation/growth and erosion on the landscape is needed. This would correctly capture the erosion depth and mercury concentration of contributing soils. At present, the Cache Creek model was set up to compute the average erosion rate over the scale of the hillslope and thus material contributions are primarily from the surface. This suggests that contributions would be relatively low in mercury concentration over a longer period of time. A potential way to address this would be to determine an "effective" erosion depth based on expected micro-channel dimensions on hillslopes to estimate more accurate mercury concentrations in eroded soil.

To further check our model's total mercury predictive performance, we compare the WY2017 predictions in this study with the prediction by Wang et al. (2019) using PFHydro-WQ, under a similar set of assumptions. This is shown in . It is seen that there is good correspondence between the two model results, with the NSEC of 0.67. This is expected given the similar inputs and assumptions used in both studies; it also verifies that the model is predicting what it is supposed to, given its constraints.

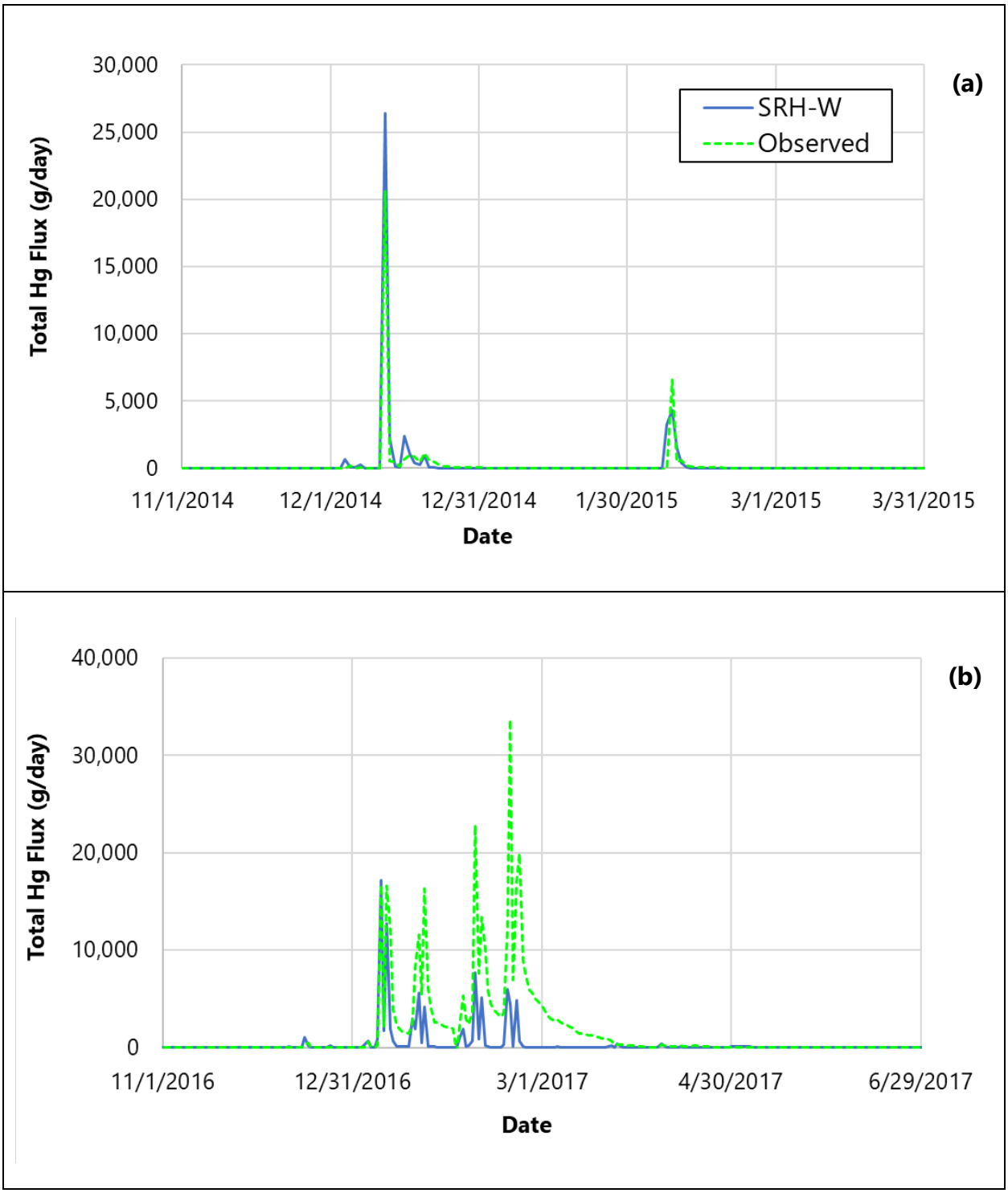

Figure 32.—Comparison between predicted and observed Total Mercury fluxes (in g/day) at Cache Creek watershed outlet for (a) WY2015 and (b) WY2017.

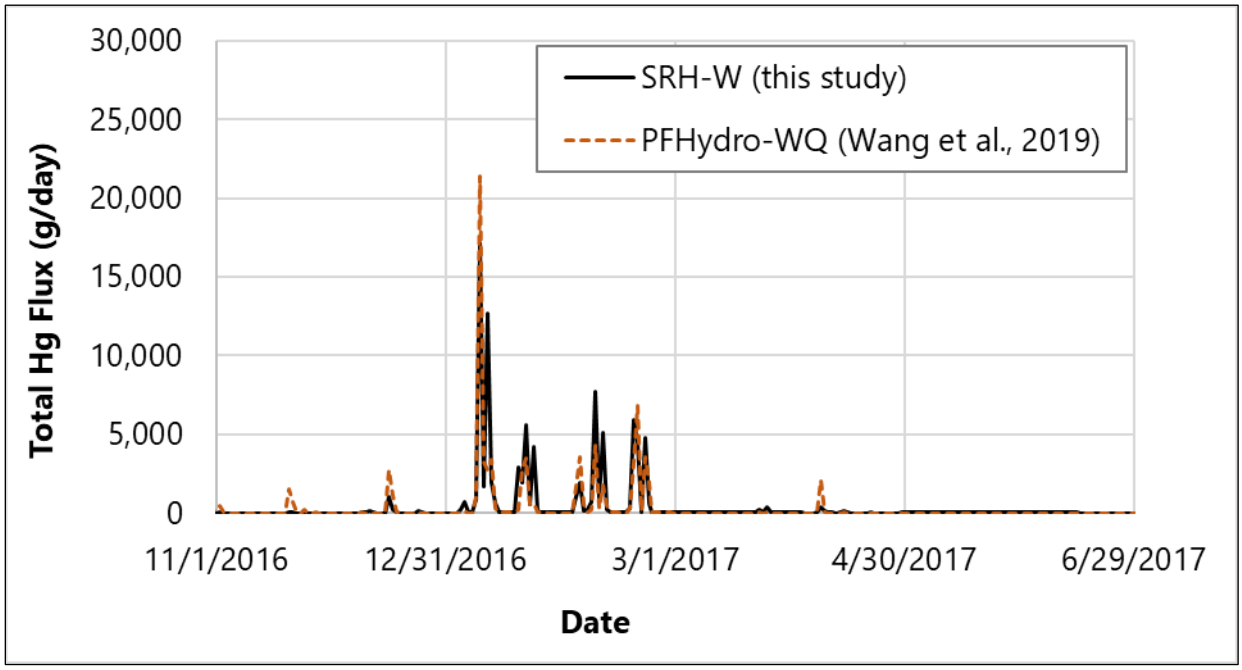

Figure 33.—Comparison between SRH-W and PFHydro-WQ total mercury flux predictions for WY2017 at Cache Creek outlet.

Figure 34 compares the predicted methylmercury loads with the observed data for storm events in WY2015 and WY2017. The methylmercury flux is also reported on a daily time step. As expected, the trends were similar to both the sediment and total mercury trends given the approach adopted. While, the model performed well for WY2015, its performance for WY2017 was only fair. The peak magnitude and timing were captured well for WY2015. However, only the timings of the peaks were well predicted for WY2017. The trend and magnitudes of the peaks were not. The observed data showed increasing methylmercury concentrations with subsequent storms, which was not captured by the model.

A final assessment of modeling results and performance is done comparing fluxes from two similar storm events in WY2015 (12/10/14 – 12/13/14; pre-fire) and WY2017 (01/06/17 – 01/09/17; post-fire). These are the biggest events in the respective years and have similar precipitation amounts and intensities. The assessment serves to evaluate the model performance in capturing pre- and post-fire effects on sediment and mercury loads. Table 16 summarizes both observed and modeled net sediment and mercury loads for the two storm events. As shown, the precipitation amounts are similar, with the total precipitation for WY2017 approximately 1.1 times the WY2015 precipitation. However, both model predictions and observed data suggest a marked increase in sediment loads between pre- and post-fire conditions by 1.39 and 1.20, respectively, highlighting the effects of fire on erosion rates and sediment loading. The ratios of modeled and observed total mercury loads (i.e., post-fire/pre-fire load) are also as expected, with respective values of 0.70 and 0.86, which are consistent with the reduction in terrestrial mercury concentrations following soil heating by wildfire. Unlike total mercury loads, the modeled and observed methylmercury loads are larger post-fire compared to pre-fire loads, with ratios of

1.12 and 1.37, respectively. The relatively larger post-fire methylmercury loads could be due to a stimulation in methylmercury formation with the addition of sulfate and labile carbon to the soil during the burning process (Krabbenhoft and Fink, 2001) as well as the hypothesized post-fire increase in methylmercury adsorption rates that is brought about by thermal changes to carbon-bearing particles and formation of sorption-active surfaces (Wang et al., 2019). Overall, the results show that the developed model can predict observed trends in pre- and post-fire sediment and mercury fluxes and, thus, can be a good tool for evaluating wildfire effects for various purposes.

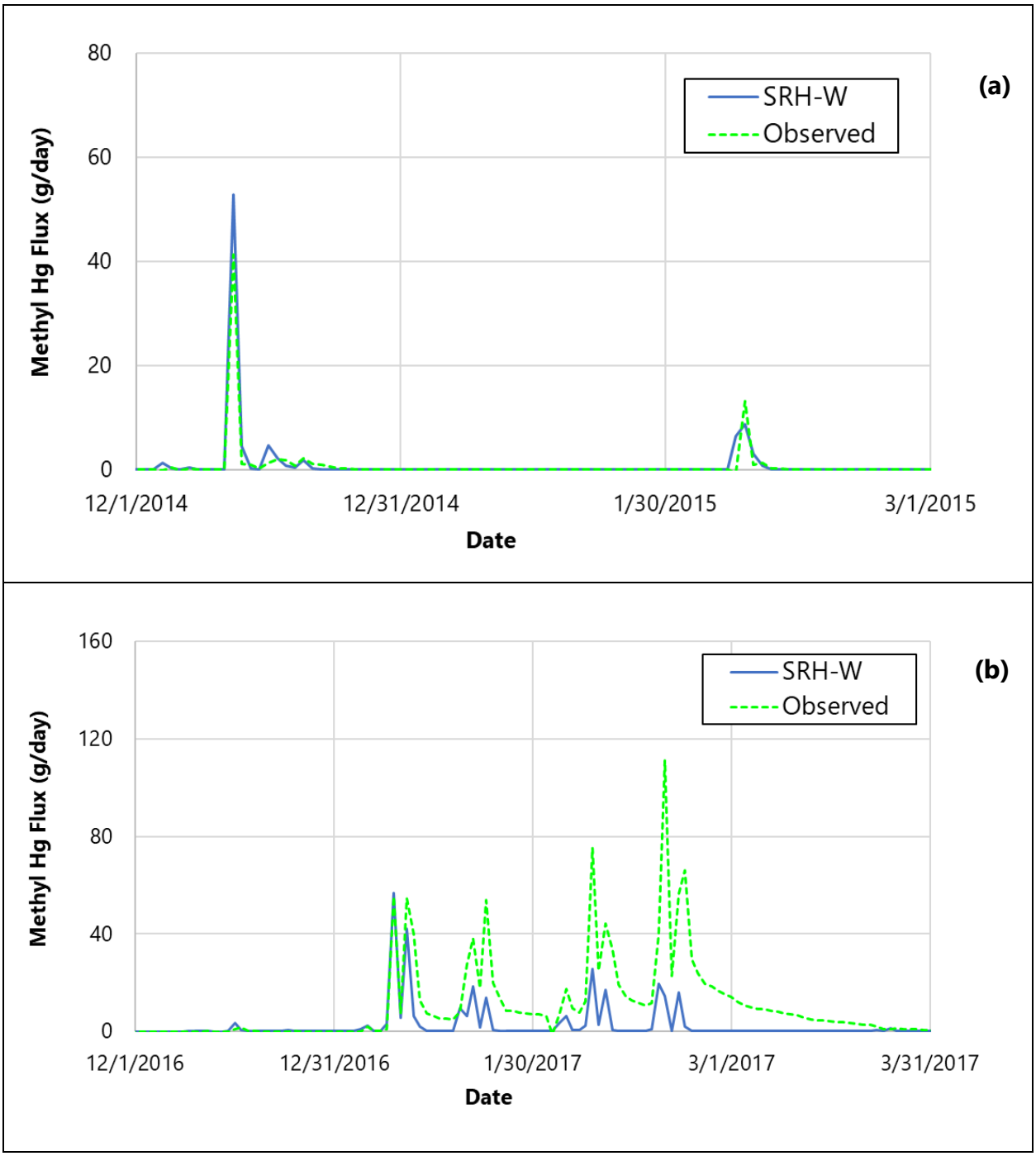

Figure 34.—Comparison between predicted and observed Methyl Mercury fluxes (in g/day) at Cache Creek watershed outlet for (a) WY2015 and (b) WY2017.

Table 16.—Comparison of sediment and mercury loads for pre-fire and post-fire storm events

Precipitation Start and End Time	Total precipitation (mm)	Total simulated sediment load (tons)	Total observed sediment load (tons)	Total simulated Hg load (kg)	Total observed Hg load (kg)	Total simulated MeHg load (g)	Total observed MeHg load (g)
12/10/14-12/13/14 (pre-fire)	127	164,519	179,214	29	21	58	43
01/06/17–01/09/17 (post-fire)	141	228,952	215,093	20	18	65	59
post-fire/pre-fire	1.11	1.39	1.20	0.70	0.86	1.12	1.37

There are several potential reasons for differences between the observed and predicted mercury flux values, besides those already mentioned in preceding paragraphs. While the spatial heterogeneity has been captured, our analyses are limited by the uncertainty contained in the available input data. For example, uncertainty can be high in the depth-to-bedrock distribution across the watershed, as well as the spatial coverage of rainfall across the watershed. There is also uncertainty in the hydraulic conductivities, erodibility and soil mercury values obtained from national geodatabases, as these are average representative values that have some distribution to them. These uncertainties highlight general modeling limitations; the benefits of having a flexible, distributed mesh capable of capturing input datasets with different resolutions should be noted within the context of the information contained in the datasets.

5. Concluding Remarks

A new process-based, mesh-distributed watershed model, SRH-W, has been developed, which is applicable to both event-based and continuous modeling that spans a sequence of events. Intended modeling applications of SRH-W include: (a) flood forecast and water routing for a given precipitation event or sequence of precipitation events; (b) sediment and mercury delivery to a project site from a watershed; (c) identification of sediment and mercury sources and locations within a watershed with highest erosion potential; and (d) project and management practice impact assessment at local and watershed scales.

The overland domain is represented by 2D mesh cells that may assume any resolution and shape, and the channel network may be represented by the same overland 2D mesh or by a separate 1D network. Overland runoff is based on the 2D diffusive wave solver and the sediment and mercury transport are governed by the non-equilibrium mass conservation equation, while the channel network is solved by the 1D diffusive wave.

Key improvements and advancements include: (a) applicability of the model to both small and large watersheds; (b) use of a meshing technology allowing both coarse and refined resolution simulations; (c) finite-volume discretization with both explicit and implicit schemes; (d) seamless coupling of major hydrological processes on overland, stream network, floodplain and groundwater; (e) robustness, accuracy, and ease of application, and most important, (f) the ability to simulate mercury transport.

The model validation and application are reported to simulate the runoff, sediment transport and mercury transport in the Cache Creek watershed, California, with special focus on the pre- and post-fire impact of the burn severity. The results demonstrated the flexibility and utility of the SRH-W; it has also been shown that the model is capable of reproducing the field observed runoff, sediment transport and mercury movement rates within the uncertainty of the input data.

References

Alonso, C. V., Bingner, R. L., and Kuhnle, R. A. (1995). "Sediment Yield From Watersheds With Eroding Channels." Water Resources Engineering : Proceedings of the First International Conference, Am. Soc. of Civil Eng., 1183-1187.

Alonso, C. V. (1996). "Hydrologic Research on the USDA Goodwin Creek Experimental Watershed, Northern Mississippi." Procs. 16th AGU Hydrology Days, Colorado State University, 25-36.

Alpers, C.N., Marvin-DiPasquale, M., Ackerman, J.A., Fleck, J.A., Windham-Myers, L, Fuller, C.C., Arias, M., Agee, J., Hartman, C.A., Herzog., M.P., & Eagles-Smith, C.A., in revision, Mercury studies in the Cache Creek Settling Basin, Yolo County California, Preliminary Results, 2010-14: USGS Scientific Investigations Report.

Bennett, J. P. (1974). Concepts of mathematical modeling of sediment yield. Water Resources Research, 10, 485–492.

Benoit, J. M., Gilmour, C. C., Heyes, A., Mason, R. P., Miller, C. L., 2003. Geochemical and biological controls over methylmercury production and degradation in aquatic ecosystems. In Cai, Y., Olin, B. C., (eds.) Biogeochemistry of important trace elements. ACS Symposium Series 835, 262-297.

Blackmarr, W. A. (1995). "Documentation of Hydrologic, Geomorphic, and Sediment transport Measurements on the Goodwin Creek Experimental Watershed, Northern Mississippi, for the Period 1982-1993 - Preliminary Release." Research Report No.3 (CD-ROM), U.S, Dept. of Agriculture. Agricultural Research Service.

Bras, R.L. (1990). Hydrology, an introduction to hydrologic science. Addison -Wesley.

Brooks, K.N., Ffolliott, P.F. and Magner, J.A. (2013). Hydrology and the Management of Watersheds. John Wiley & Sons, Inc., New York.

Caldwell, C.A., Canavan, C.M., and Bloom, N.S., 2000, Potential effects of forest fire and storm flow on total mercury and methylmercury in sediments of an arid-lands reservoir: Science of the Total Environment, 260(1-3), 125-133.

Carroll, R.W.H., Warwick, J.J., Heim, K.J., Bonzongo, J.C., Miller, J.R., and Lyons, W.B. (2000). Simulation of mercury transport and fate in the Carson River, Nevada, Ecological Modelling, vol.125, pp. 255 –278.

Chen, C.W., Herr, J., and Ziemelis, L. (1998). Watershed analysis risk management framework: A decision support system for watershed approach and total maximum daily load calculation. Topical report (No. EPRI-TR--110709). Electric Power Research Inst., Palo Alto, CA (United States); Systech Engineering, San Ramon, CA (United States).

Chow, V.T., Maidment, D.R. and Mays L.W. (1988). Applied Hydrology. New York: McGraw-Hill.

Dai, T., Ambrose, R.B., Alvi, K., Wool, T., Manguerra, H., Chokshi, M., Yang, H., and Kraemer, S. (2005). Characterizing Spatial and Temporal Dynamics: Development of a Grid-Based Watershed Mercury Loading Model, in Managing Watersheds for Human and Natural Impacts, pp. 1–12, American Society of Civil Engineers, Reston, VA.

Davis, G., Knightes, C.D., Abdelnour, A., Stieglitz, M. (2011). Biogeochemical Cycling of Mercury in Watersheds: VELMA (Visualizing Ecosystems for Land Management Assessment), International Conference on Mercury as a Global Pollutant, Halifax, Nova Scotia.

Diaz-Fierros, F., Benito Rueda, V.E., Perez Moreira, R. (1987). Evaluation of the U.S.L.E. for the prediction of erosion in burnt forest areas in Galicia (N.W. Spain), CATENA, Vol.14 (Issues 1–3),189-199.

Domagalski, J.D., Majewski, M.S., Alpers, C.N., Eckley, C.S., Eagles-Smith, C.A., Schenk, L., and Wherry, S., 2016, Comparison of mercury mass loading in streams to atmospheric deposition in watersheds in the western U.S.: Evidence for non-atmospheric mercury sources: Science of the Total Environment, 568, 638–650.

Downer, C.W., Ogden, F.L., Martin, W.D. and Harmon, R.S. (2002). Theory, development, and application of the surface water hydrologic model CASC2D. Hydrological Processes, 16, 255-275.

Downer, C.W. and Ogden, F.L. (2006). Gridded Surface Subsurface Hydrologic Analysis (GSSHA) User's manual. ERDC/CHL SR-06-1.

Dunne, T. and Leopold, L.B. (1978). Water in environmental planning. W. H. Freemont Company, San Francisco, California.

EPRI (2009). Dynamic Mercury Cycling Model for Windows XP/Vista – A Model for Mercury Cycling in Lakes. D-MCM Version 3.0. User's Guide and Technical Reference.

Gilley, J.E., Woolhiser, D.A., and McWhorter, D.B. (1985). Interrill Soil Erosion – Part I: Development of Model Equations, Transactions of the ASAE, 28(1), 147-153.

Golden, H.E., Knightes, C.D., Conrads, C.D., Davis, G.M., Feaster, T.D., Journey, C.A., Benedict, S.T., Brigham, M.A., and Bradley, P.M. (2012). Characterizing mercury concentrations and fluxes in a coastal plain watershed: Insights from dynamic modeling and data. Journal of Geophysical Research: Biogeosciences: 117, doi:10.1029/2011JG001806.

Govers, G. (1992). Evaluation of transporting capacity formulae for overland flow. Overland Flow, Parsons, J. and Abrahams, A. D. (eds), 243-274.

Guy, B.T., Rudra, R.P., Dickenson, W.T. and Sohrabi, T.M. (2009). Empirical model for calculating sediment-transport capacity in shallow overland flow: model development. Biosystem Engineering, 103, 105–115.

Haan, C.T., Barfield, B.J., and Hayes, J.C. (1994). Design Hydrology and Sedimentology for Small Catchments. Academic Press Inc, Elsevier. San Diego, California.

Holloway, J.M., Goldhaber, M.B., Scow, K.M., and Drenovsky, R.E., 2009b, Spatial and seasonal variations in mercury methylation and microbial community structure in a historic mercury mining area, Yolo County, California: Chemical Geology, 267, 85-95.

Horton, R.E. (1933). The role of infiltration in the hydrologic cycle. American Geophysical Union Transactions, 14, 446-460.Howard, C. (1996). Revisiting the degree-day method for snowmelt computations – Discussion. Water Resources Bull., 32, 411–413.

Jenkerson, C. B., Maiersperger, T.K., Schmidt, G. L. (2010). eMODIS - a user-friendly data source. U.S. Geological Survey (USGS) Open-File Report, Reston, VA, USA. 2010-1055

Johnson, B.E., Julien, P.Y., Molnar, D.K. and Watson, C.C. (2000). The two-dimensional upland erosion model CASC2D-SED. Journal of The American Water Resources Association, 36(1), 31-42.

Julien, P.Y. and Saghafian, B. (1991). CASC2D User's Manual - A Two Dimensional Watershed Rainfall-Runoff Model. Department of Civil Engineering, Colorado State University, Fort Collins, Colorado. Report CER90-91PYJ-BS-12, pp.66.

Julien, P.Y. (1998). Erosion and Sedimentation (First Paperback Edition). Cambridge University Press, Cambridge, UK, pp.280.

Julien, P.Y. (2002). River Mechanics. Cambridge University Press, Cambridge, UK, pp.434.

Kelly, E.N., Schindler, D.W., St Louis, V.L., Donald, D.B., Vladicka, K.E. (2006). Forest fire increases mercury accumulation by fishes via food web restructuring and increased mercury inputs. Proceedings of the National Academy of Sciences of the United States of America 103: 19380–5.

Kilinc, M.Y. and Richardson, E.V. (1973). Mechanics of soil erosion from overland flow generated by simulated rainfall. Hydrology Papers Number 63. Colorado State University, Fort Collins, Colorado.

Knightes, C. and Ambrose Jr., R.B. (2004). Analysis of mercury in Vermont and New Hampshire lakes: Evaluation of the regional mercury cycling model. U.S. Environmental Protection Agency, Washington, DC, EPA/600/R-04/080 (NTIS PB2005-101438).

Krabbenhoft, D.P., and Fink, L.E., 2001, Appendix 7-8: The effects of dry down and natural fires on mercury methylation in the Florida Everglades. Everglades Consolidated Report. South Florida Water Management District. A7-8-1 to A7-8-14.

Kuhnle, R. A., Bingner, R. L., Foster, G. R., and Grissinger, E. H. (1996). "Effect of land use changes on sediment transport in Goodwin Creek." Water Resources Research, 32(10), 3189-3196.

Kuhnle, R. A. and Willis, J. C. (1998). "Statistics of Sediment Transport in Goodwin Creek." ASCE J. Hydraulic Engineering, 124(11), 1109-1114.

Lai, Y.G. (2008). SRH-2D version 2: Theory and User's Manual. Technical Service Center, U.S. Bureau of Reclamation, Denver, Colorado.

Lai, Y.G. (2010). Two-Dimensional Depth-Averaged Flow Modeling with an Unstructured Hybrid Mesh. J. Hydraulic Engineering, 136(1), 12-23.

Lai, Y.G. (2017). SRH-WQ: A Water Quality and Mercury Transport Model for Streams and Reservoirs. Technical Service Center, Bureau of Reclamation, Denver, CO.

Lai, Y.G., and Greimenn, B. (2019). Development of a Physically-Based Distributed Watershed Scale Model. Federal Interagency Hydrologic Modeling Conference, June 24-28, 2019, Reno, NV.

Lai, Y.G., Abban, B., and Politano, M. (2020). Development of a Distributed Watershed Model and its Application to Clear Creek, Iowa. Watershed Management Conference, Henderson, NV, May 20-21, 2020.

Lai, Y.G., Abban, B., and Politano, M. (2022). A processed-based mesh-distributed watershed model for water runoff and soil erosion simulation. Int. J. River Basin Management (under print).

Low, H.S. (1989). Effect of sediment density on bed-load transport. Journal of Hydraulic Engineering, 115, 124–148.

Maidment, D.R. (1993). Handbook of Hydrology. New York: McGraw-Hill, Inc.

Nord, G., Esteves, M., Lapetite, J.M. and Hauet, A. (2009). Effect of particle density and inflow concentration of suspended sediment on bedload transport in rill flow. Earth Surface Processes and Landforms, 34, 253–263.

Obrist, D., Pearson, C.,Webster, J., Kane, T., Lin, C.-J., Aiken, G.R., and Alpers, C.N., 2016. A synthesis of terrestrial mercury in the western United States: Spatial distribution defined by land cover and plant productivity. Sci. Total Environ. 568, 522–535.

Ogden, F.L. and Saghafian, B. (1997). Green and Ampt Infiltration with Redistribution. ASCE J. Irrigation & Drainage Engineering, 123(5), 386-393.

Ogden, F.L. and Julien, P.Y. (2002). CASC2D: A Two-Dimensional, Physically-Based, Hortonian, Hydrologic Model. Mathematical Models of Small Watershed Hydrology and Applications, V.J. Singh, and D. Freverts (eds), Water Resources Publications, Littleton, Colorado.

Panday, S. and Huyakorn, P.S. (2004). A fully coupled physically-based spatially-distributed model for evaluating surface/subsurface flow. Advances Water Resources, 27(4), 361–82.

Politano, M. (2018). GHOST — Generic Hydrologic Overland-Subsurface Toolkit. Theory guide. IIHR Report No. 519.

Qu Y., and Duffy, C.J. (2007). A semidiscrete finite volume formulation for multiprocess watershed simulation, Water Resour. Res., 43, W08419., 10.1029/2006WR005752.

Rawls, W.J., Brakensiek, D.L. and Miller, N. (1983). Green-Ampt infiltration parameters from soils data. Journal of Hydraulic Engineering, 109(1), 62-69.

Rulli, M.C., Offeddu, L., and Santini, M. (2013). Modeling post-fire water erosion mitigation strategies, Hydrol. Earth Syst. Sci., 17, 2323–2337.

Sanchez, R.R. (2002). GIS-based Upland Erosion Modeling, Geovisualization and Grid Size Effects on Erosion Simulations with CASC2D-SED, Ph.D. Thesis, Civil Engineering, Colorado State University, Fort Collins, CO.

Schlüter, K., 2000. Review: evaporation of mercury from soils. An integration and synthesisof current knowledge. Environ. Geol. 39, 249–271.

Shields, F.D., Knight, S.S. and Cooper, C.M. (1995). Rehabilitation of watersheds with incising channels. Water Resources Bulletin, 31(6), 971-982.

Smith, D. B., Cannon, W. F., Woodruff, L. G., Solano, F., Kilburn, J. E., and Fey, D. L., 2013, Geochemical and mineralogical data for soils of the conterminous United States. U.S. Geological Survey Data Series 801, 19 p., https://pubs.usgs.gov/ds/801/

Stern, M., Flint, L., Minear, J., Flint, A., Wright, S. (2016). Characterizing changes in streamflow and sediment supply in the Sacramento River basin, California, using Hydrological Simulation Program - FORTRAN (HSPF). Water; 8(10):432.

Swets, D.L., Reed, B.C., Rowland, J.R., and Marko, S.E. (1999). A weighted least-squares approach to temporal smoothing of NDVI. In Proceedings of the 1999 ASPRS Annual Conference, from Image to Information, Portland, Oregon, May 17-21, Bethesda, Maryland, American Society for Photogrammetry and Remote Sensing, CD-ROM, 1 disc.

Therrien, R., Panday, S.M., McLaren R.G., Sudicky, E.A, Demarco, D.T., Matanga, G.B. and Huyakorn, P.S. (2003). HydroSphere: A Three-Dimensional Numerical Model Describing Fully-integrated Subsurface and Surface Flow and Solute Transport. User's Manual of HydroSphere, a Draft.

UNESCO (2013). Soil Erosion and Sediment Production on Watershed Landscapes: Processes and Control. Peter F. Ffolliott, Daniel G. Neary, Kenneth N. Brooks, Roberto Pizarro Tapia, Pablo García Chevesich.

USEPA (United States Environmental Protection Agency). (1997). Mercury Study Report to Congress, Volumes I through VIII. Office of Air Quality Planning and Standards and ORD. (EPA/452/R-97-001 thru 010; December 1997).

USFS Geospatial Technology and Applications Center, 2022. Burned Area Emergency Response Program FAQ. https://burnseverity.cr.usgs.gov/baer/faq. Accessed 7/11/2022.

USGS (United States Geological Survey). (2014). National Geospatial-Intelligence Agency (NGA), and National Aeronautics and Space Administration (NASA). Shuttle Radar Topography Mission 1 Arc-Second Global. Available online at https://earthexplorer.usgs.gov. Accessed 10/10/2017.

van Genuchten, M. T., 1980, A closed-form equation for predicting the hydraulic conductivity of unsaturated soils. Soil science society of America journal, 44, 892–898.

Vanderkwaak, J. (1999). "Numerical Simulation of Flow and Chemical Transport in Integrated Surface-Subsurface Hydrological Systems," Ph.D. Thesis, Earth Sciences, University of Waterloo, Waterloo, Ontario, Canada.

Velleux, M.L., England, J.F. and Julien, P.Y. (2005). TREX Watershed Modeling Framework User's Manual: Model Theory and Description. Colorado State University, Dept. Civil and Environmental Engineering, Fort Collins, CO.

Wang, J., Alpers, C.N., Lai, Y., Quinn, N.W.T., Weigand, J., and Sholtes, J., (2017), Integrated modeling of mercury transformation and transport in watersheds subject to wildfire, Technical Report SRH-2017-xx, Bureau of Reclamation.

Wang, J., Stern, M., Alpers, C.N., King, V.M., Webster, J., Quinn, N.W.T, and Lai, Y. (2019). Research and Development of a Watershed-Scale Model/Tool for Simulating Effects of Wildfires on Mercury Contamination of Land and Water, Report No. ST-2019-7112-01, Research and Development Office, Bureau of Reclamation, USA.

Wang, J., Stern, M.A., King, V.M., Alpers, C.N., Quinn, N.W.T., Flint, A.L., Flint, L.E. (2020). PFHydro: A New Watershed-Scale Model for Post-Fire Runoff Simulation. Environmental Modelling & Software Vol. 123 (2020), 104555. DOI: 10.1016/j.envsoft.2019.104555.

Wang, Q., Kim, D., Dionysiou, D.D., Sorial, G.A., and imberlake, D. (2004). Sources and remediation for mercury contamination in aquatic systems - a literature review, Environmental Pollution, vol. 131, pp.323-336.

Wicks, J.M., and Bathurst, J.C. (1996). SHESED: A physically based, distributed erosion and sediment yield component for the SHE hydrological modeling system, J. Hydrol, 175, 213-238.

Wigmosta, M.S., and Lettenmaier, D.P. (1999). A comparison of simplified methods for routing topographically-driven subsurface flow, Water Resour. Res. 35, 255-264.

Wischmeier, W.H. and Smith, D.D. (1978). Predicting Rainfall-Erosion Losses. Agricultural Handbook Number 537. Washington, DC: United States Department of Agriculture-Science and Education Administration.

Wool, T.A., Ambrose, R.B., Martin, J.L., Comer, E.A., and Tech, T. (2006). Water quality analysis simulation program (WASP). User's Manual, Version, 6.

Zhang, G.H., Wang, L.L., Tang, K.M., Luo, R.T. and Zhang, X.C. (2011). Effects of sediment size on transport capacity of overland flow on steep slopes. Hydrological Sciences Journal, 56(7), 1289-1299, doi: 10.1080/02626667.2011.609172.